

A Measurement of Helicity-Frame Spin Alignment of Inclusive $\Upsilon(nS)$ Mesons in $p\bar{p}$ Collisions at 1.96 TeV

by

James Thome

A dissertation submitted in partial fulfillment of the
requirements for the degree of

Doctor of Philosophy

in the Department of Physics

Carnegie Mellon University

August 29, 2011

Carnegie Mellon University
MELLON COLLEGE OF SCIENCE

THESIS


SUBMITTED IN PARTIAL FULFILLMENT OF THE REQUIREMENTS
FOR THE DEGREE OF

DOCTOR OF PHILOSOPHY IN THE FIELD OF PHYSICS


**TITLE: "A Measurement of Helicity-Frame Spin Alignment of Promptly Produced
Y(nS) Mesons in $p\bar{p}$ Collisions at 1.96 TeV"**

PRESENTED BY: James Thome

ACCEPTED BY THE DEPARTMENT OF PHYSICS

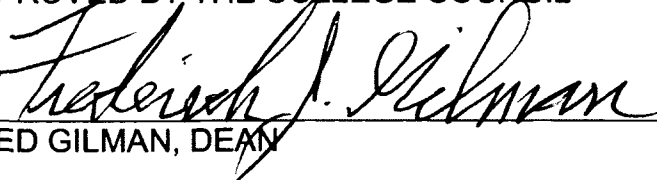


JAMES RUSS, MAJOR PROFESSOR 8/29/11
DATE



GREGG FRANKLIN, DEPT HEAD 8/29/11
DATE

APPROVED BY THE COLLEGE COUNCIL



FRED GILMAN, DEAN 8/31/11
DATE

Abstract

Measurements of $\Upsilon(nS)$ spin alignment have been made, using 4.9 fb^{-1} of data obtained by the CDF II detector at the Tevatron. The analysis is performed in the s-channel helicity frame on Υ mesons having rapidity $|y| < 0.6$ and $2 < p_T \leq 40 \text{ GeV}/c$ via the decay channel $\Upsilon(nS) \rightarrow \mu^+ \mu^-$. A template method is used to correct for acceptance and trigger effects. The $\Upsilon(1S)$ polarization is small and longitudinal at low p_T . It is consistent with a constant at all p_T . The $\Upsilon(2S)$ and $\Upsilon(3S)$ behaviors are similar to each other within statistics. Both have small polarization at low p_T and move toward transverse polarization in the bin with $p_T > m(\Upsilon)$.

Acknowledgments

I would like to thank the many individuals without whom the work presented in this thesis could not have been completed, and those whose presence over the years helped me better enjoy the time spent on it.

First and foremost, I thank my adviser, Jim Russ, whose expertise and knowledge were the guiding force behind this analysis, and whose patience has been unfathomable.

The members of the CDF B Physics group are also of note for their thoughtful attention and suggestions in countless meetings. I am very grateful to have had the assistance of Jonathan Lewis, who frequently took time to sit down with me and discuss the analysis and share his expertise. Vaia Papadimitriou, Matthew Jones, Diego Tonelli, Michal Kreps, and Rob Harr all contributed often to discussions about this work, strengthening the results greatly.

Zhen Tang has made several key contributions to this analysis, and is continuing the investigation beyond the scope of this thesis.

I also offer my thanks to the CDF Operations group, especially Mark Mattson and the ADMEM support crew, with whom I spent many hours in the collision hall jiggling wires.

I thank my thesis committee for their time and insight which have improved this document: Manfred Paulini, Helmut Vogel, Ira Rothstein, and Adam Leibovich.

I have been blessed with great co-workers and friends over the past several years. Many thanks to my erstwhile officemate, Elisa Pueschel, for putting up with me

in multiple states, and for commiserating when things got rough. Dean Hidas, Bo Jayatilaka, and John Freeman helped me stay sane during countless hours at the gym, over meals, or over drinks. Soon Yung Jun not only selflessly helped me with bug fixes and software problems, but also offered worldly wisdom, always with a smile.

The graduate students and faculty at CMU have all contributed to a great environment and a fun place to work. I was lucky to have Ben Beppler, Chris Hefferan, and Brian Vernarsky around to shoot pool and go to Penguins games with.

The CMU Physics Department Staff deserves note for saving me from my many oversights and mistakes, and for being generally great people. Thanks to all the staff, especially Hilary Homer, Mary Jane Hutchison, and Patrick Carr.

I would never have started down the path of High Energy Physics without the encouragement and enthusiasm of Sally Koutsoliotas, who brought me to work at Fermilab in the summer of 2003. There, I worked with Morgan Wascko, whose good nature and passion for science reinforced my burgeoning interest in the field.

Lastly, without the love and support of my parents, I never could have completed this work.

Preface

As evinced by the title and abstract of this thesis, the primary topic presented herein is a measurement of the spin alignment of Υ (“Upsilon”) mesons. Such a discussion obviously starts at a description of what the Υ is, and why it has a spin alignment. Carrying this line of thought further brings us to a discussion of theoretical predictions and the results of other similar measurements. All these things are discussed in Chapter [1](#)

The means of producing Υ mesons, and most other interesting particles, are non-trivial. The work presented herein is based on data collected at the Tevatron accelerator at Fermilab by the CDF detector, both of which are described at length in Chapter [2](#)

The methods utilized to discern the spin alignment of the Υ are described in Chapters [3](#)[4](#). The results and discussions of systematic effects and possible future work are presented in Chapters [5](#) and [6](#)

Contents

Preface	1
1 Introduction	5
1.1 The Standard Model	5
1.2 Quantum Chromodynamics	6
1.3 Positronium and the Quarkonium Spectrum	8
1.3.1 Υ Spin Alignment and Decay Angular Distributions	13
2 Experimental Apparatus	17
2.1 Protons and Antiprotons	17
2.1.1 Proton source	17
2.1.2 Anti-Proton source	19
2.1.3 Tevatron	20
2.2 CDF Detector	21
2.2.1 Tracking Systems	22
2.2.2 Calorimetry	25
2.2.3 Muon Systems	28
2.3 Trigger System	32
2.3.1 Level 1 Trigger	33
2.3.2 Level 2 Trigger	34
2.3.3 XFT and XTRP Tracking Algorithms	34

CONTENTS	3
----------	---

2.3.4 Level 3 Trigger	35
-----------------------	----

2.3.5 Upsilon Trigger Path	35
----------------------------	----

3 Simulation	37
---------------------	-----------

3.0.6 Monte Carlo Generation	37
------------------------------	----

3.0.7 Acceptance and Efficiency	38
---------------------------------	----

3.0.8 Monte Carlo re-weighting	41
--------------------------------	----

3.0.9 Angular Binning and p_T Resolution	46
--	----

3.0.10 Test of Monte Carlo using μ^+ distributions in p_T and η	53
--	----

4 Data Treatment and Spin Alignment Analysis	58
---	-----------

4.1 Data Processing	58
---------------------	----

4.2 Backgrounds	59
-----------------	----

4.3 $\Upsilon(nS)$ Polarization Analysis	59
--	----

4.3.1 Υ Mass PDFs from Simulation	62
--	----

4.3.2 Υ Mass Fits	64
----------------------------	----

4.3.3 Υ Polarization Fitter	67
--------------------------------------	----

4.3.4 Toy Monte Carlo Tests of Fitter	69
---------------------------------------	----

5 Results	72
------------------	-----------

5.1 $\Upsilon(nS)$ Polarization Results	72
---	----

5.2 Systematics	72
-----------------	----

5.3 Comparison with Other Measurements	82
--	----

6 Conclusions	88
----------------------	-----------

6.1 Summary	88
-------------	----

6.2 Current and Future Efforts	89
--------------------------------	----

A Angular Distribution Derivation	95
--	-----------

Appendices	95
-------------------	-----------

B Mass Fit Plots	98
B.1 Mass Fits in p_T Bins	98
B.2 Mass Fits in Angular Bins	102
C Alternate fitter	110

Chapter 1

Introduction

1.1 The Standard Model

The Standard Model is a theory which describes the set of fundamental particles and the forces and interactions among them. Specifically, the model is a combination of the theory of quantum chromodynamics (QCD) and quantum electroweak theory. In the Standard Model, the set of fundamental particles consists of twelve spin- $\frac{1}{2}$ fermions, each with its own anti-particle. Six of these fermions are leptons: the electron (e), the electron neutrino (ν_e), the muon (μ), the muon neutrino (ν_μ), the tau (τ), and the tau neutrino (ν_τ). The remaining six fermions are quarks: up (u), down (d), charm (c), strange (s), top (t), and bottom (b). The fundamental fermions are arranged into generations, in increasing mass:

$$\begin{pmatrix} u \\ d \end{pmatrix} \begin{pmatrix} c \\ s \end{pmatrix} \begin{pmatrix} t \\ b \end{pmatrix} \\ \begin{pmatrix} e \\ \nu_e \end{pmatrix} \begin{pmatrix} \mu \\ \nu_\mu \end{pmatrix} \begin{pmatrix} \tau \\ \nu_\tau \end{pmatrix}.$$

As the first generation consists of the lightest, most stable particles, most matter in the universe is comprised of these particles. The heavier particles are short-lived

Quarks			Leptons		
Quark	Charge (e)	Approx. Mass (GeV/c^2)	Lepton	Charge (e)	Mass (GeV/c^2)
u	$\frac{2}{3}$	0.003	e	-1	0.000511
d	$-\frac{1}{3}$	0.005	ν_e	0	~ 0
c	$\frac{2}{3}$	1.27	μ	-1	0.106
s	$-\frac{1}{3}$	0.101	ν_μ	0	~ 0
t	$\frac{2}{3}$	172.0	τ	-1	1.78
b	$-\frac{1}{3}$	4.19	ν_τ	0	~ 0

Table 1.1: Some properties of quarks and leptons.

and will decay to more stable states. Some properties of the quarks and leptons are shown in Table [1.1](#)

The Standard Model also features spin-1 bosons which mediate the fundamental forces through which particles can interact. The photon (γ) carries the electromagnetic force, which acts on charged particles. The massive Z and W^\pm mediate the weak interaction, effecting all quarks and leptons. Finally, gluons (g) mediate the strong interaction among particles with “color charge” (common to all quarks and gluons). These strong interactions are described by quantum chromodynamics, which is described in Section [1.2](#)

1.2 Quantum Chromodynamics

Quantum chromodynamics is a non-abelian gauge theory of the $SU(3)$ group that describes strong interactions among colored quarks and gluons. Each type of quark possesses a color charge, which can be one of six “colors” (three colors each with an anti-color). Gluons are the generators of the color $SU(3)$ group, and come in color-anticolor combinations, for a total of 8 possible color varieties. The color degree of freedom was developed in response to an apparent violation of Fermi-Dirac statistics

in spin- $\frac{3}{2}$ baryons. Such particles, interpreted as three-quark states, would require that all constituent quarks be in the same spin state, meaning that all three fermions were in the same quantum state. In order to break the symmetry of the wave function, the color degree of freedom was hypothesized. Each quark of the baryon should have a distinct color charge (red, green, blue, or their anti-colors).

While the color degree of freedom solves the baryon wave function asymmetry problem, it could potentially lead to a vast number of additional states. This issue gives rise to another tenet of the color hypothesis: hadrons (mesons and baryons) can only exist in “colorless” states. As such, mesons, consisting of a quark and an antiquark, must be color-anticolor pairs, and baryons contain one quark of each color. Furthermore, a quark, which has color charge, cannot be isolated from a hadron. This is a statement of a feature unique to the strong force, known as color confinement. Unlike any of the other forces, the magnitude of the strong force grows with the distance between two particles bound by the strong force. If an attempt were made to separate a quark from a hadron, it would eventually become energetically favorable for a quark-antiquark pair to appear out of the vacuum, forming new hadrons. In a real setting, such as the Tevatron accelerator described in Chapter 2 this phenomenon (known as “hadronization”) is observed in the form of jets of hadrons clustered together. As one would expect, single quarks have never been observed.

Another interesting feature of QCD is that, at very short length scales (high momentum transfer), the QCD coupling α_s becomes arbitrarily small. This phenomenon is known as “asymptotic freedom,” quarks can behave as if free on these scales. Gluons, carrying a color charge themselves, are self-coupling. Asymptotic freedom can be viewed as a result of a screening process undergone by particles with color charge. Virtual gluons shield the color charge, but due to the dual color of the gluon, this serves to ‘spread out’ the color charge of the fermion, which results in a weaker coupling at large momentum transfer. Luckily, this weakened coupling facilitates perturbative calculations in α_s .

1.3 Positronium and the Quarkonium Spectrum

The heavy quark-antiquark bound states $c\bar{c}$ and $b\bar{b}$ are known as 'quarkonium.' While the quarks are interacting via a strong potential, an analogy can be made with particle-antiparticle states bound by the electromagnetic force, namely, e^+e^- , or positronium.

The static Coulomb potential goes as $V_C \propto 1/r$, which, for the hydrogen atom, leads to bound-state energy levels of the form,

$$E_n = -\frac{\alpha^2 mc^2}{2n^2}. \quad (1.1)$$

Here, n is the principal quantum number, α is the electromagnetic coupling constant, and m is the reduced mass of the system. The energy levels are degenerate, as n is taken to be $N + l + 1$, where N is the number of nodes in the radial wave function and l in the orbital angular momentum. This degeneracy is broken by the spin-orbit interaction and the spin-spin interaction, though the splittings are very small.

Positronium can be described in much the same way, except that the reduced mass is a factor of two smaller, which leads to a more weakly-bound system. Furthermore, the spin-spin coupling has a much stronger effect in this case because the electron magnetic moment is far greater (by a factor of about 650) than that of the proton. To accurately describe positronium energy levels, one must consider the total spin S and total angular momentum J in addition to the principal quantum number and orbital angular momentum L . Clearly, S can take on values of 0 and 1, respectively known as singlet and triplet states.

Comparing the spectra of quarkonium to positronium, the lowest energy levels are similarly-arranged, up to a scale factor of about 10^8 . Higher energy levels deviate from the pattern of positronium. This seems to indicate that at small r , the quarkonium potential is of a similar form to that of positronium. It is also known that quarks cannot be separated, so the potential must grow linearly at larger distances. Thus,

the potential can be described by the ansatz [1],

$$V = -\frac{4}{3} \frac{\alpha_s(r) \hbar c}{r} + kr. \quad (1.2)$$

The factor of $4/3$ is due to the three colors of quarks, α_s is the strong coupling constant (which varies with r), and k is a constant.

This potential does not fully describe the energy levels seen in quarkonium states, because it does not account for the spin-spin interactions. This portion of the potential is again analogous to the positronium case, as seen in Equation [1.3]

$$V_{ss}(q\bar{q}) = \frac{8\pi\hbar^3}{9c} \alpha_s \frac{\sigma_q \cdot \sigma_{\bar{q}}}{m_q m_{\bar{q}}} \delta(x), \quad (1.3)$$

where the σ vectors are made up of Pauli spin matrices. This interaction corresponds to the flipping of a quark spin state.

The Υ (“Upsilon”) is a vector meson comprising a $b\bar{b}$ bound state (this is known as “bottomonium”). It exists in a spin triplet state (3S_1). The lowest-mass 3S_1 state of bottomonium, the $\Upsilon(1S)$, and the first two radial excited states, $\Upsilon(2S)$ and $\Upsilon(3S)$, lie below the mass threshold for decay into B mesons and have significant probability to undergo leptonic decays. Because of the high quark masses involved in quarkonia, the quark constituents have relative velocities which are non-relativistic. This allows for approximate calculations of meson properties based on expansions in α_s and v/c . The spectrum of the bottomonium family is shown in Figure [1.1]

The first and most natural application of QCD to quarkonium production was the Color Singlet Model (CSM) [3]. In that model, quarkonium production is considered as the creation of a heavy quark pair, which is treated perturbatively, and their binding into quarkonium, which is factorized in a universal wave function. The model assumes that the quark color and spin remain constant as the quarks bind together. The leading-order diagrams for production of 3S_1 states associated with a gluon are shown in Figure [1.2]

The CSM was applied to describe quarkonium states such as the Υ states and the

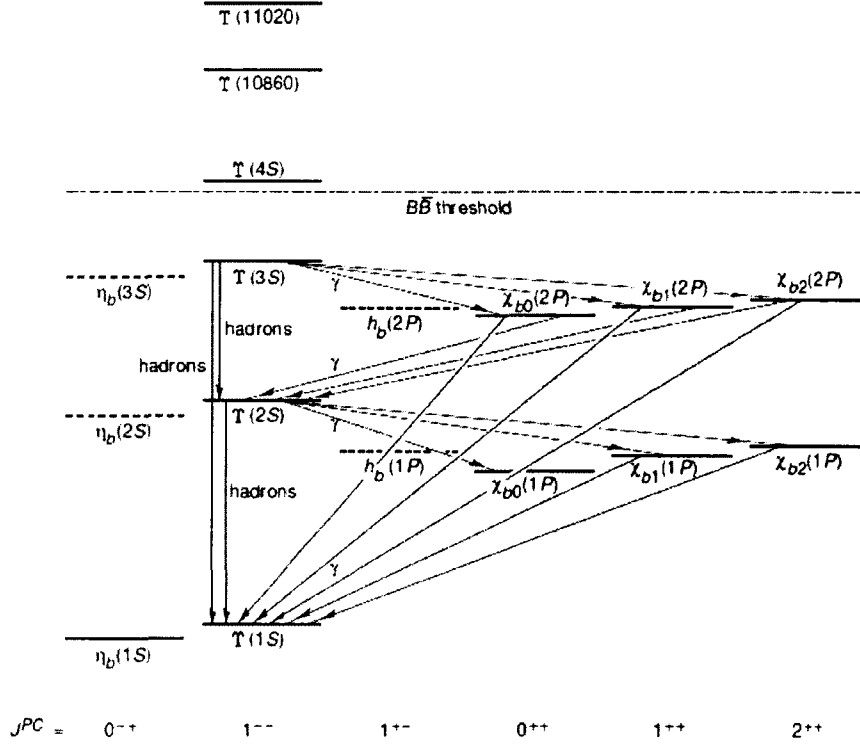


Figure 1.1: The spectrum of the bottomonium family. [2]

J/ψ and $\psi(2S)$. However, early CDF results on the J/ψ and $\psi(2S)$ cross-sections [4] indicated that the CSM predictions for the prompt cross-section were an order of magnitude too low.

Since the Tevatron Run I observations of surprisingly large production cross sections for all three vector mesons J/ψ , $\psi(2S)$, and Υ , vector meson production and polarization in hadronic collisions has usually been discussed within the framework of non-relativistic QCD (NRQCD). This theoretical framework separates the heavy flavor production into a perturbative short-distance process to produce the $Q\bar{Q}$ pair times a long-distance matrix element to create the vector meson (or, more generally, any quarkonium state). The short-distance process can include color-octet $Q\bar{Q}$ contributions as well as color singlet configurations because the long-distance matrix elements can absorb soft gluon emission terms. This *factorization* hypothesis lies at

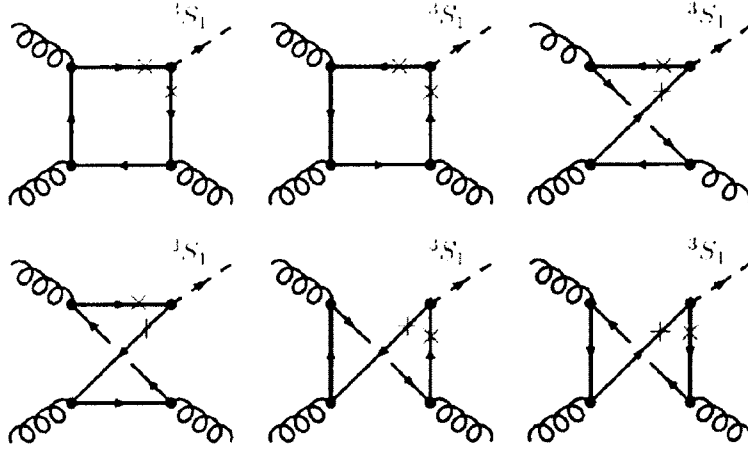


Figure 1.2: The six leading-order diagrams for 3S_1 states in the CSM.

the core of the NRQCD analysis [5]. The long-distance part is expanded in powers of the heavy quark velocities, using the vacuum expectation values of appropriate 4-fermion operators with parametrized coefficients. These coefficients are *universal* in that they are the same for all quarkonium states. Fixing them from data in one process leads to predictions valid in all other quarkonium production processes.

Using the degrees of freedom available in the parametrization, NRQCD calculations can fit the Tevatron production cross sections for the three vector mesons [6, 7]. However, the theory predicts that vector meson polarization should become transverse in the perturbative regime, i.e., for large transverse momentum p_T of the vector meson. Recent CDF measurements of polarization for J/ψ and $\psi(2S)$ do not support this prediction [8, 9], as shown in Figures 1.3 and 1.4. Measurements of J/ψ photoproduction at HERA can be described by NLO CSM calculations without color octet contributions as included in NRQCD [10, 11]. Some theorists have proposed a different NRQCD expansion for c-quark states and b-quark states [12]. The NRQCD predictions for Υ polarization for Tevatron Run I, including feed-down effects from higher charmonium states, from Braaten and Lee [13] are shown in Figure 1.5.

Recently, different models of production that emphasize higher-order processes

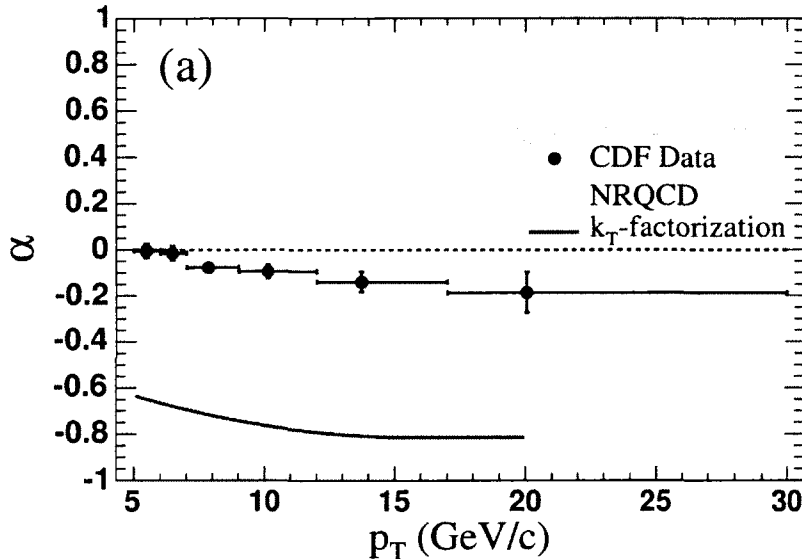


Figure 1.3: The CDF Run II measurement of J/ψ polarization shows slight longitudinal polarization over the entire p_T region, in contrast with NRQCD predictions.

have been invoked to explain the vector meson production data. A model invoking a tower of gluon processes, leading to a sum of NLO amplitudes that enhances the LO color singlet amplitude, has been proposed [14]. This model gives a qualitative description of the CDF Run II measurements for J/ψ and $\psi(2S)$ production and polarization. A new color singlet calculation including terms up to α_s^5 has been used to model $\Upsilon(1S)$ production and polarization [15]. One of the features of this model is that the Υp_T will be balanced by one or more gluon jets.

All authors agree that polarization and production information on the Υ family are essential tests of NRQCD and alternative production models. This note describes the first step in that procedure for CDF data - a measurement of the $\Upsilon(nS)$ production polarization.

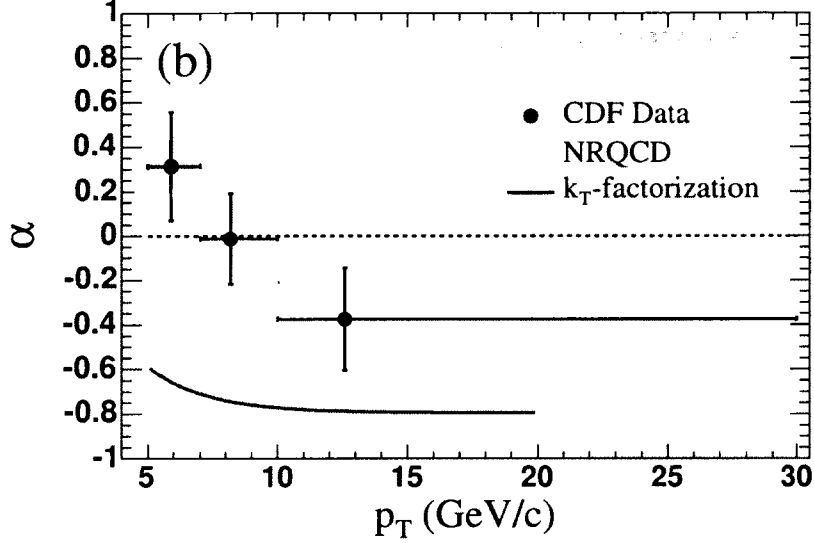


Figure 1.4: The CDF Run II measurement of $\psi(2S)$ polarization shows longitudinal polarization at high p_T , in contrast with NRQCD predictions.

1.3.1 Υ Spin Alignment and Decay Angular Distributions

This analysis, like all proton collider polarization analyses to date, uses a quantization axis defined in the s-channel helicity frame. In this frame, the quantization axis is defined as the negative of the boost direction that takes the Υ from the laboratory frame to its rest frame, *i.e.*, the negative of the Υ direction in the lab.

The polarization can be determined using the dilepton decays of the Υ , and this analysis utilizes the dimuon decay, $\Upsilon \rightarrow \mu^+ \mu^-$. Dielectrons could provide the same information, but limitations in the mass resolution for these events greatly reduce the ability to perform this kind of analysis at CDF.

In the rest frame of the Υ meson, the μ^+ makes an angle θ^* with respect to the Υ direction in the lab frame. The angular distribution depends on the polarization parameter α , which lies in the interval -1 to 1 :

$$\frac{d\Gamma}{d\cos\theta^*} \propto 1 + \alpha \cos^2\theta^*. \quad (1.4)$$

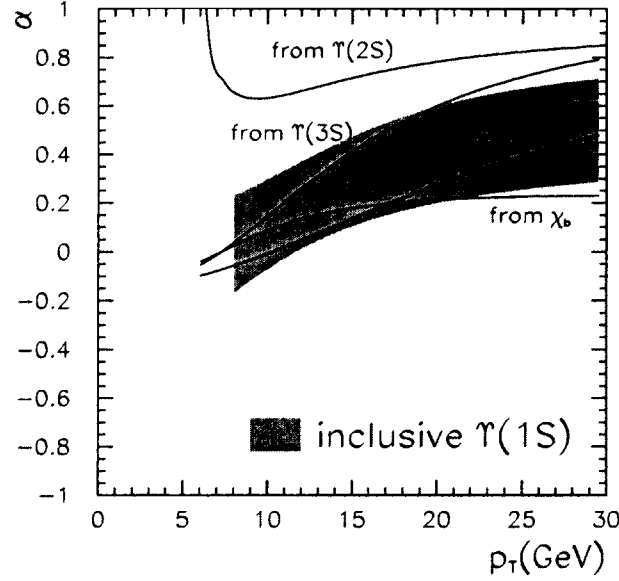


Figure 1.5: NRQCD prediction for $\Upsilon(1S)$ prompt polarization, including feed-down from higher bottomonium states.

The derivation of the form of this angular distribution is given in Appendix [A](#)

If the Υ meson is fully polarized in the transverse direction, $\alpha = 1$. If it is fully aligned longitudinally, $\alpha = -1$. In our later discussion we use a related alignment parameter η that measures the fraction of longitudinal alignment. The two parameters are simply related:

$$\eta = \frac{1 - \alpha}{3 + \alpha} \quad (0 \leq \eta \leq 1). \quad (1.5)$$

There have been a number of studies of the properties of Υ mesons performed previously. Most applicable to this analysis are the Tevatron measurements. CDF measured Υ polarization and cross-section in Run I [\[16\]](#), finding that the $\Upsilon(1S)$ polarization was consistent with zero, *i.e.*, unpolarized. More recently at the Tevatron, the DZero Collaboration published polarization results for the $\Upsilon(1S)$ and $\Upsilon(2S)$ states [\[17\]](#). Their findings indicated longitudinal polarization at low- p_T , shifting to transverse above about 10 GeV/c. The $\Upsilon(2S)$ polarization was found to be transverse, but

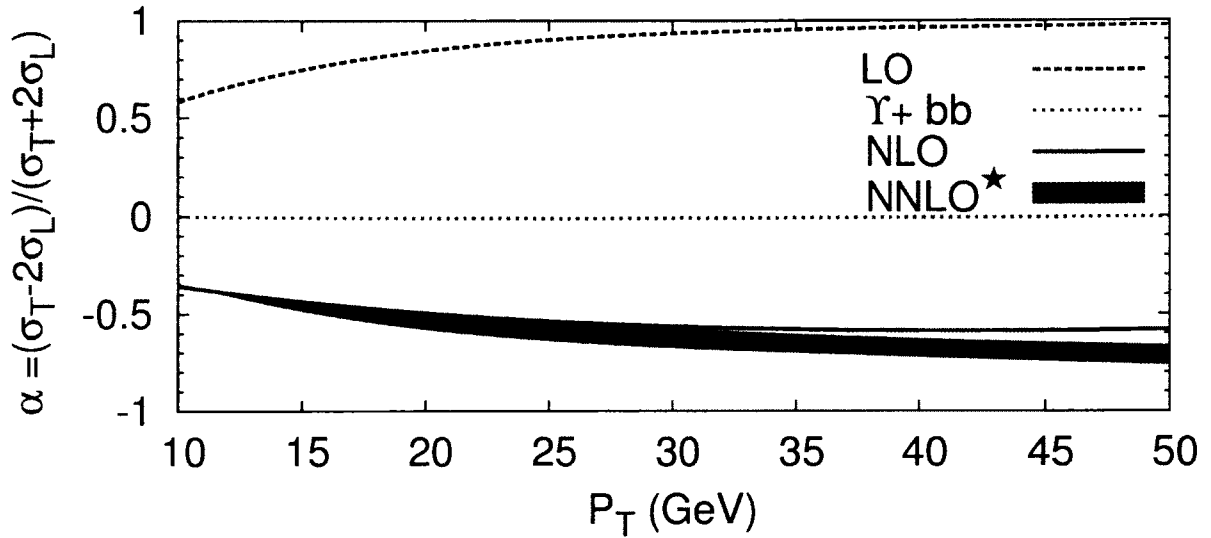


Figure 1.6: Color Singlet Model prediction for $\Upsilon(1S)$ prompt polarization, including NNLO terms from multigluon processes.

with large error bars.

Fixed target measurements, *e.g.*, E866 at Fermilab, have also measured Υ polarization, albeit in a different (Collins-Soper) frame. In this frame, the quantization axis is chosen along the proton direction of the beamline. That measurement found slight transverse polarization of the $\Upsilon(1S)$, and the $\Upsilon(2S+3S)$, measured together for lack of adequate resolution, are fully transversely polarized.

This measurement, based on 4.9 fb^{-1} of data from CDF Run II, seeks to clarify the theoretical picture and confirm or refute the previous experimental results. The method of the analysis differs from CDF Run I and is explained in Chapters [3](#) and [4](#)

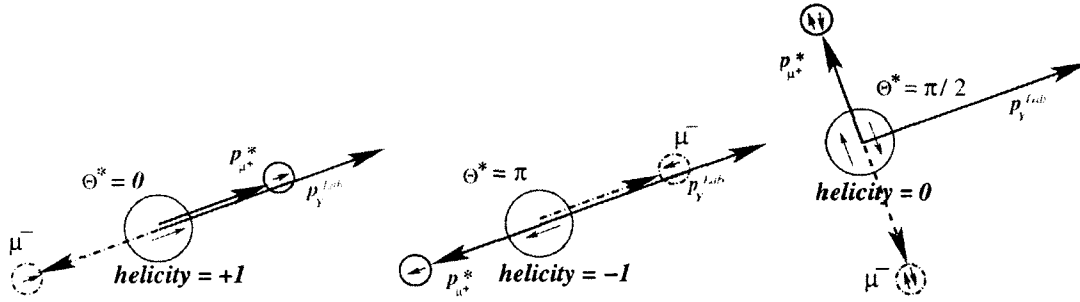


Figure 1.7: The diagrams of polarization angles with three different helicity states. When the helicity states are equally populated, Υ mesons have zero polarization. The little arrow on the top of each particle indicates its spin alignment.

Chapter 2

Experimental Apparatus

Particle physics experimenters seek to observe the world at its most fundamental level. This effort requires advanced and specialized equipment and a great deal of collaboration. To probe the nature of particles and interactions, high-energy particle colliders are necessary to produce such particles and interactions that may then be observed. To do this observation requires a sophisticated multi-purpose detector designed to measure and reconstruct the vast breadth of interactions of interest. At Fermilab, these tasks are accomplished by the Tevatron accelerator and two detectors, D0 and CDF, the latter of which provides the data for this analysis. This chapter provides a look at the accelerator and the CDF detector.

2.1 Protons and Antiprotons

2.1.1 Proton source

The Tevatron accelerator was, until recently, the highest-energy particle accelerator in the world. Having been eclipsed in energy by the Large Hadron Collider (LHC) at CERN, it remains the highest-energy *proton-anti-proton* accelerator in the world, and so it will be up until its imminent shutdown. As such, any adequate discussion of the Tevatron begins with the production of protons and anti-protons.

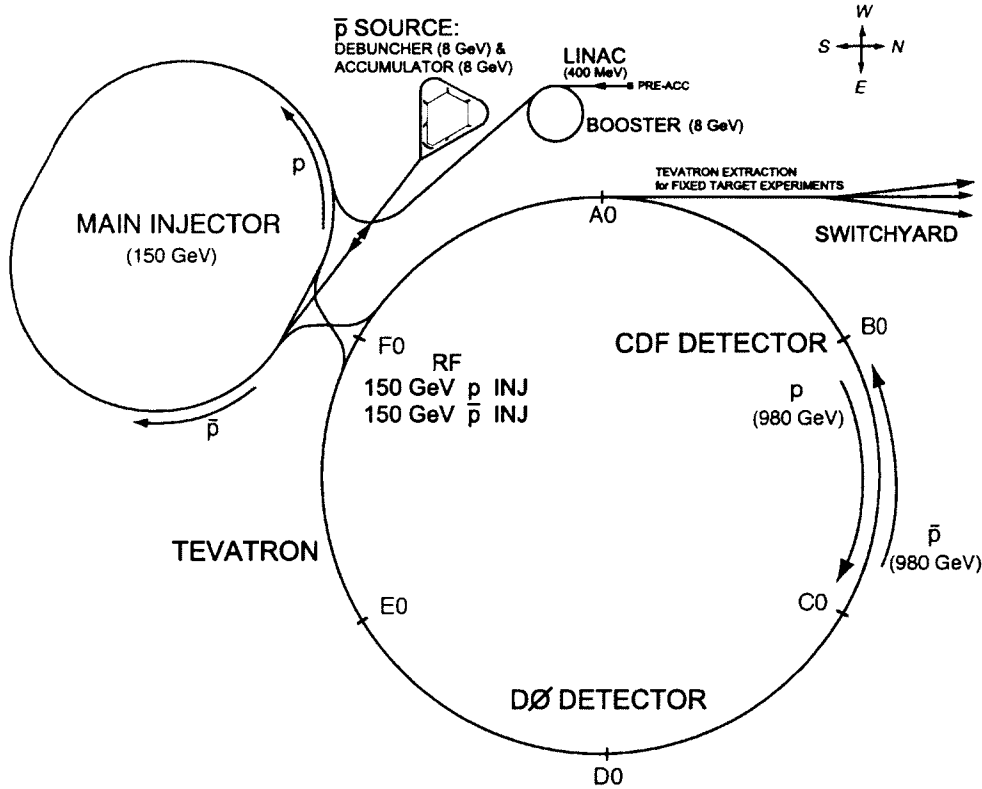


Figure 2.1: A schematic view of Fermilab's accelerator complex, showing each accelerator component beginning with the pre-accelerator and ending in the Tevatron.

Hydrogen gas is ionized by electrical discharges in the pre-accelerator, forming H^+ (protons) and electrons. The protons drift toward a Cesium surface where they can acquire free electrons, forming H^- ions. The H^- ions are subsequently freed from this surface by errant protons in the ionized plasma.

A Cockroft-Walton generator supplies voltage to an electrostatic accelerating column that accelerates the H^- ions to an energy of 750 keV, whereupon they enter the Linac. The Linac consists of drift tubes and side-coupled cavities, which take the 750 keV H^- beam and accelerate it to 400 MeV. This process naturally groups H^- ions into bunches because of the alternating currents involved.

Once the H^- ions reach the end of the Linac, they are transferred to the Fermilab

Booster, a 474-meter-circumference synchrotron accelerator. Upon entry into the Booster, the H^- ions are finally stripped of their electrons when they pass through a thin carbon foil. The Booster uses 18 RF cavities to accelerate protons from their initial energy of 400 MeV to 8 GeV in less than 67 msec.

The next step in the accelerator chain is the Main Injector. Another synchrotron accelerator, the Main Injector takes 8 GeV protons from the Booster and accelerates them to 150 GeV for transfer to the Tevatron, or 120 GeV for anti-proton (\bar{p}) production.

2.1.2 Anti-Proton source

To produce the anti-protons that will collide with our protons, some of the protons from the Main Injector are extracted and used in the anti-proton source. These protons, with an energy of 120 GeV, are steered toward a nickel alloy target, where they interact to produce showers of particles. Approximately 10^5 protons are required to produce a single \bar{p} in this way, and \bar{p} 's are produced at a rate of 10^{11} per hour. The outgoing shower of particles from the target is focused into a beam by a cylindrical lithium lens, and the anti-protons are separated from other particles using a pulsed dipole magnet spectrometer. This process utilizes the fact that particles of different mass and charge curve differently in a magnetic field to extract only the anti-protons. The anti-proton beam exits the spectrometer with an average \bar{p} momentum around 8 GeV.

The anti-protons produced in the anti-proton source have a spread of momentum, making it necessary to homogenize the beam energy. Because the Main Injector uses RF to accelerate the beam, the protons arriving at the anti-proton source are bunched. These bunches, with their wide spread in energy, are sent to the debuncher, a triangular synchrotron. Therein, lower-energy \bar{p} 's and higher-energy \bar{p} 's take a slightly different path around the corners, causing their total path length around the debuncher to differ. This leads to a difference in the phases of the RF

seen by higher- and lower- energy particles. As a result, lower-energy particles are accelerated and higher-energy particles decelerated until an equilibrium is reached, thereby equilibrating the momentum profile and smoothing the bunches of the beam.

Protons are sent to the anti-proton source once every 1.5 seconds. During the interim, \bar{p} 's in the debuncher are subject to stochastic cooling. This is, in effect, a feedback system wherein a 'hot' beam with random variations in particle momentum and angle is 'cooled' using a pickup to detect the variations of individual particles and a kicker magnet to correct them. This process reduces the transverse size of the beam.

The antiprotons are then transferred to the Accumulator ring, which shares a tunnel with the Debuncher. Here, \bar{p} 's are stored at 8 GeV and subject again to stochastic cooling. When enough \bar{p} 's are gathered, they are transferred to the Recycler. The Recycler, which shares a tunnel with the Main Injector, not only stores 4 times more \bar{p} 's than the Accumulator, but is also capable of cooling the beam further. In addition to a stochastic cooling system, electron cooling is also utilized. The \bar{p} beam is combined with an electron beam whose emittance is much lower, and allowed to cool via heat exchange with the electrons. Because the Recycler operates at a fixed momentum, and because it would be costly to lose \bar{p} 's at this stage to a magnet quench, permanent magnets are used in lieu of superconducting magnets. At this point, the 8 GeV anti-proton beam is ready to be transferred to the Tevatron.

2.1.3 Tevatron

The final step in the accelerator chain is the Tevatron, wherein protons and anti-protons will collide to produce the events that will comprise our dataset. A synchrotron with a circumference of 6.3 km, the Tevatron accelerates p 's and \bar{p} 's from 150 GeV to 980 GeV (giving a final $p\bar{p}$ center of mass energy of 1.96 TeV). The protons and anti-protons are loaded separately into the Tevatron. First, the protons, at 150 GeV, are loaded in 36 bunches into the Tevatron. Anti-protons are accelerated

to 150 GeV in the Main Injector before being likewise transferred to the Tevatron in another 36 bunches, which cross with the protons once every 396 ns. These particles circulating in the Tevatron are referred to as a '*store*.'

The Tevatron is divided into sectors labeled A through F, and further divided into six numbered segments each. The collision points for the beam are located at B0 and D0, where reside the CDF and D0 detectors. At each detector, the beam is focused using quadrupole magnets to increase the *instantaneous luminosity*, \mathcal{L} , given by

$$\mathcal{L} = \frac{f N_B N_p N_{\bar{p}}}{4\pi\sigma_x\sigma_y}, \quad (2.1)$$

where N_B , N_p , and $N_{\bar{p}}$ are the number of bunches, protons, and anti-protons, respectively, f is the bunch-crossing frequency, and $4\pi\sigma_x\sigma_y$ is the effective cross-sectional area of the beam, presumed to feature a Gaussian profile. The integrated luminosity, $\int \mathcal{L} dt$, multiplied by the cross-section for a given interaction, provides a measure of the number of such interactions present in a dataset.

2.2 CDF Detector

The CDF II detector [18] is designed to collect information about the wide range of events that occur at the Tevatron. It features forward-backward symmetry along the beamline as well as a roughly cylindrical shape around the beam. A right-handed coordinate system is used, with z defined along the proton direction, and x and y pointing out of the ring and upward, respectively. Alternatively, the symmetry in the x - y plane allows for the use of a polar coordinate system, with the radial coordinate $r \equiv \sqrt{x^2 + y^2}$ and an azimuthal angle ϕ defined upward from the x -axis, *i.e.*, $\phi \equiv \tan^{-1}(y/x)$. The polar angle $\theta \equiv \cos^{-1}(z/\sqrt{x^2 + y^2 + z^2})$ is not invariant under boosts in the longitudinal direction (along the beamline), so it is often eschewed in favor of the *rapidity*, defined as

$$y \equiv \frac{1}{2} \ln \frac{E + p_z}{E - p_z}. \quad (2.2)$$

Outgoing particles from interactions have an approximately even distribution in rapidity. In the low-mass limit ($p \gg E$), this can be replaced by the *pseudo-rapidity*, η , defined as

$$\eta \equiv -\ln \tan \frac{\theta}{2}. \quad (2.3)$$

As the CDF detector is tasked with gathering data about all types of interactions, it comprises a number of sub-detectors designed for varying purposes. Beginning at the interaction point and moving radially outward, a particle will traverse tracking systems to determine charged particle momenta, calorimeters to measure particle energy, and muon systems to identify muons. These subdetectors are described below, focusing on the components used in this analysis.

2.2.1 Tracking Systems

The innermost components of CDF trace the paths of charged particles in a 1.4T magnetic field supplied by a superconducting solenoid. The solenoid is 5m in length, with an inner bore of 2.86m and outer diameter of 3.35m. It carries a current of 4650 A to produce a uniform magnetic field along the proton direction.

The tracking system consists of silicon microstrip detectors and a large drift chamber known as the Central Outer Tracker.

Silicon tracking

The silicon tracking system [19][20] consists of three radiation-hard silicon subdetectors surrounding the beamline. Moving outward from the beamline, they are Layer 00 (L00), the Silicon Vertex tracker (SVXII), and the Intermediate Silicon Layer (ISL).

CDF Tracking Volume

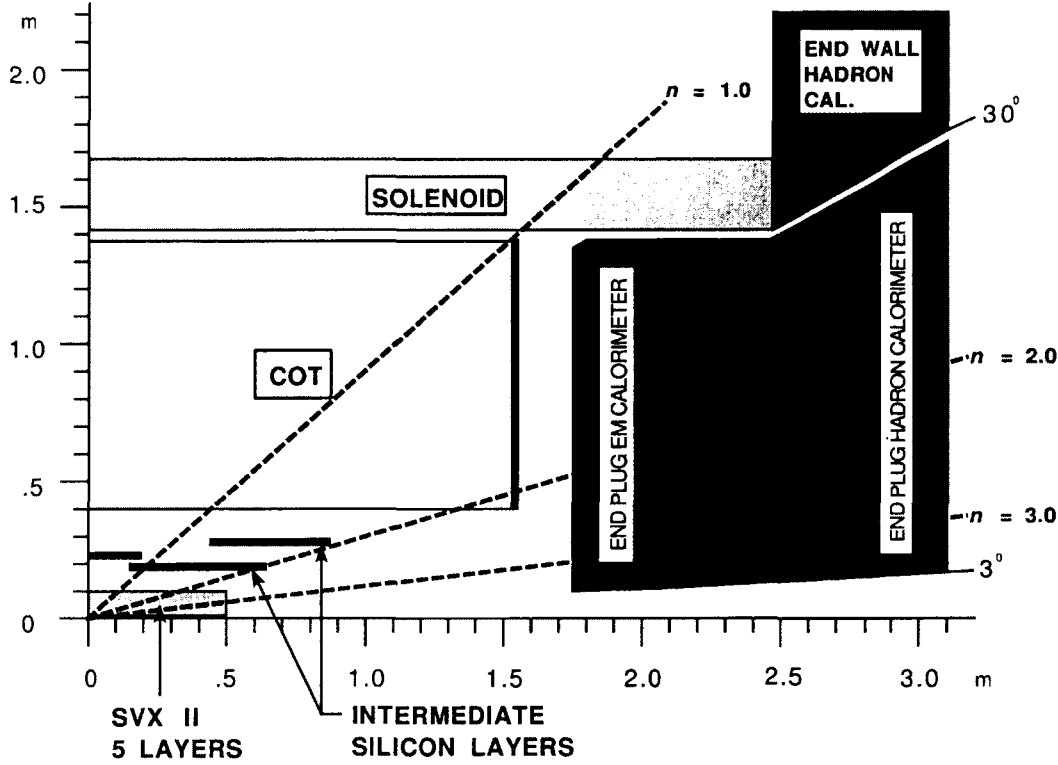


Figure 2.2: A diagram showing the location of the different elements of the CDF tracking system.

The L00 subdetector is mounted directly on the beampipe, at a radius of $r = 1.5\text{cm}$. It consists of 48 single-sided silicon strips with axial (aligned with the beam direction to measure r and ϕ) silicon microstrips. Its proximity to the interaction point and the relatively small amount of intervening material provide a much better measurement of the transverse impact parameter (d_0) than would be otherwise available.

Beyond L00, the SVXII occupies a region from $r = 2.5\text{cm}$ to 10.6cm . It consists of five layers of double-sided silicon sensors arranged into three cylindrical barrels along the beamline. One side of each sensor is axial, while the other is offset by either 1.2° (small angle stereo, or SAS, to measure r , ϕ , and z) or 90° (to measure z). The sensors comprising the SVXII are arranged in 30° azimuthal wedges, and each of the

five layers in each wedge is an independent module called a *ladder*.

Finally, the ISL encompasses the SVXII and bridges the gap between the SVXII and the Central Outer Tracker (COT). In the central region ($|\eta| < 1.0$), a single layer of double-sided sensors is situated at $r = 22\text{cm}$. Two layers of sensors at $r = 20\text{cm}$ and $r = 28\text{cm}$ extend coverage in the region $1.0 \leq |\eta| \leq 2.0$. Like the double-layered sensors in the SVXII, the ISL sensors feature axial and stereo silicon strips.

Because of the large mass of the Υ , the decay muons have a wide opening angle. Requiring silicon therefore does not significantly improve mass resolution, so in this analysis, silicon hits are not required on tracks.

Central Outer Tracker

The Central Outer Tracker (COT), located around the ISL, is a large open-cell drift chamber used for tracking in the central region ($|\eta| \leq 1.0$) [21]. In the COT, charged particles move through a volume of gas, ionizing the particles therein. An electric field is applied by potential wires and shaped with gold films (field panels) and shaper wires, causing the resulting electrons to drift toward the sense wires.

The COT occupies the region $0.4\text{ m} < r < 1.32\text{ m}$ with full azimuthal coverage, and is 310 cm in length, covering $-155\text{ cm} \leq z \leq 155\text{ cm}$. The tracking volume contains a 50/50 mixture of argon and ethane gases. The wires are arranged into eight superlayers, consisting of twelve sense wires each. Among the eight superlayers, even-numbered layers are parallel to the z -axis, while odd-numbered layers represent small-angle stereo layers, offset by $\pm 2^\circ$ from the z -axis. The azimuthal arrangement of the wires consists of super cells, each of which contains 12 sense wires, separated from adjacent cells by a field panel.

The COT can resolve hit position within approximately 140 nm , and its transverse momentum resolution is $\sigma_{p_T}/p_T \approx 0.0015 \times p_T$. As the original plan for CDF Run II included a possibility to have 132 ns bunch crossings instead of the nominal 396 ns, the COT is designed for a maximum drift time of 100 ns .

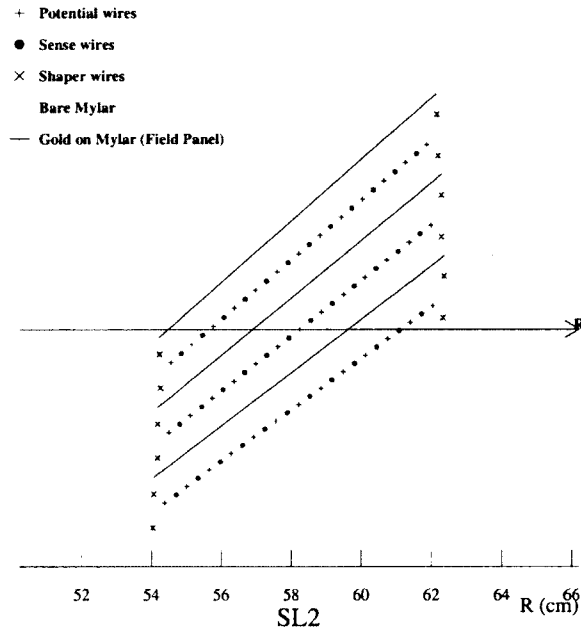


Figure 2.3: The COT consists of cells containing wires and foils to shape the electric field, as well as sense wires.

Time of Flight

Between the COT and magnet solenoid, the Time of Flight (TOF) system is comprised of 3m-long bars of scintillator, measuring 4×4 cm. These bars are arranged, length-wise, along the COT and aid in particle identification. The TOF resolution is of order 100 ps.

2.2.2 Calorimetry

The CDF calorimetry system is designed to measure the energy of through-going particles by sampling the electromagnetic and hadronic showers produced as they traverse the detector. Alternating layers of absorber and scintillator create showers of particles which can be detected by the light they produce in the scintillator lay-

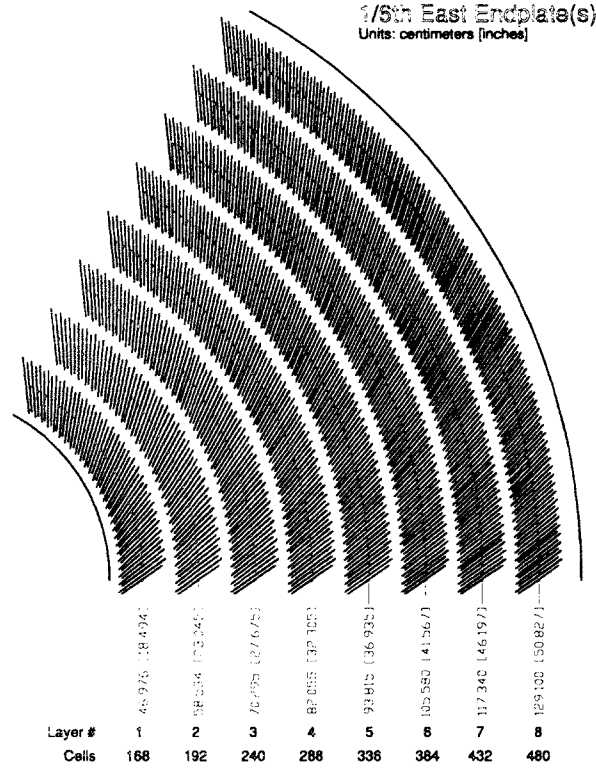


Figure 2.4: A section of the COT east endplate indicates the locations of each super-layer and the configurations of sense and field slots.

ers. The light is captured by photomultiplier tubes and digitized, and this output is proportional to the energy of the incident particle.

The calorimeters cover nearly 4π in solid angle, with different sections of the calorimeter combining to cover the region $|\eta| < 3.6$. The Central Electromagnetic and Central Hadronic calorimeters (CEM and CHA) cover $(0.0 < |\eta| < 1.1)$, with a Wall Hadronic calorimeter extending from $(1.1 < |\eta| < 1.2)$. The Plug calorimeters (PEM and PHA) cover $(1.2 < |\eta| < 3.6)$.

The electromagnetic calorimetry [22] is located directly outside the solenoid, and is designed to measure the energies of electrons and photons. In the EM calorimeters, 4.5 mm layers of lead comprise the absorber, separated by 4 mm layers of scintillator, with wavelength-shifting fibers for readout. Electrons in the lead lose energy through

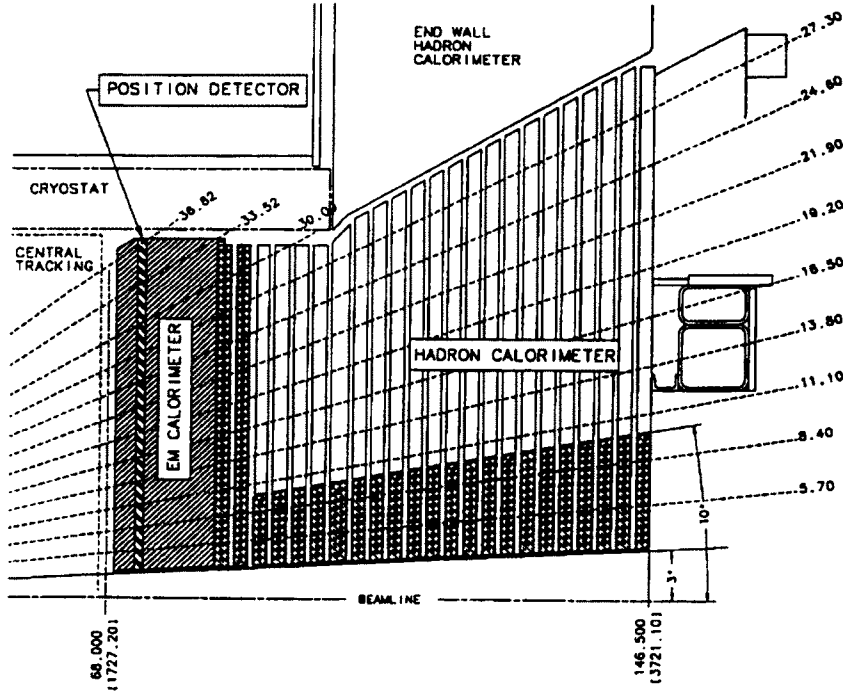


Figure 2.5: A cross-sectional view of the top half of the plug calorimeter system.

Bremsstrahlung, causing showers of particles, while photons cause showers through pair-production. In order to ensure that the entirety of the energy of the showers is collected, there must be a sufficiently thick series of lead-scintillator layers. The CEM is approximately 18 radiation lengths (X_0), where X_0 is the distance over which an electron's energy decreases to $1/e$ of its initial value. Alternatively, X_0 denotes $7/9$ of a photon's mean free path before undergoing pair production. The depth of the PEM calorimeter is approximately $21 X_0$.

Hadronic calorimeters [23] are needed to measure the energies of neutral particles or charged particles that are too heavy to lose much energy from Bremsstrahlung. As such, the hadronic calorimeter systems are designed to measure showers produced when particles interact via strong interactions with nuclei in the absorber. The system is comprised of alternating layers of steel and scintillator, and is 4.5 interaction lengths

Calorimeter Resolution	
Subsystem	Resolution
CEM	$13.7\%/\sqrt{E_T} \oplus 2\%$
PEM	$16\%/\sqrt{E_T} \oplus 1\%$
CHA	$50\%/\sqrt{E_T} \oplus 3\%$
WHA	$75\%/\sqrt{E_T} \oplus 4\%$
PHA	$80\%/\sqrt{E_T} \oplus 5\%$

Table 2.1: Energy resolution of each calorimeter subsystem.

(λ) deep in the central region and 7λ deep in the plug region. λ is defined as the mean distance a hadron travels before interacting with a nucleus in the medium.

For trigger purposes, all of the calorimeter systems are arranged into 'towers,' which are 15° wide in ϕ , and 0.2-wide in η in the central region. In the plug region, some towers are as small as 7.5° in ϕ . Each trigger tower output is digitized with 10 bits of energy resolution, with the smallest bit indicating 125 MeV and the largest at 128 GeV [24]. The energy resolution of each subsystem is given in Table 2.1

In the central and plug regions of the electromagnetic calorimeter, there are two-dimensional readout strip chambers embedded at the depth of the expected shower maximum (around $6 X_0$). These 'showermax' detectors aid in particle identification, by distinguishing pions and photons and help identify electromagnetic showers.

2.2.3 Muon Systems

The calorimeter systems are designed to capture all the energy of particles that enter. As such, most particles do not make it through the calorimeter region. Two notable exceptions are neutrinos, which are only evinced by missing energy and momentum from interactions, and muons, whose mass is too large to lose energy to Bremsstrahlung in the electromagnetic calorimeter. Thus, charged particles escaping

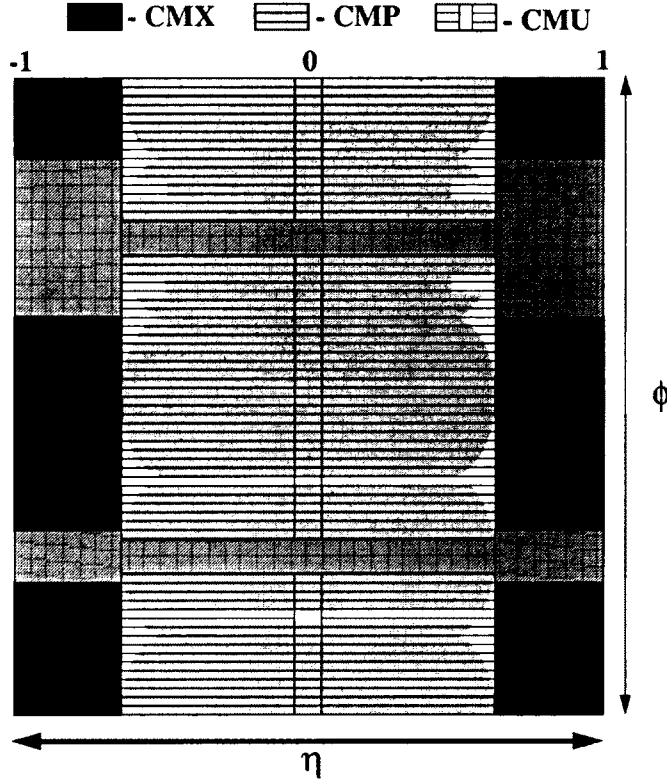


Figure 2.6: The $\eta - \phi$ locations of muon systems. CMU and CMP cover the central η region, where the box-like geometry of the CMP causes its coverage to vary at the edges, seen in gray. The light gray cross-hatched regions are uninstrumented.

the calorimeters with minimal energy loss can be identified as muons. The outermost portion of the CDF detector is dedicated to this purpose. Clusters of hits in muon systems are called 'stubs' and can be linked to tracks in the tracking system to positively identify muons.

The muon systems are comprised of four separate systems. The Central Muon detector (CMU) and Central Muon Upgrade cover the central region of the detector up to $|\eta| < 0.6$, the Central Muon Extension (CMX) covers $(0.6 < |\eta| < 1.0)$, and the Intermediate Muon System (IMU) extends from $(1.0 < |\eta| < 1.5)$.

CMU

The CMU is the original CDF Run I muon system. It is located beyond the CHA and isolated from it by steel shielding. Its operation is similar to the COT, in that it uses a 50-50 argon-ethane gas mixture and sense wires, but in this case, rectangular single-wire drift cells, measuring $6.35 \times 2.68 \times 226$ cm in size, are used instead of a large drift chamber.

As the CMU is placed directly outside of the CHA, it is segmented similarly to the calorimeters. The drift cells are grouped into 24 wedges in ϕ , with one outside of each central calorimeter wedge. The wedges span 12.6° in ϕ , with 2.4° gaps between each wedge. Groups of 16 cells are arranged into 144 modules, four cells deep, with a slight offset in ϕ between alternating layers. Each module spans 4.2° in ϕ , and there are three such modules comprising each wedge. Pairs of two chambers (six to a wedge) are called 'trigger towers,' with gaps between wedges also counting as towers.

The z position of muons can also be determined in the CMU via charge division.

CMP

For Run II, the central muon coverage was updated with the CMP. The CMP is made of single-wire drift tubes 640 cm in length, positioned outside the CMU and an additional 60 cm of steel shielding. The additional steel cuts back on background from particles that escape the calorimeter and pass into the CMU. Thus, tracks with CMU and CMP stubs together form a much purer sample of muons.

CMP cells have a maximum drift time of $1.4\mu\text{s}$. The drift tubes of the CMP are also arranged into four offset layers on four planes, forming a box-like geometry around the detector. This geometry gives rise to slight azimuthal variation in the η coverage. The CMP is lined on the outside (relative to the beam) by a set of scintillation counters known as the CSP. Muons traversing both the CMU and CMP are called 'CMUP muons.'

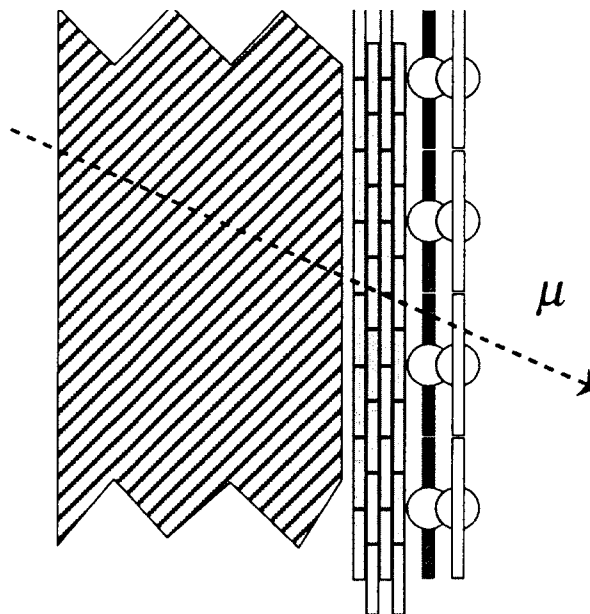


Figure 2.7: The stacked drift cells of the CMP, outside a region of shielding, and the location of the CSP scintillators and photomultiplier tubes. The arrow represents a muon coming from the interaction region.

CMX

The CMX is a system of drift tubes arranged into conical sections at the ends of the CDF detector, extending the rapidity coverage of the muon systems to $|\eta| < 1.0$. Like the CMP, the CMX also features scintillation counters (CSX). The CMX features 15° segments in ϕ , each with 12 drift tubes arranged in four layers. CMX drift tubes are 180 cm in length, but are otherwise the same as CMP drift tubes.

IMU

The IMU extends muon coverage to $|\eta| < 2.0$ with drift chambers and scintillator counters like those of the CMP. However, high backgrounds make it difficult to include in physics triggers.

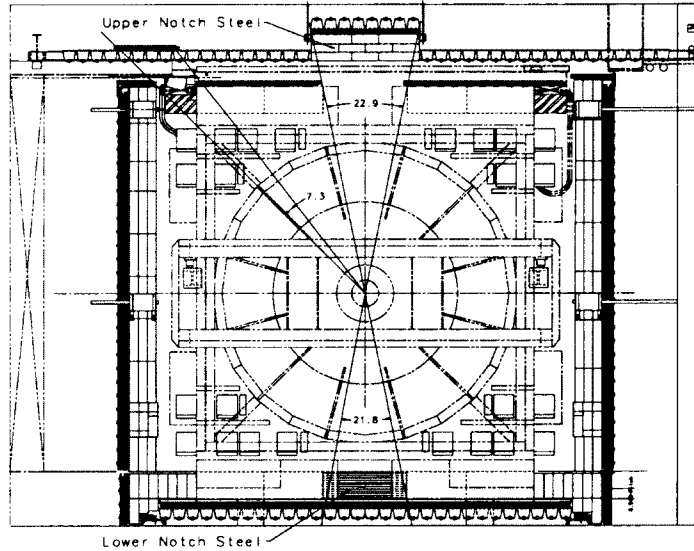


Figure 2.8: The CMP detector shown end-on. PMTs for the CSP are indicated by small circles.

2.3 Trigger System

In order to analyze the collisions that take place at CDF, a method of recording events is necessary. A problem arises because the collision rate at CDF is about 1.7 MHz, with each event taking approximately 170 kB of storage space. CDF is capable of writing up to 40 MB/s to tape, and thus, only a fraction of a percent of all beam crossings can be saved. The trigger system is the means by which interesting physics events are identified and written to tape. The trigger consists of a three-level system, the first and second of which (L1 and L2) are hardware triggers, with the third level (L3) processed at a software level. As of 2007, an upgrade to the trigger system was fully commissioned to help deal with the increasing luminosities reached by the Tevatron [25]. A schematic diagram of data flow in the triggers is shown in Figure

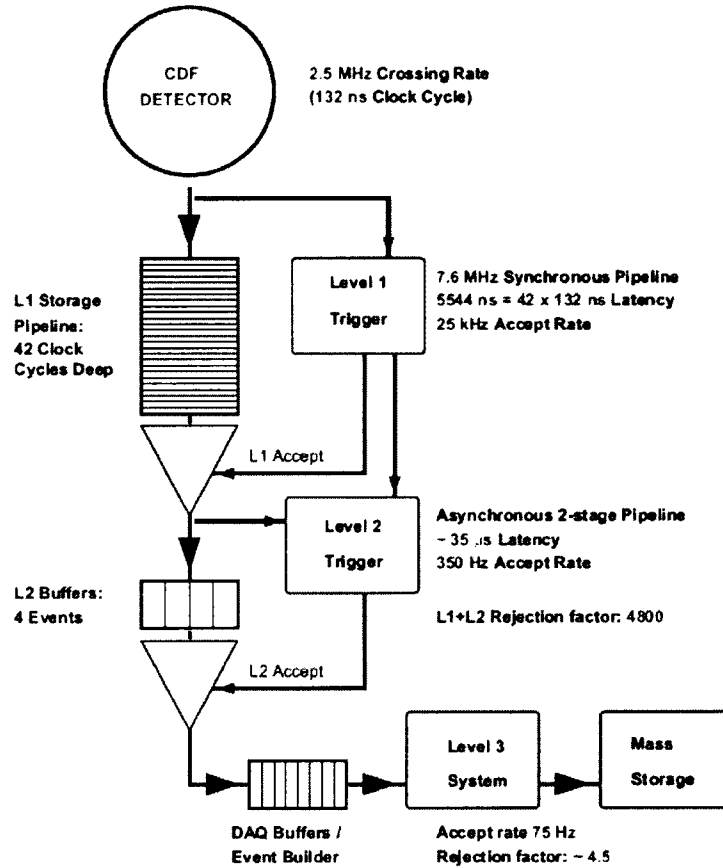


Figure 2.9: The CDF trigger system, with accept rates and latencies (these values are for the period prior to L2 and L3 upgrades).

2.3.1 Level 1 Trigger

The Level 1 system is a deadtimeless hardware trigger which takes information (known as ‘trigger primitives’) from certain detector elements and makes a rapid ($5 \mu\text{s}$) decision on whether to keep an event. The detector subsystems providing information to Level 1 are the COT, the calorimeters, TOF, luminosity counters, and the muon systems. Tracks are identified in the COT by the ‘eXtremely Fast Tracker’ (XFT), which links patterns of hits in the tracking chamber. The Track Extrapolator (XTRP) links COT tracks to muon systems and calorimeters. Level 1 decisions are based on the number of tracks; lepton, photon, or jet candidates; and the total energy or

missing transverse energy of an interaction. Only 8 of the 10 bits of energy resolution from the calorimeters are used at Level 1, with the least- and most-significant bits left out. Many different Level 1 triggers are used, and if an event meets one of them it is passed to the next level. With the incoming 1.7 MHz collision rate, Level 1 accepts events at rates up to 30 kHz.

2.3.2 Level 2 Trigger

Accepted events from Level 1 are passed into one of four Level 2 buffers, which operate with <5% deadtime. Buffering events mitigates event rate fluctuations from the Level 1 trigger. At this level, events are partially reconstructed, taking around 32 μ s of processing time. In addition to the event information used at Level 1, silicon and showermax information are used at this level. The full 10-bit energy resolution from the calorimeters is used at Level 2, and the jet clustering algorithms take place here. Like Level 1, there are a variety of Level 2 triggers, and if any are met, the event is passed to the next level. Level 2 accepts events at a rate of up to 700 Hz, and accepted events undergo full detector readout.

2.3.3 XFT and XTRP Tracking Algorithms

This analysis is heavily dependent on the ability of the trigger system to reconstruct tracks from charged particles in the tracking regions. The XFT [26] is the first step to achieve this. In the plane transverse to the beamline, track momentum and azimuthal angles are measured by searching for track segments in the axial superlayers of the COT. The p_T resolution is σ_{p_T}/p_T^2 2%(GeV⁻¹) and the azimuthal resolution is σ_ϕ 6 mrad, with an efficiency of 96% for tracks with $p_T > 1.5$ GeV/c. The outer stereo layers are also used to reject fake tracks by requiring associated stereo hits.

Tracks from the XFT are sent to the XTRP, which uses look-up tables to extrapolate the tracks to the calorimeters and muon systems. Each central muon system has its own p_T threshold, above which tracks with associated muon system hits will

be passed to L2. The XTRP makes a similar decision based on the energy seen in each calorimeter wedge.

At Level 2, stereo segments are combined with the axial tracks to provide 3D information. The resolution is $\sigma_{cot\theta} = 0.11$ and $\sigma_z = 11\text{cm}$.

2.3.4 Level 3 Trigger

The final step in the trigger system is a software-level system which fully reconstructs events via C++ code using CDF's reconstruction framework. The reconstruction is done by the 'Event Builder' on a large processing farm. Reconstructed events are compared to a set of Level 3 triggers. In the case of muon triggers, Level 3 decisions often consider track p_T and the distance between extrapolated tracks and muon stubs, known as Δ_x . If the criteria of a trigger are met, the event is separated into an output stream based on the type of trigger met and stored. After all three trigger levels, the event rate written to tape is 100Hz.

2.3.5 Upslion Trigger Path

In order to sort events of interest, they must satisfy the criteria of a specific trigger at each level. The set of L1, L2, and L3 triggers required is called a "trigger path." For this analysis, only a single trigger path is utilized in gathering data. That path, called UPSILON_CMU_CMUP, requires a dimuon event with one stub in the CMU and one with stubs in both the CMU and CMP. The relevant requirements are listed in Table [2.3.5](#)

The requirements for this trigger path have remained stable over the data-taking period on which this analysis is based.

UPSILON_CMU_CMUP Trigger Requirements	
L1	No East-West requirement Min. p_T of CMU stub = 1.5 GeV/ c Min. XFT p_T of CMU stub = 1.52 GeV/ c Min. 2 muon trigger towers between stubs
L2	Require CMUP stub Min. XFT p_T of CMUP stub = 3.04 GeV/ c Require CMU stub Min. XFT p_T of CMU stub = 1.52 GeV/ c
L3	(CMU μ) CMU stub $\Delta x < 30$ cm (CMU μ) CMU stub $p_T > 3.0$ GeV/ c (CMUP μ) CMP stub $\Delta x < 40$ cm (CMUP μ) CMU stub $\Delta x < 15$ cm (CMUP μ) CMUP stub $p_T > 4.0$ GeV/ c $8.0\text{GeV}/c^2 \leq m_{\mu\mu} \leq 12.0\text{GeV}/c^2$ Require Opposite Charge

Table 2.2: L1, L2, and L3 requirements for UPSILON_CMUP_CMU trigger path.

Chapter 3

Simulation

This analysis utilizes a set of Monte Carlo templates which represent the shapes of purely transverse or longitudinal distributions as they would be observed by CDF. The acceptance and efficiency of the CDF apparatus act to modify the angular distribution and yield of Υ mesons. These effects vary with spin alignment. For these reasons, the template method employed in this analysis accounts for any such effects by applying the CDF detector simulation, production, and data-driven trigger efficiency function to the Monte Carlo events before the polarization fitter compares the distributions with data. The data-driven CMU trigger efficiency developed for the $B^0 \rightarrow \mu^+ \mu^-$ search is applied in the construction of the templates to account for CDF dimuon trigger efficiencies [27]. The CMP efficiency measurement is described later in this note.

3.0.6 Monte Carlo Generation

The CDF simulation package, MCProduction, is used for Monte Carlo generation. Events consisting of a single $\Upsilon(nS)$ are generated using FAKEEVENT. The Υ particles are produced according to a flat $p_T(\Upsilon)$ spectrum in each of several bins (eight, four, and four bins for $\Upsilon(1S)$, $\Upsilon(2S)$, and $\Upsilon(3S)$, respectively) covering the region $2 \leq p_T \leq 40$ GeV/ c . The specific bin boundaries are listed in various tables, e.g., Tables 5.2, 5.4

The Υ events are generated with uniform distributions in rapidity for $|y| < 0.8$ and uniform over the full range of ϕ . The generated Υ is decayed to two muons using the EvtGen package, with a fully transverse (T) or fully longitudinal (L) polarization. Having been decayed, the events are passed to CDFSIM and Production to simulate detector response and reconstruction effects. In CDFSIM, simulated particles are passed through a model of the CDF detector using GEANT3 [28] to emulate energy loss through multiple scattering and interactions in the material. TrigSim, which simulates CDF triggers, is executed as a part of the standard MCProduction chain, though its results are not applied in this analysis. The number of events generated per $p_T(\Upsilon)$ bin is the same for both polarizations. Differences in acceptance for T and L polarizations cause Monte Carlo yields for each template to be somewhat different.

Because detector response is not constant over time, and because trigger rates vary due to luminosity-based prescaling, it is important to generate simulations that represent the conditions in which the data was produced. As such, for this analysis, a run range consistent with data (*i.e.*, 184062-287261) is used, with a requisite minimum integrated luminosity per run of 1.5 pb^{-1} to keep the number of jobs manageable. This results in a total of 579 runs simulated, each comprising a relative number of events proportional to its integrated luminosity.

3.0.7 Acceptance and Efficiency

The Monte Carlo production chain creates a large set of simulated events and models detector response and event reconstruction. The effects of triggers and detector efficiencies must still be added to create an accurate depiction of real events found in the data.

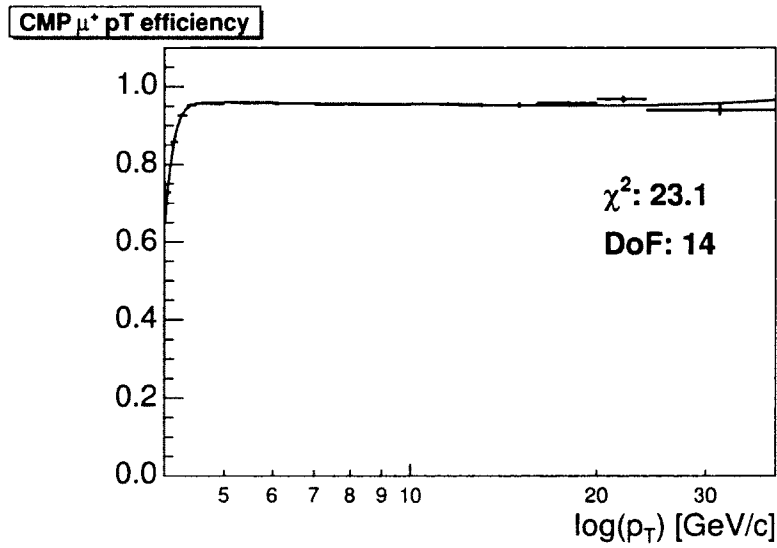
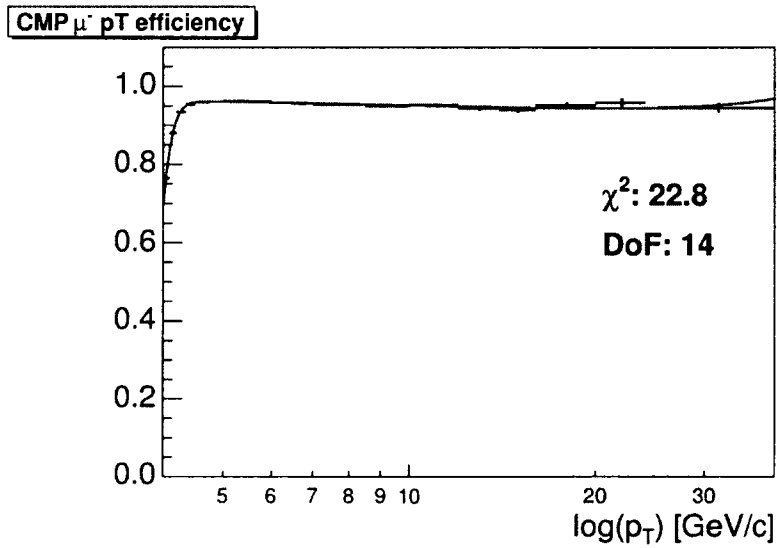
As trigger effects modify the decay angular distribution of real events, several methods are used to simulate the respective modifications made by different detector systems. For instance, to incorporate the trigger efficiency of the CMU detector to Monte Carlo events, we utilize the data-driven trigger efficiency functions from the

$B^0 \rightarrow \mu^+ \mu^-$ search. These functions characterize the efficiencies of dimuon and single-muon triggers as a function of trigger type and run number, as well as the type, p_T , η , and ϕ of each muon. Because the dimuon efficiencies provided in that study are not tested for dimuon masses $> 6\text{GeV}/c^2$, we use the product of the two muons' L1 single-muon efficiencies. The two muons come from the decay of a high mass state, so there is very little chance that they will sample the same COT cell and have a correlated inefficiency.

Unfortunately, CMP-based triggers, like the one used in this analysis, are not included in the package. Because we utilize a CMUP trigger, we calculate an additional efficiency for the CMP and apply it in the same way. Considering the fact that all muons used in this analysis have come from decays which have satisfied the trigger, care must be taken to avoid a biased sample. The trigger requires one CMUP muon and one CMU muon, which provides a way to isolate an unbiased sample. The charge of each muon is known from its curvature in the tracking volume, so all positively- or negatively-charged muons can be evaluated. Selecting events wherein the μ^+ is a CMUP muon gives a sample of μ^- that is unbiased by the requirement for a CMUP muon. Then, μ^- properties are checked against CMUP trigger requirements. The number of events in which CMUP requirements are met and the CMUP trigger bit is set is compared to the total number of events in which CMUP requirements are met to determine the efficiency. The operation is then re-done with the charges swapped, *i.e.*, selecting events with a CMUP μ^- and checking μ^+ trigger requirements. This allows for different efficiencies depending on muon charge.

After performing this operation, we find that the CMP efficiency is flat in η and varies with p_T as demonstrated in Figures [3.1](#) and [3.2](#). We fit the μ^+ and μ^- distributions separately, finding the PDFs in Equations [3.1](#) and [3.2](#) best describe CMP efficiency functions.

Each event in our Monte Carlo sample is tested against the CMU and CMP efficiency functions and is kept or discarded based on the calculated efficiency. Because

Figure 3.1: Measured CMP efficiency for μ^+ .Figure 3.2: Measured CMP efficiency for μ^- .

the number of muons available attenuates rapidly above 30 GeV/ c , the CMP functions are based on muons with p_T less than 35 GeV/ c . Any muon with p_T in excess of that value is treated as having exactly 35 GeV/ c to avoid potentially nonphysical behavior of the efficiency function. The number of events for which this is an issue is vanishingly small.

$$\epsilon_{\mu^+}(p_T) = (0.969 + 0.0023 \times p_T + 0.000071 \times p_T^2) / \{1 + \exp[-9.84 \times (p_T - 3.93)]\} \quad (3.1)$$

$$\epsilon_{\mu^-}(p_T) = (0.975 + 0.0033 \times p_T + 0.000096 \times p_T^2) / \{1 + \exp[-9.83 \times (p_T - 3.91)]\} \quad (3.2)$$

The Monte Carlo events are processed in a FakeEvt + EvtGen, CdfSim, Trigsim++, Production sequence. We do not test the trigger bits set in Trigsim++ but use cuts to simulate the L1, L2, and L3 triggers. In order to apply the trigger efficiency as discussed above, one must apply a set of selection cuts that emulate the XFT requirements by quantizing ϕ_{SL6} in 1.25-degree segments and removing events in which both muons hit the same segment. The trigger tower requirement on muon ϕ separation is imposed by quantizing each muon's ϕ angle into 5-degree segments. Muon pairs must have at least two tower separation (gaps between adjacent segments count as a tower for this purpose) to satisfy the trigger tower requirement. Applying these cuts to data is redundant with hardware and therefore removes very few events. Trigger emulation requirements are listed in Table [3.0.7](#)

3.0.8 Monte Carlo re-weighting

The Monte Carlo is generated with a flat $p_T(\Upsilon)$ distribution in each $p_T(\Upsilon)$ bin. However, the corresponding data has a smooth, continuous distribution which is not flat. Because the detector acceptance is p_T dependent and the Υ polarization itself is p_T -dependent, the use of a flat distribution can cause a systematic error in the measurement, especially for bins covering a large range of p_T . To avoid this, the Monte Carlo events are reweighted to match the data p_T distribution after (polarization-dependent)

Cuts	
Basic Offline Cuts	Require CMU or CMUP muons $n_{ctaxial} \geq 10$ $n_{ctstereo} \geq 10$ $ z_0 \leq 60\text{cm}$ $ \Delta z_0(\mu^+, \mu^-) \leq 5\text{cm}$ $ z_{SuperLayer} \geq 1.5\text{cm}$ $ z_{COTexit} \leq 155\text{cm}$ $\mu\mu$ Vertex Fit Prob ≥ 0.001 $\sigma L_{xy} \leq 0.025\text{cm}$
Trigger Cuts	CMU Muon: $p_T \geq 3.05$ GeV, CMUdx $\leq 30\text{cm}$ At least 1 CMUP Muon CMUP Muon: $p_T \geq 4.05$ GeV/c, CMUdx $\leq 15\text{cm}$ Each μ has matched XFT track Min. 2 trigger towers between hits

Table 3.1: Selection cuts required for data and Monte Carlo, as well as L3 trigger requirements imposed in the form of cuts.

acceptance and efficiency losses. This ensures that each bin has the appropriate p_T weight despite the flat generation. To account for the polarization dependence effects, the reweighting procedure must be iterative. First, the polarization analysis is carried out based on Monte Carlo templates with a flat $p_T(\Upsilon)$ spectrum. The results of that analysis are used to combine T and L templates, producing a representation of data with the appropriate polarization. The p_T distribution of this combined template is compared to that of data, and weights are calculated in each $p_T(\Upsilon)$ bin to match the shapes, as described below. The templates are then re-processed with these weights applied, and the resulting, new templates are used to carry out another polarization measurement, thus beginning the next iteration. The process continues until the polarizations cease to vary from one iteration to the next in a statistically significant way. Happily, these polarizations stabilize after a single application of the weights.

To extract the signal $p_T(\Upsilon)$ distribution, the reweighting procedure uses a background-subtraction method. The background p_T distribution under the signal peaks is estimated using a low-mass sideband below the 1S peak, from 9.1-9.225 GeV/c²; a mid-mass sideband between 1S and 2S peaks, from 9.65-9.775 GeV/c²; and a high mass sideband above the 3S peak, from 10.55-10.675 GeV/c². The mass distribution in a given p_T bin is fitted with a 3rd-order Chebyshev Polynomial background shape and the decay-angle-integrated mass probability distribution functions for each peak that are described in section [4.3.1](#). The sideband distributions represent the background p_T distribution. This background shape is extrapolated into the signal region and subtracted from the p_T distribution in the signal region. The background of the $\Upsilon(1S)$ is represented by the nearby low-mass and mid-mass sidebands, while the $\Upsilon(2S)$ and (3S) are represented by the mid-mass and high-mass sideband regions. Despite a large distance between the sidebands used for the latter two peaks, the background p_T spectrum over that range is stable, as demonstrated in Figure [3.3](#)

Once signal-region p_T distributions are determined for each state and p_T bin, they are fitted with an exponential probability distribution function. This PDF represents

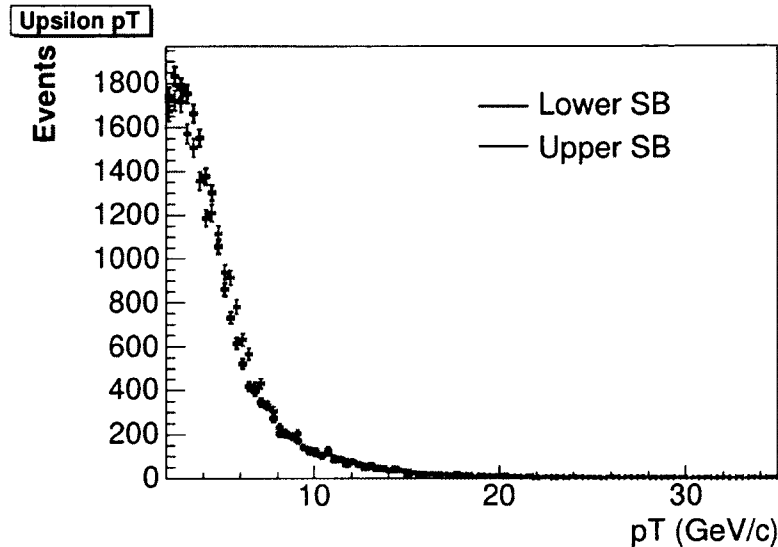


Figure 3.3: Dimuon p_T of events in the sideband regions for the 2S and 3S states. The distributions are quite stable over that range.

the probability that a detected event in that bin has a certain p_T . In the corresponding Monte Carlo p_T bins, the initially-flat p_T distribution is separated into ten sub-bins. A p_T weight function is determined from the exponential fit by evaluating the resulting function at the center of each sub-bin. The Monte Carlo population is reweighted so that its p_T distribution accurately reflects the data distribution over the p_T interval while preserving the number of Monte Carlo events in the $p_T(\Upsilon)$ bin. The new, reweighted Monte Carlo templates are used to determine the next iteration of the polarization. The changes in polarization for successive iterations are listed in Table 3.2. Happily, only one iteration is needed for any of the states or bins.

The effects of reweighting the Monte Carlo in dimuon rapidity were considered as well. The Monte Carlo y distribution integrated over p_T agrees well with that from data for $|y|_\Upsilon < 0.6$. Thus, no y reweighting is required, and only p_T reweighting is used in the final measurement. The y distribution for data and Monte Carlo are shown in Fig. 3.5 and 3.6

Effects of pT reweight on polarization			
$\Upsilon(1S)$ p_T bin	$\Delta\eta(\sigma)$, no rwt	$\Delta\eta(\sigma)$, first rwt	$\Delta\eta(\sigma)$, second rwt
2-3	-	0.5	0
3-4	-	0	0
4-6	-	15.0	0
6-8	-	4.3	0
8-12	-	0.3	0
12-16	-	1.0	0.1
16-21	-	1.0	0
21-40	-	5.7	0.1

Table 3.2: The polarization may change significantly after a single reweight, but thereafter it is highly stable with respect to further iterations. This table shows how significant the change in polarization is after each iteration, in units of σ_η , or the uncertainty on the fit value of the longitudinal polarization fraction. The $\Upsilon(2S)$ and $(3S)$ polarizations behave similarly.

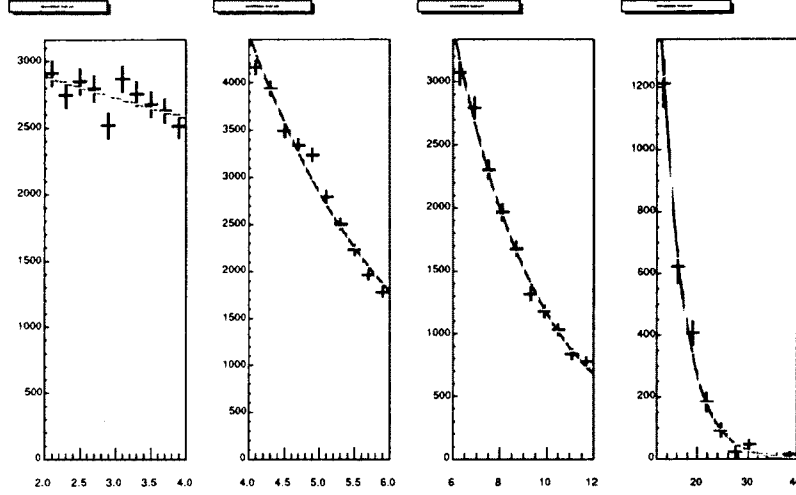


Figure 3.4: Effects of a single iteration of re-weighting Monte Carlo samples for the $\Upsilon(2S)$. Data is shown in black, the exponential fit in red, and reweighted Monte Carlo in cyan. Monte Carlo samples are generated flat in each bin.

3.0.9 Angular Binning and p_T Resolution

To demonstrate the dependence of Υ polarization on p_T , events are sorted into p_T and $\cos \theta^*$ bins. The Υ p_T binnings are listed in Tables [5.2](#), [5.3](#) and [5.4](#). The $\cos \theta^*$ distribution is folded about 0, exploiting parity invariance in the decay, and the bins are chosen to have a width of 0.1 to ensure good statistics. The equivalence of the folded and unfolded distributions has been checked in two ways. Firstly, the polarization remains unchanged when the polarization angle is defined from the negative muon instead of the positive one. Secondly, the $\cos \theta^*$ distribution at $\cos \theta^* < 0$ agrees well with the positive half of the distribution when the two halves are overlaid on the same axis. For example, the folded angular distribution of the $\Upsilon(1S)$ is shown in Fig. [3.7](#)

The significance of bin migration effects is checked by determining from Monte Carlo the resolution for p_T and $\cos \theta^*$ for the $\Upsilon(1S)$. This is done by comparing these

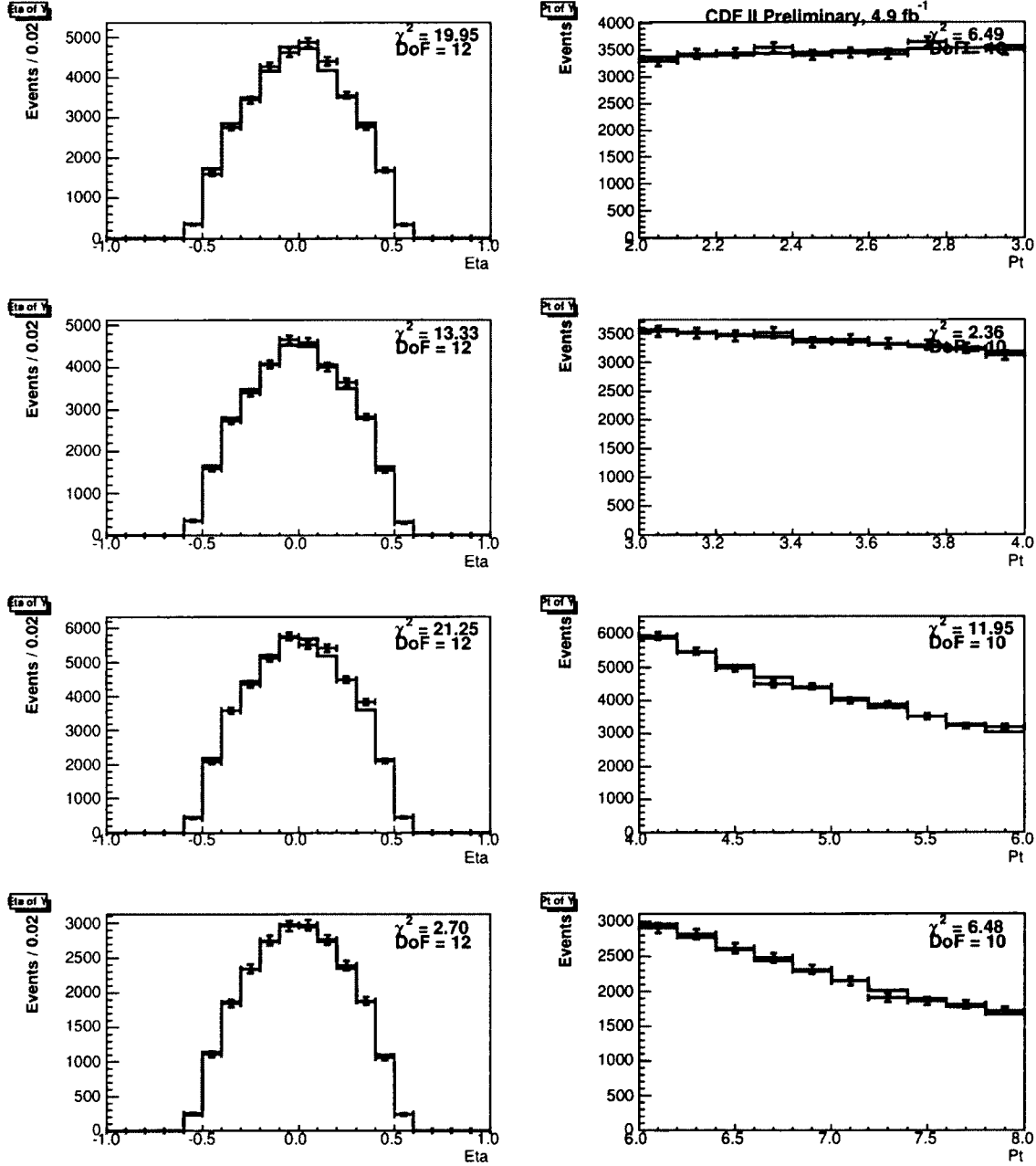


Figure 3.5: Sideband-subtracted data (points) and Monte Carlo (solid line) rapidity and p_T distributions of Υ , for the first four p_T bins, based on 4.9 fb^{-1} .

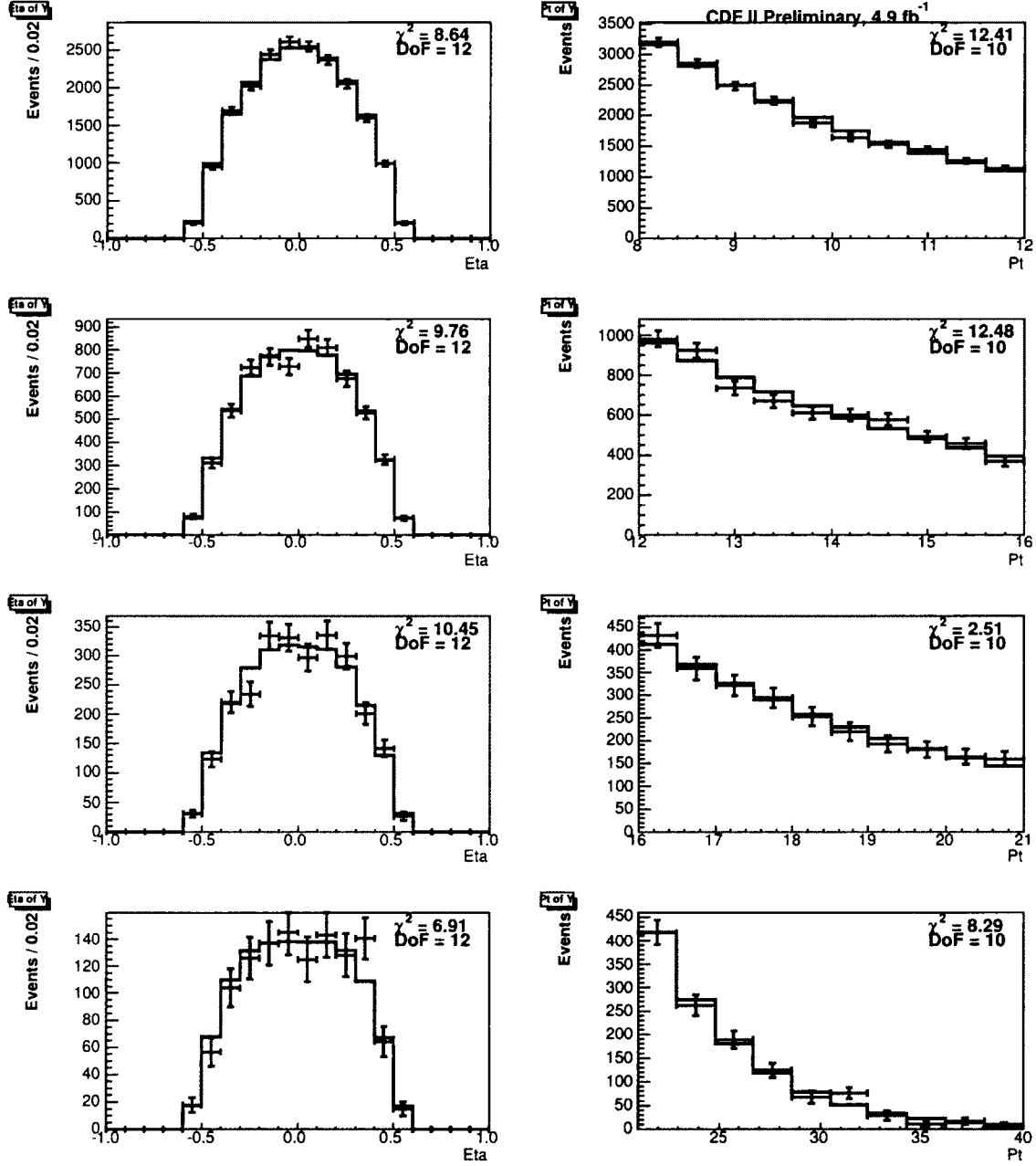


Figure 3.6: Sideband-subtracted data (points) and Monte Carlo (solid line) rapidity and p_T distributions of Υ , for the last four p_T bins, based on 4.9 fb^{-1} .

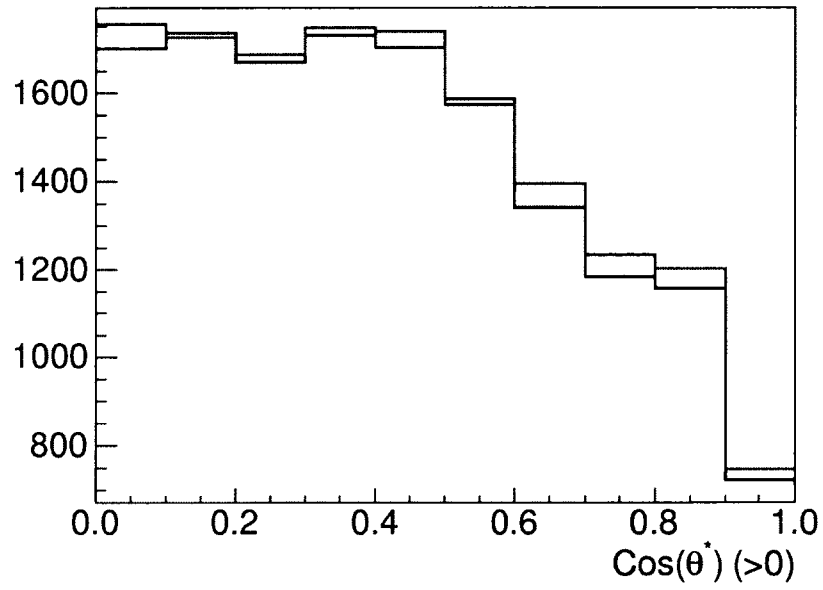


Figure 3.7: An example of the symmetry about zero of the angular distributions. This plot shows the signal-region angular distribution (including background) for the first p_T bin of the $\Upsilon(1S)$. The red histogram is $|\cos \theta^*|$ for $\cos \theta^*$ values less than zero; black is the positive portion of the distribution.

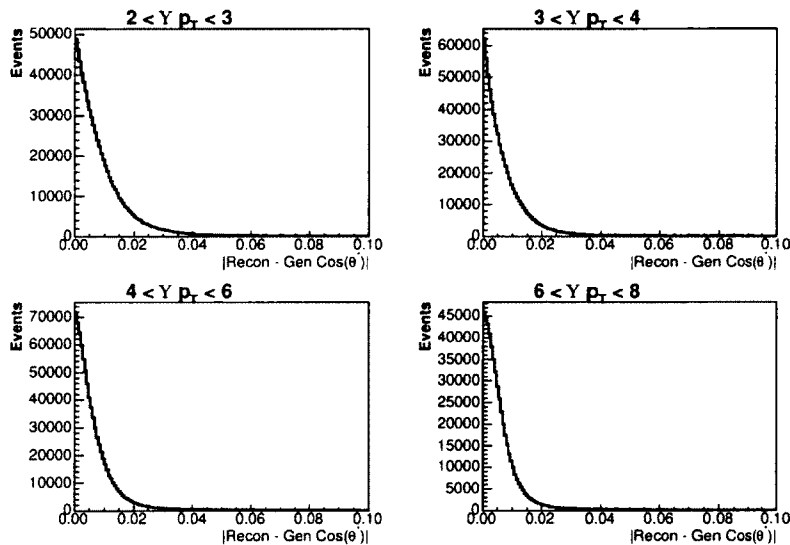


Figure 3.8: Absolute value of the difference between reconstructed $\cos \theta^*$ and generator values for the first four p_T bins. The resolution shown is much smaller than the bin sizes, so event migration effects are considered negligible.

quantities as measured using generator-level information against fully-reconstructed events. The results are featured in Figures [3.8](#) - [3.11](#). Because the shapes are not easily fit by a simple Gaussian, an approximate width is determined by folding the difference distributions about zero and then determining the region that contains 68% of the total yield for that bin. In the absence of a fit, we must choose a region that ends on a bin boundary for ease of enumeration. Therefore, we take the upper end of the bin containing the 68th percentile as the (slightly conservative) estimate. The results are shown in Tables [3.3](#) and [3.4](#). The resolution in all cases is much smaller than the bin width.

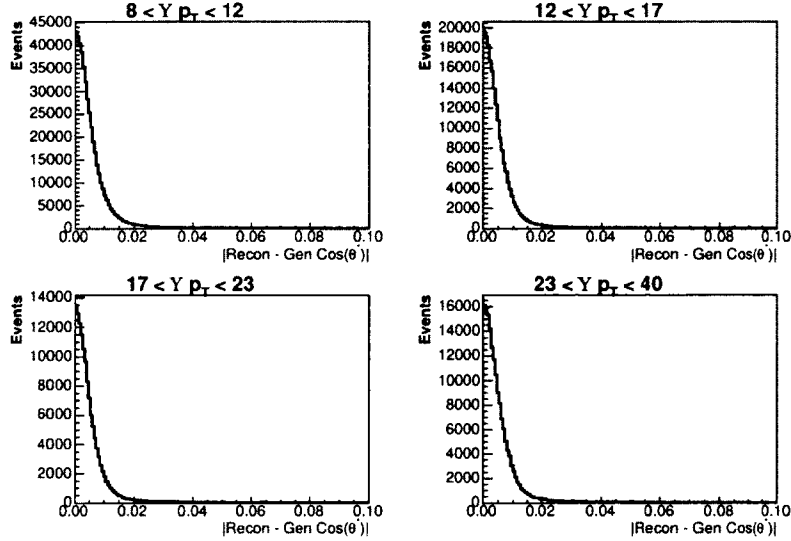


Figure 3.9: Absolute value of the difference between reconstructed $\cos \theta^*$ and generator values for the last four p_T bins. The resolution shown is much smaller than the bin sizes, so event migration effects are considered negligible.

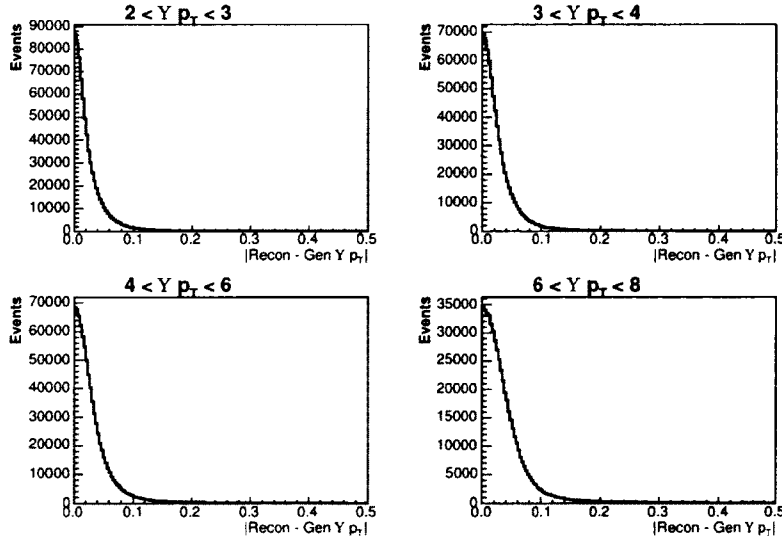


Figure 3.10: Absolute value of the difference between reconstructed $\Upsilon(1S)$ p_T and generator values for the first four p_T bins. The resolution shown is much smaller than the bin sizes, so event migration effects are considered negligible.

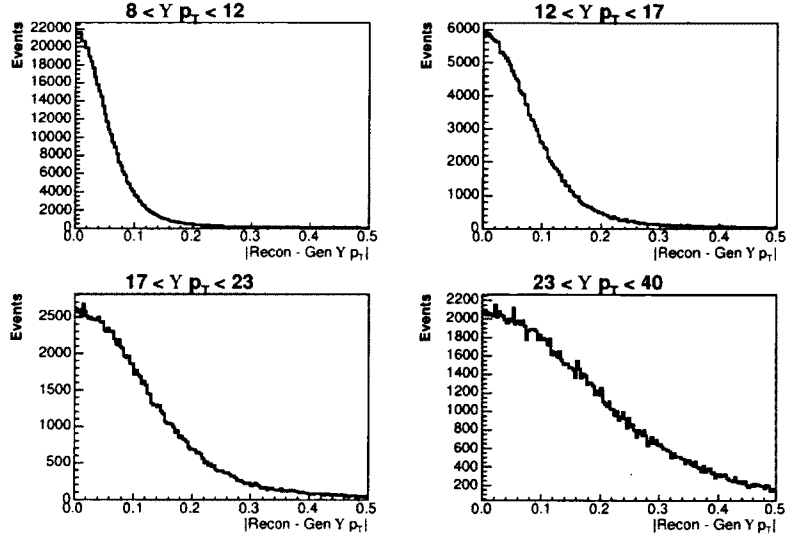


Figure 3.11: Absolute value of the difference between reconstructed $\Upsilon(1S)$ p_T and generator values for the last four p_T bins. The resolution shown is much smaller than the bin sizes, so event migration effects are considered negligible.

$\Upsilon(1S) \cos \theta^*$ Resolution		
p_T bin	Percentile	Resolution
2-3	68.74	0.011
3-4	69.14	0.009
4-6	70.55	0.007
6-8	71.14	0.007
8-12	71.21	0.006
12-17	70.17	0.006
17-23	70.41	0.006
23-40	68.07	0.006

Table 3.3: $\cos \theta^*$ resolution determined from $\Upsilon(1S)$ Monte Carlo. The listed percentile indicates the portion of events within a region ending on a specific bin boundary.

$\Upsilon(1S)$ p_T Resolution		
p_T bin	Percentile	Resolution (GeV/c)
2-3	70.57	0.030
3-4	70.30	0.033
4-6	69.59	0.037
6-8	68.24	0.043
8-12	68.96	0.060
12-17	69.67	0.090
17-23	68.89	0.133
23-40	68.18	0.197

Table 3.4: $p_T(\Upsilon)$ resolution in GeV/c determined from $\Upsilon(1S)$ Monte Carlo. The listed percentile indicates the portion of events within a region ending on a specific bin boundary.

3.0.10 Test of Monte Carlo using μ^+ distributions in p_T and

η

To check the validity of the Monte Carlo acceptance calculations, we compare the measured distributions of μ^+ mesons from Υ decay to the polarization-weighted Monte Carlo predictions for the μ^+ . Unlike the polarization analysis, which fits for the background in each angle bin, the μ^+ comparisons rely on sideband subtraction for the data. At low p_T especially, there is a sizeable background subtraction. The background changes exponentially in normalization as one moves from the low sideband to the high sideband. This means that assuming a linear average behavior for the background shape as one varies the dimuon mass may not be a completely satisfactory approximation. The effects of a non-linear behavior of the $p_T(\mu^+)$ distribution can be seen in Fig. [3.12](#). The average of the upper and lower distributions produces some peaks and dips at low muon p_T . A small residue of this behavior can be seen by com-

paring the background distributions to the sideband-subtracted μ^+p_T distributions in Fig. [3.13](#). The η plots are not affected by this kind of background shape change. Overall the distributions match well in shape for all $p_T(\Upsilon)$. There is no indication of a mismatch between the polarization-weighted Monte Carlo predictions and the data distributions.

After having applied all the necessary trigger and acceptance cuts and efficiencies, the templates should be a good representation of what the data will hold. The agreement between data and MC in the single-muon distributions is a good sign that the templates are up to the task of measuring a polarization.

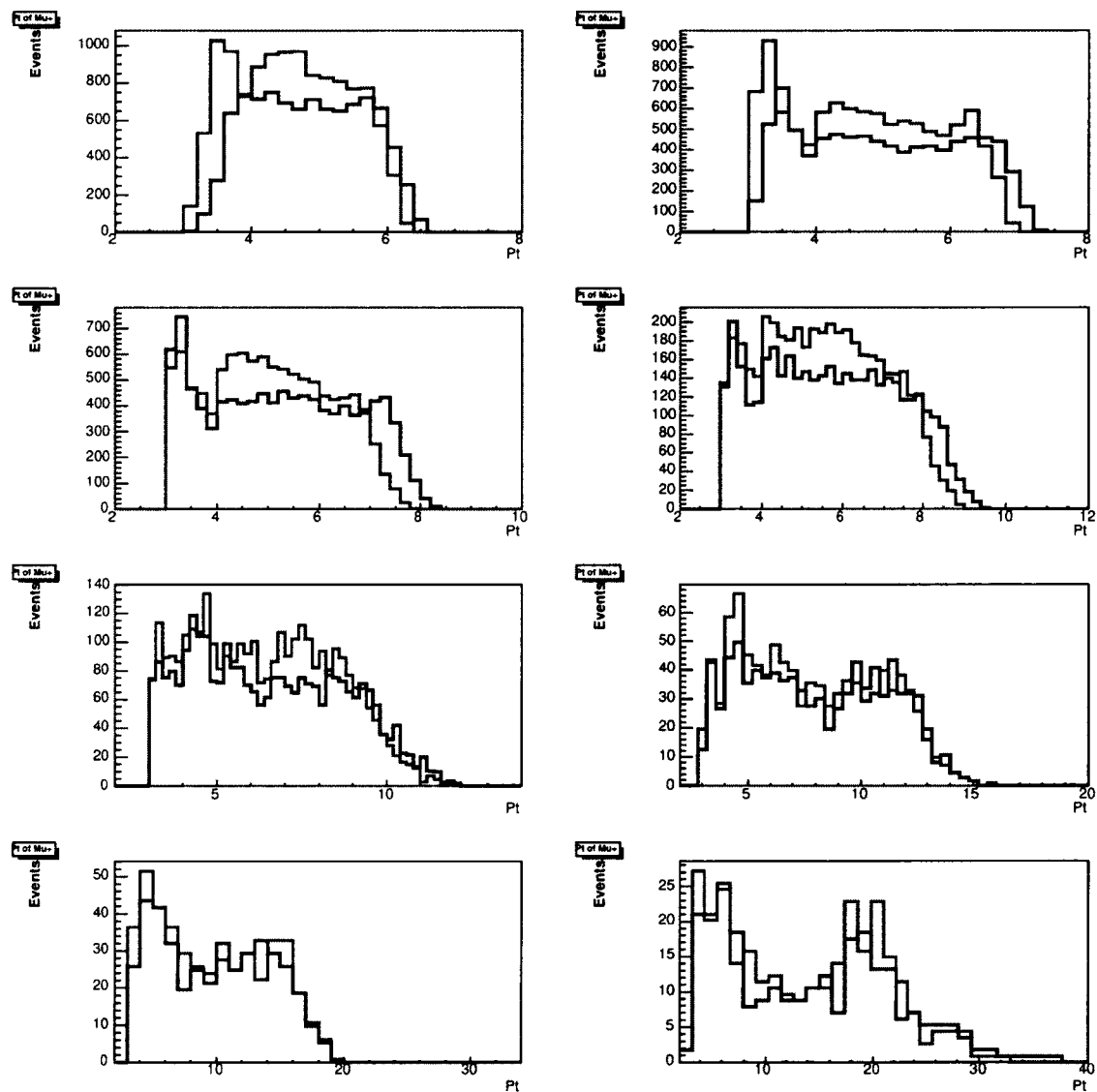


Figure 3.12: μ^+p_T distributions for the sideband regions used for $\Upsilon(1S)$. The lower (“low-mass”) sideband is indicated by the red line, while the upper (“mid-mass”) sideband is shown in black.

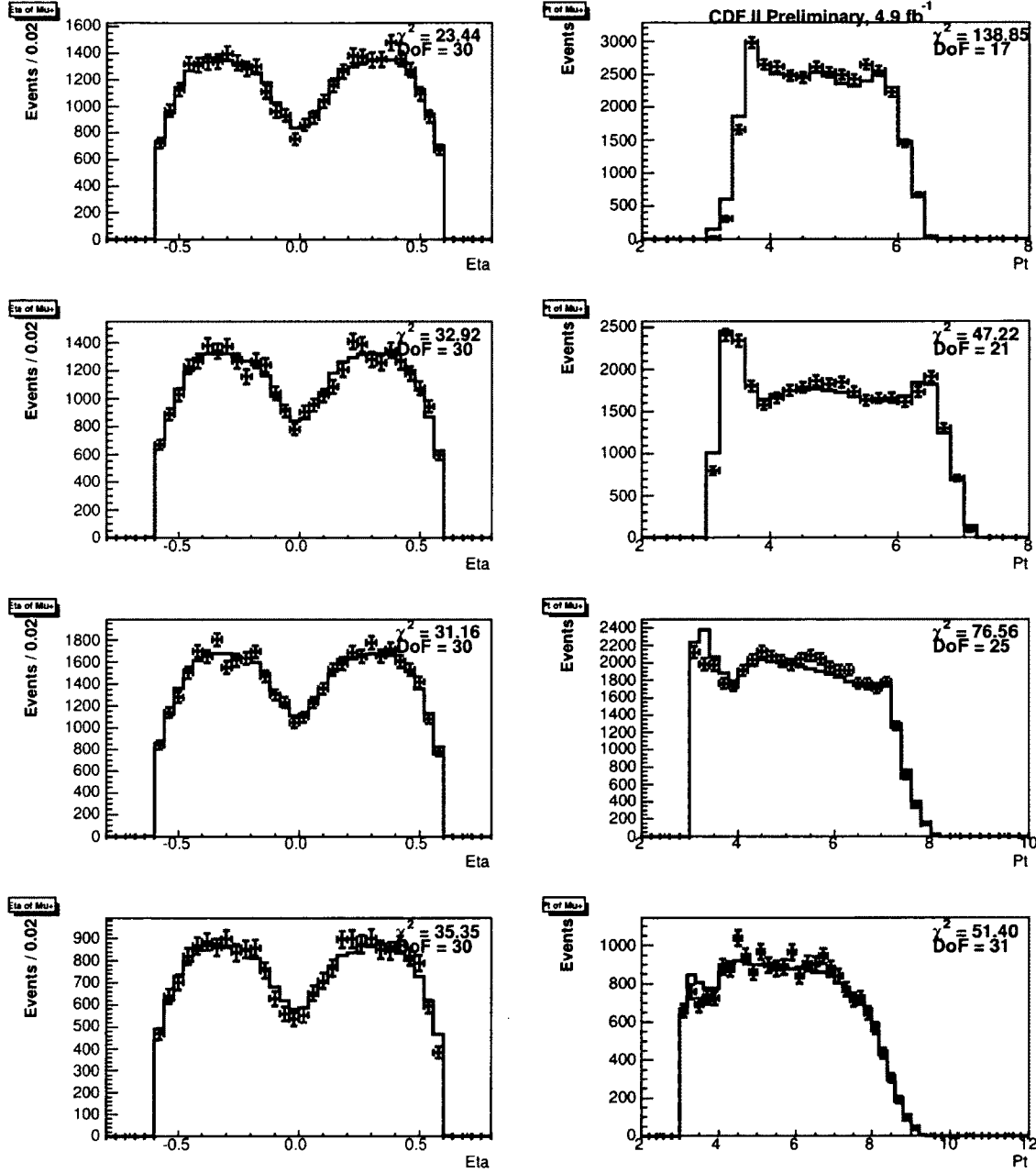


Figure 3.13: Sideband-subtracted data (points) and Monte Carlo (solid line) rapidity and p_T distributions of muons, for the first four p_T bins, based on 4.9 fb^{-1} .

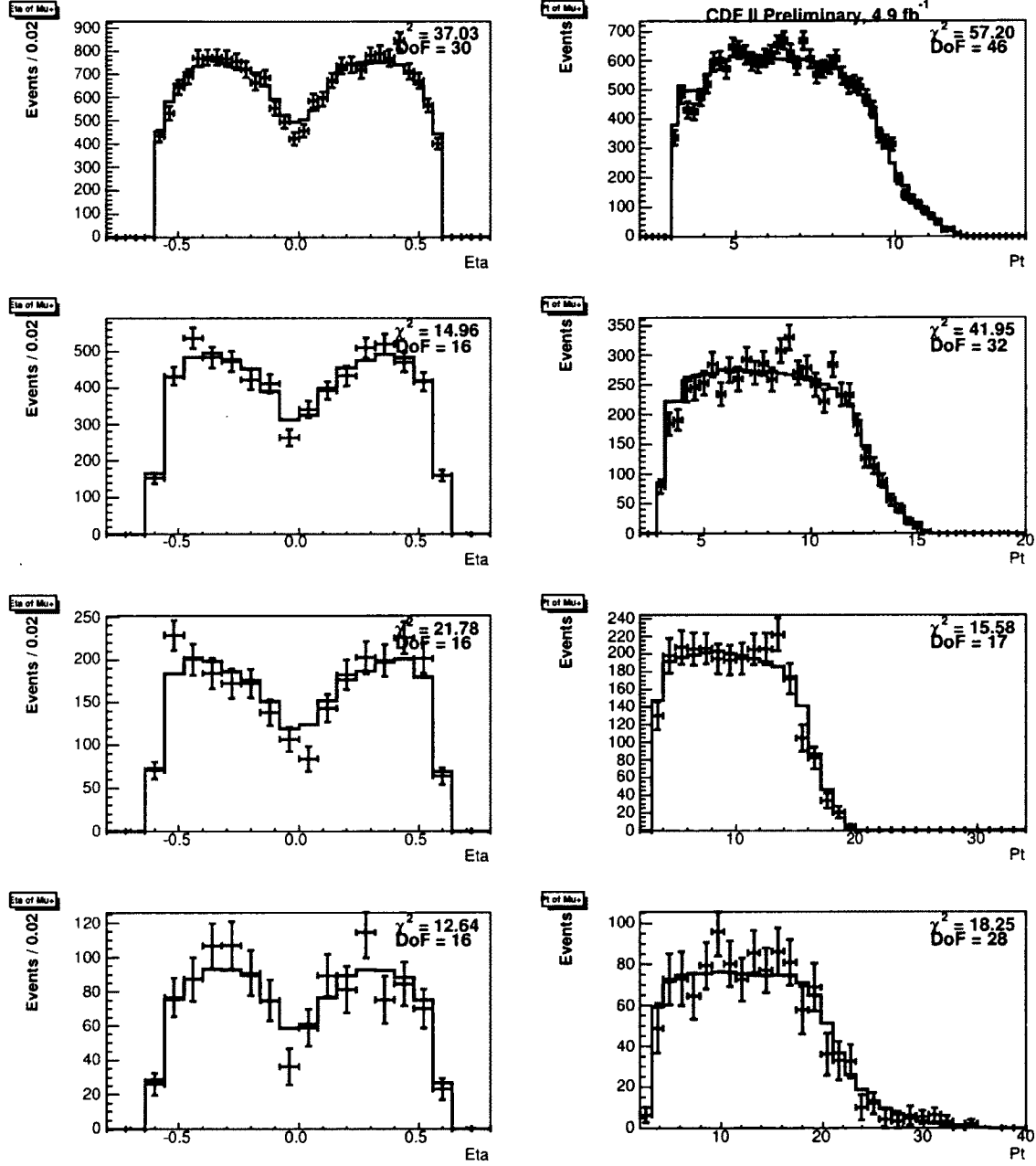


Figure 3.14: Sideband-subtracted data (points) and Monte Carlo (solid line) rapidity and p_T distributions of muons, for the last four p_T bins, based on 4.9 fb^{-1} .

Chapter 4

Data Treatment and Spin Alignment Analysis

With Monte Carlo templates in hand, the next step is to turn to the data. Steps must be taken to ensure the quality of the data sample, and then a strategy must be developed to extract the angular distribution of real events among polarized background. Without a clean sample, there is no way to accurately match templates to the distribution. The methods used to obtain the angular distribution of data are explained herein, as well as the polarization analysis itself.

4.1 Data Processing

The dataset used for this analysis comes from a single trigger path, `UPSILON_CMU_CMUP`. The trigger requirements are emulated in Monte Carlo, but are selected in data by a utility, called `TPrereqFast`, that verifies the desired trigger bits. Data events that have met the appropriate trigger criteria must pass all the same cuts as Monte Carlo events, including trigger emulation. Many of the cuts are designed to remove events with poor track quality, and are equally necessary in data and simulation. Others, such as trigger cuts, are applied to data because they are necessary in Monte Carlo,

and identical treatment of each helps avoid dissimilarities that could lead to systematic effects. Once cuts are applied, the business of extracting the angular distributions of each state begins.

4.2 Backgrounds

The Υ peaks are clearly distinguished by the CDF detector, but there is significant background under each peak, as demonstrated in Figure 4.1. The primary sources of background are Drell-Yan events and hadron decay muons. Drell-Yan muons are the result of quark-antiquark annihilation from the hadron beam, which (in the Υ mass range) produces a virtual photon which decays into a dimuon. Pions and kaons can contribute to the background when the particles from their showers in the outer region calorimeter find their way into the muon systems. In concert with a real muon, this may fire the Υ trigger. The trigger and track quality cuts reduce these backgrounds as much as possible, but dimuons in the appropriate mass window cannot be distinguished from real events. This causes a continuum of background under the peaks. The method of this analysis, described in this chapter, is designed to reliably extract signal distributions from the dataset with minimal influence by the background.

4.3 $\Upsilon(nS)$ Polarization Analysis

The $\Upsilon(nS)$ studies use events from a dimuon mass interval from 8.82-10.98 GeV/c². For a given state and a given p_T bin the polarization analysis requires histogramming the angular distribution of those decays. This, in turn, requires a determination of the $\Upsilon(nS)$ yield in each $\cos\theta^*$ bin. In order to achieve this, the data, already split into p_T bins for each state, are further separated based on their angular distribution. By invoking parity conservation in the decay, the events are organized into ten bins

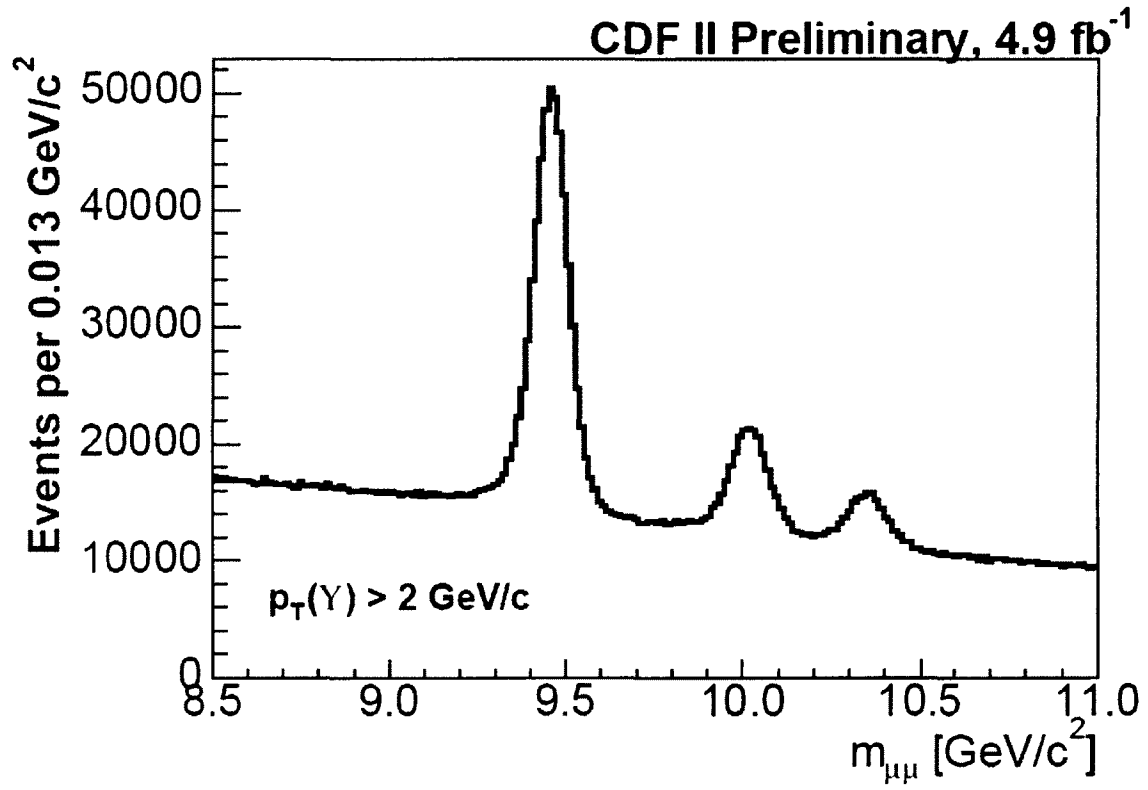


Figure 4.1: The dimuon mass distribution of trigger events, before any cuts are applied.

of $|\cos \theta^*|$ on the interval (0,1.). The dimuon masses of these events are used to generate mass histograms over the aforementioned range. In each $|\cos \theta^*|$ bin we make a fit over the entire region, including all three $\Upsilon(n\text{S})$ peaks plus a Chebyshev polynomial background function. This process is repeated for each p_T bin. For the $\Upsilon(1\text{S})$ analysis, we have 8 bins. Because the higher-mass states have lower yields, the $\Upsilon(2\text{S})$ or $\Upsilon(3\text{S})$ polarization calculations are not based on their yields from the 1S binning, even though the mass fit includes all three states. For the $\Upsilon(2\text{S})$ or $\Upsilon(3\text{S})$ yields we rebin the data into four p_T bins and repeat the analysis procedure.

Beneath the three peaks, the background is unconstrained by physics considerations. Determining the best description of the background is somewhat tricky due primarily to the varying background shapes over the range of $\cos\theta^*$ bins. We evaluated the utility of the following method [29]. We fit with a large number of Chebyshev polynomials and truncate the series when, scanning backward from the highest-order polynomial used, a parameter's significance surpassed a level chosen *a priori*. Using a significance level of 3 gave reasonable fits in most bins, but there were cases in which the polynomial level was clearly too low to fit the data even though the significance of individual terms was less than two σ . These bins typically had large χ^2 values for the fits.

To obtain reliable fits for all bins, the strategy was modified as follows. The mass distribution in each $\cos\theta^*$ bin was fit nine times, each with an increasing number of Chebyshev polynomials (starting from zeroth order, with the last fit using $T_n(x)$ up to $n = 8$) in the series. We looked for the best fit, determined by the place where the χ^2 of the fits stopped dropping by at least two units per additional term. In a few cases there was a second 'step' in χ^2 which met this criterion at larger N . In such cases we used the lower polynomial order as the best fit and assigned a background systematic to that particular bin as half the difference in yields between the two plateau levels. This systematic is added in quadrature with the statistical uncertainty of that bin. The maximum effect seen in any single bin was $1.0\sigma_{\text{stat}}$ in one case. Most bins had

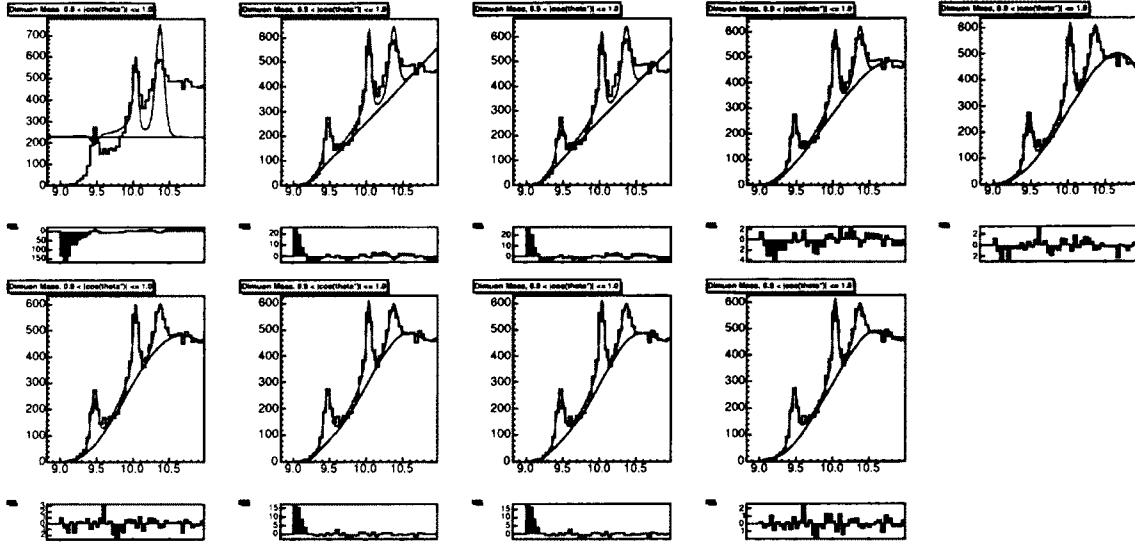


Figure 4.2: Mass fits for the $\Upsilon(1S)$, third p_T bin, tenth angular bin, using each Chebyshev Polynomial. The small plots under each histogram show the fit residuals $[(\text{function value} - \text{bin contents}) / \text{bin uncertainty}]$. This is a bin for which it may be difficult to choose the appropriate background shape, owing to its sparsely-populated lower bins and its curvature. In this case, the fifth-order polynomial was chosen based on the method described in Section [4.3.1](#)

negligible systematics, and for those that did, the systematic was usually less than $0.2\sigma_{stat}$. Signal PDFs were determined from Monte Carlo studies and adjusted to match angle-integrated mass plots, as described below.

The stability of the fit was also evaluated by fitting over a narrower mass range of $8.875 - 10.9 \text{ GeV}/c^2$. There is no sensitivity to the limits. The yields in some bins require a higher order Chebyshev polynomial because of clear curvature of the background. This is evident from Figure [4.2](#)

4.3.1 Υ Mass PDFs from Simulation

To determine the $\Upsilon(nS)$ yields from data, we fit fixed signal shapes and polynomial backgrounds to the mass distributions in each p_T and $|\cos \theta^*|$ bin. We obtain the sig-

nal shapes by fitting Monte Carlo events for each $\Upsilon(\text{nS})$ state after processing through CdfSim and Production. Efficiency effects are developed from data and triggers are emulated with cuts. The resulting mass distributions are binned into histograms and are fit by a smooth functional form.

We studied many different fitting functions and their combinations to fit the Υ mass distribution. The basic shapes are Gaussian (G), Johnson SU function (JSU), Crystal Ball (CB), or Modified Crystal Ball (MCB). Each of these functions is related to the Normal distribution, with the latter three capable of modeling an asymmetric distribution. This is important because of the radiative tail of the dimuon mass distributions from Bremsstrahlung, which is also modeled in the Monte Carlo. The functional forms used and the parameters involved are shown in the following equations.

$$PDF_G = \frac{1}{\sqrt{2\pi}\sigma^2} \exp\left(-\frac{(x-\mu)^2}{2\sigma^2}\right) \quad (4.1)$$

$$PDF_{JSU} = \frac{\delta}{\lambda\sqrt{2\pi}\sqrt{\left(\frac{x-\xi}{\lambda}\right)^2 + 1}} \exp\left(-1/2\left(\gamma + \delta \log\left(\left(\frac{x-\xi}{\lambda}\right) + \sqrt{\left(\frac{x-\xi}{\lambda}\right)^2 + 1}\right)\right)^2\right) \quad (4.2)$$

$$PDF_{CB} = \begin{cases} A \exp\left(-\frac{(x-Et)^2}{2\sigma^2}\right) & \frac{x-Et}{\sigma} > -\alpha \\ A\left(\frac{n}{\alpha}\right)^n \frac{\exp(-\alpha^2/2)}{\left(\frac{Et-x}{\sigma} + \frac{n}{\alpha} - \alpha\right)^n} & \frac{x-Et}{\sigma} \leq -\alpha \end{cases} \quad (4.3)$$

$$PDF_{MCB} = \begin{cases} A \left(\exp\left(-\frac{(x-Et)^2}{2\sigma^2}\right) + R \exp\left(-\frac{(x-Et)^2}{2(B\sigma)^2}\right) \right) & \frac{x-Et}{\sigma} > -\alpha \\ A\left(\frac{n}{\alpha}\right)^n \frac{\exp(-\alpha^2/2)}{\left(\frac{Et-x}{\sigma} + \frac{n}{\alpha} - \alpha\right)^n} & \frac{x-Et}{\sigma} \leq -\alpha \end{cases} \quad (4.4)$$

Single function shapes did not fit the peaks well, so we used combinations of functions: two and three Gaussians, JSU+G, JSU+2G, CB+G, JSU+CB. We chose JSU+CB as our fitting function, because among the candidate functions, it alone can fit all the data distributions successfully with no fit status errors from Minuit and with suitable χ^2 values. The other options all led to MINUIT fit errors, either an inaccurate error matrix or an error matrix that is not positive-definite. In all cases the JSU+CB function described the Monte Carlo distributions well.

4.3.2 Υ Mass Fits

Modifying the Monte Carlo Mass Fits

We know that the CDF simulation package does not match the data mass distributions exactly. In most CDF B Physics analyses, the Monte Carlo predictions track the relative p_T dependence of a mass distribution, but are typically too narrow and tend to be shifted slightly. The data themselves are used to correct the Monte Carlo PDF parameters, using the integral mass distribution. In this case, we divide the Υ data into $p_T(\Upsilon)$ bins appropriate for analyzing the nS state in question: 8 bins for the 1S, 4 bins for the 2S, 3S. We describe the data by three $\Upsilon(nS)$ peaks and a polynomial background term, just like the fits in the individual $|\cos \theta^*|$ bins. The mass PDFs use the Monte Carlo-derived PDF described above but include a single scale factor to float the CB Gaussian width (σ in Eq. 4.3) and the JSU width parameter (λ in Eq. 4.2) for all three states and a global mass shift term to allow movement in the central value for the peaks (E_t for the CBF, ξ for the JSU). The mass differences between the three nS peaks are fixed at the PDG values. This procedure determines the *width scale factor* $\text{sfw} = \text{width}(\text{data})/\text{width}(\text{Monte Carlo})$ and the *mass shift* for this p_T bin. These shifts are applied to the Monte Carlo mass PDFs in making the mass fits that determine the yields in a given $|\cos \theta^*|$ bin. An example of a mass fit in a single p_T bin, from which the shifts are determined, is shown in Fig. 4.3. The fit χ^2 values, mass shift and scale factors are summarized in Table 4.1

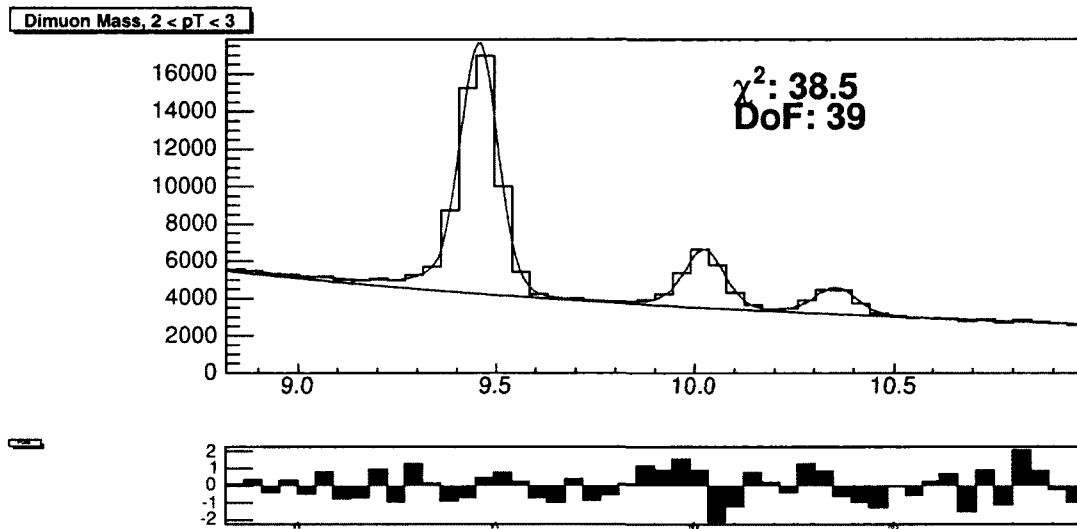


Figure 4.3: Mass fit in the first $\Upsilon(1S)$ p_T bin ($2\text{GeV}/c < p_T < 3\text{GeV}/c$), from which mass shifts and scale factors are extracted. Crystal Ball + Johnson SU functions are fit to each peak, and a third-order Chebyshev polynomial shape is applied to fit the background. The lower histogram shows the fit residuals [(function value - bin contents) / bin uncertainty].

Mass Shifts and Scale Factors			
$p_T(\Upsilon)[GeV/c]$	Fit χ^2 (39 DoF)	Mass shift $[GeV/c^2]$	Width SF
2-3	38.5	-0.0025 ± 0.0004	1.21 ± 0.01
3-4	44.0	-0.0027 ± 0.0004	1.19 ± 0.01
4-6	85.8	-0.0022 ± 0.0003	1.18 ± 0.01
6-8	60.5	-0.0027 ± 0.0004	1.17 ± 0.01
8-12	63.8	-0.0027 ± 0.0005	1.22 ± 0.01
12-16	49.9	-0.0027 ± 0.0008	1.18 ± 0.02
17-21	30.8	-0.0025 ± 0.0014	1.19 ± 0.03
21-40	45.7	0.0042 ± 0.0026	1.29 ± 0.06
Mean (2-21)		-0.0025	1.186

Table 4.1: Mass shifts and width scale factors from fits in p_T bins.

The mass shifts and scale factors in the 1S p_T bins in Table 4.1 excepting bin 8, are consistent with a single constant value at all p_T . The average mass shift and scale factor (over the first seven bins, weighted by bin population) is used for the subsequent yield fits for all nS states in all p_T bins.

The 21-40 GeV/c bin is somewhat inconsistent with other bins. Because we have no explanation for an upward shift in mass, we still apply the average mass shift and scale factor when fitting that bin. The actual values for the mass shift and scale factor from the fit are used to determine a systematic error in that bin's polarization, as discussed in the Systematics section, and its effect is small.

Angular Distributions and Yields

When the adjusted mass PDFs are fit to the data in a given p_T , $|\cos \theta^*|$ bin, the only free parameters are the three yield parameters and the background parameters for the Chebyshev terms, which are represented by the n 's in Equation 4.5. Since the

Chebyshev polynomials are defined on the interval from -1 to 1, the histograms and fit functions are transformed to that interval for the fit, and then transformed back to units of mass. The mass histograms (one for each $|\cos \theta^*|$ bin) used in the fit consist of 48 bins from 8.82 to 10.98 GeV/c². A maximum likelihood fit determines the yields, and the MINOS uncertainties on these parameters provide the yield uncertainties for the data in that particular bin. An exemplary set of ten of these fits from one p_T bin is shown in Figure 4.4. The fits all have acceptable χ^2 probabilities in the range of 2-96%. The yields are the inputs to the polarization fit, discussed in the next section. The order of the highest Chebyshev polynomial included in the base fit was determined by the procedure described in Section 4.3.

$$f(x) = n_{1S} \times PDF_{1S} + n_{2S} \times PDF_{2S} + n_{3S} \times PDF_{3S} + \sum_{i=1}^k n_k T_k(x) \quad (4.5)$$

Due to acceptance issues, a number of bins at large $\cos \theta^*$ have inadequate statistics to support a good fit. These histograms are still included in the mass fit figures, and can be identified by the absence of a drawn fit function. These bins are, of course, omitted from the polarization fit and their representative bins in the angular histogram are fixed to zero.

4.3.3 Υ Polarization Fitter

After the mass-fit procedure, we have the yields and their uncertainties for each $\Upsilon(\text{nS})$ state in each $|\cos \theta^*|$ bin i . A histogram representing the angular distribution of signal events is constructed from these values, taking the results of each fit to fill the individual bins. As noted previously, both bin contents and their uncertainties are gathered from the mass fits and included in the histograms.

After the angular distributions of the data have been determined, the transverse and longitudinal templates described in Chapter 3 can be compared to the data. The theoretical signal function for $|\cos \theta^*|$ bin i is the polarization-weighted sum of the

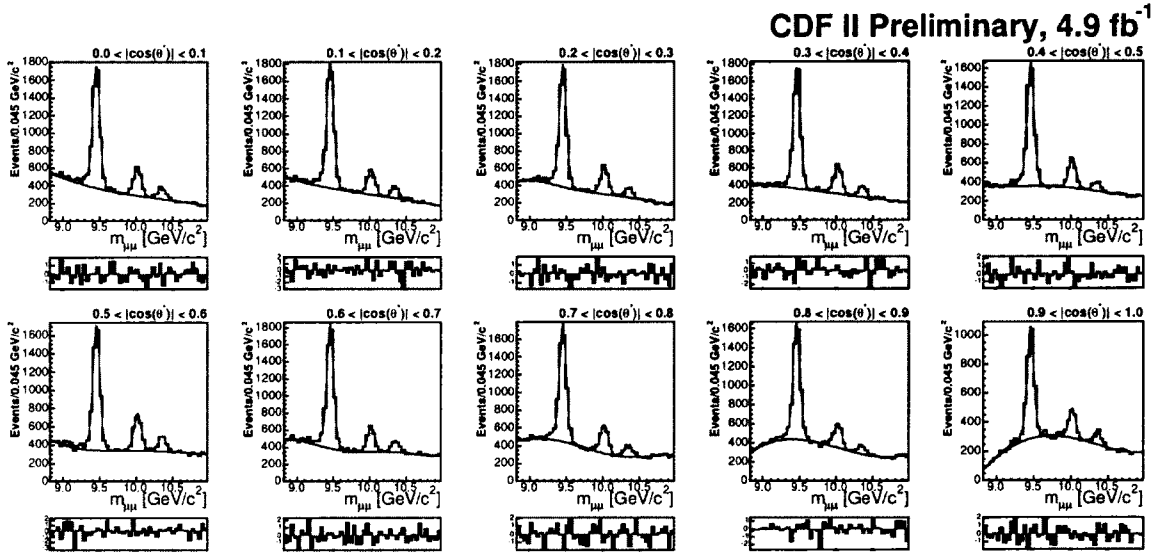


Figure 4.4: Mass fits in each $\cos \theta^*$ bin of the second $\Upsilon(1S)$ p_T bin ($3\text{GeV}/c < p_T < 4\text{GeV}/c$), from which signal distributions are extracted. Peak shapes are determined by Crystal Ball + Johnson SU functions fit to Monte Carlo, and background is modeled by a optimized Chebyshev polynomial.

$T(p_T)$ and $L(p_T)$ templates for that bin in this p_T range:

$$E_i(p_T) = N(\eta; p_T)[(1 - \eta) \cdot T_i(p_T) + \eta \cdot L_i(p_T)]. \quad (4.6)$$

The normalization parameter $N(\eta; p_T)$ matches the total yield $Y(p_T)$ for the specific p_T bin to the η -dependent prediction from the templates:

$$N(\eta; p_T) = \frac{Y(p_T)}{(1 - \eta) \cdot \sum_i T_i(p_T) + \eta \cdot \sum_i L_i(p_T)}. \quad (4.7)$$

The number of signal events $N_i(p_T)$ in bin i , the uncertainty $\sigma_i(p_T)$, each taken from the mass fits in $|\cos \theta^*|$ bins, and $E_i(p_T)$ define a χ^2 function which is optimized to determine the polarization parameter η . This function is implemented in ROOT using MINUIT. The best fit parameter and its uncertainty, evaluated using MINOS errors, are quoted in Tables [5.2](#), [5.3](#) and [5.4](#) for each Υ state and p_T bin.

4.3.4 Toy Monte Carlo Tests of Fitter

A study of possible bias in the fit function was done by making additional L and T Monte Carlo samples from which to build test samples with any desired polarization parameter η : a sample S having polarization η is $S(\eta) = \eta L + (1-\eta)T$. The size of the L and T samples *at generation* is equal. We chose sample sizes so that the number of events in the sample S after reconstruction and cuts was about 2000 events.

For simplicity, we chose to generate the test samples using only one run number. This had the unanticipated consequence of requiring an independent set of template files to be made with this same run number. The subtle variations in detector response with run number gave a misleading indication of a fitter pull when we used the standard templates. This points out the importance of using a proper luminosity-weighted set of runs for the actual templates used in the data analysis for optimal

Input η	Mean Pull	σ_{pull}
0.2	0.085 ± 0.047	0.944 ± 0.034
0.4	0.026 ± 0.053	1.047 ± 0.038
0.6	-0.022 ± 0.049	0.981 ± 0.035
0.8	0.027 ± 0.050	0.990 ± 0.036

Table 4.2: Pull distribution mean and σ for each input polarization in the fourth (6-8 GeV/c) p_T bin.

results. The size of the false pulls that we saw when we compared single-run-number samples to the complete templates was up to $0.5 \sigma_{statistical}$. We conclude that, having used the good run list for Monte Carlo and data, there is not likely to be any significant systematic uncertainty in polarization due to different acceptance between Monte Carlo templates and real data. The pulls are shown in Figure 4.5 and Table 4.2. We see no indication of a fitter bias.

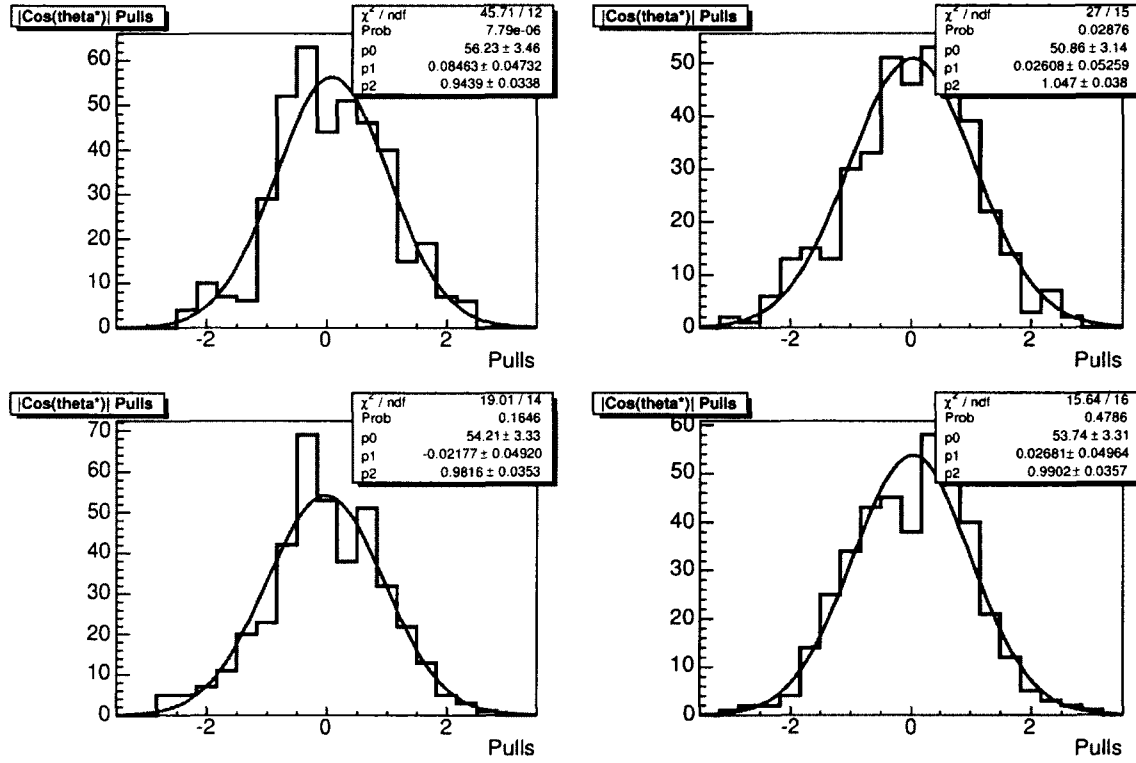


Figure 4.5: Pull distributions from polarization fitter for four trial values of η : 0.2 (top left), 0.4 (top right), 0.6 (bottom left), and 0.8 (bottom right).

Chapter 5

Results

5.1 $\Upsilon(\text{nS})$ Polarization Results

All of the necessary ingredients for the polarization analysis, including templates, signal distributions of $|\cos \theta^*|$, and a working fitter have been assembled. All that remains, then, is to combine them for a result, and investigate any possible systematic effects. This chapter addresses the findings of this analysis for all three Υ states.

5.2 Systematics

The polarization is determined by the muon angular distribution. Anything which affects the yield as a function of angle in the Υ rest frame can generate a systematic uncertainty. We consider the following potential sources of systematic error:

1. Change in the mass PDF as a function of $\cos \theta^*$
2. Incorrect estimation of mass PDF from Monte Carlo information
3. Change in acceptance as a function of $\cos \theta^*$ due to muon efficiency function
4. Sensitivity to $p_T(\Upsilon)$ re-weighting function

5. Sensitivity to $\cos \theta^*$ bin width and resolution
6. Sensitivity to background parametrization
7. Change in templates due to unaccounted-for changes in apparatus performance during data-taking.
8. Averaging mass shifts and scale factors
9. Acceptance issues related to transverse momentum thresholds

The first item might arise because the muon momenta are nearly equal when $\cos \theta^* \sim 0$ and are quite asymmetric when $\cos \theta^* \sim \pm 1$. Multiple Coulomb scattering will be different in the two cases. Such effects are included in the Monte Carlo. Example mass fits to data shown in Fig. [B.9](#) in $\cos \theta^*$ bins, using Monte Carlo parametrizations, show no indication of a discrepancy within our statistical precision. Therefore, we assign no systematic uncertainty from this source.

For the second possible issue, as discussed in the section on Mass PDFs from Simulation, many studies of particle masses confirm that the Monte Carlo underestimates the actual width of the mass distribution for a particle peak, although it gets the p_T variation of the width correct. The studies outlined in that section showed excellent fits to the observed mass distribution integrated over all decay angles. We studied the effect of changing the histogram bin widths used for the Monte Carlo samples from the standard 10 MeV up to 30 MeV. No significant change in the integrated yields in data occurred when we used different Monte Carlo parametrizations. We assign no systematic uncertainty from this source.

Item three includes the effects of systematic uncertainties in the muon efficiency function, which translate into systematic uncertainties in the templates. We have looked at the effect on the Υ polarization of changing the muon efficiency function by $\pm 1\sigma_{\text{syst}}$. The largest change seen in Υ polarization parameter η in any bin was approximately 0.0006. This, being around 1% of the statistical uncertainty, is negligible as a source of systematic uncertainty.

We have also used a different p_T reweighting scheme than the one described above, wherein weights are assigned to Monte Carlo based strictly upon the data p_T distribution. The changes to polarization are negligible. We assign no systematic uncertainty due to p_T re-weighting shape.

In checking our resolution for $\cos \theta^*$, we determined that the polarization varies within statistical uncertainty when halving or doubling the bin width. Combining this with the result that our resolution is much smaller than the bin width used indicates that there should be no systematic uncertainty assigned due to angular bin migration effects.

In an earlier version of this analysis, polarization results were measured using a method which utilized sideband subtraction to determine the $\Upsilon(1S)$ yields and polarization, as in the CDF Run I measurement. The method described here constitutes a completely different approach. The polarization results from the two studies are consistent with the statistical changes in the data arising from differing methods and datasets. This indicates that there are no large systematics from the background subtraction. For this method, we have varied the width of the mass window from the standard 8.82-10.98 GeV/c² to 9.00-10.8 GeV/c². There was no effect on the signal yields.

The variation of yield due to different orders of the background polynomial is a systematic uncertainty that varies bin by bin. In many bins there is no effect. As discussed in Section 4.1, we determine the systematic uncertainty in each $\cos \theta^*$ bin due to the fit choice. The systematic uncertainty is added in quadrature with the statistical uncertainty before making the polarization fit. To illustrate the procedure, we include two examples. The first is a bin to which we assign zero systematic. The second is a bin to which we assign the largest systematic seen in this sample. These are the seventh and sixth angle bins of the first $\Upsilon(1S)$ p_T bin, for which the mass fits are seen in Fig. [B.9](#). The data are in Table [5.1](#).

Order	Yield	σ_{stat}	χ^2/dof	Order	Yield	σ_{stat}	χ^2/dof
0	3794	81	408.0	0	4335	86	300.8
1	3544	81	115.8	1	4100	86	63.4
2	3611	82	80.8	2	4115	87	61.5
3	3736	86	48.5	3	4186	91	53.6
4	3743	87	48.3	4	4213	92	48.5
5	3744	88	48.3	5	4225	93	48.2
6	3782	93	46.5	6	4288	95	43.4
7	3775	93	45.6	7	4288	99	43.4
8	3737	85	44.1	8	4305	104	43.2

Table 5.1: Mass Yields, Uncertainties and χ^2 values versus Chebyshev order for $Y(1S)$ p_T bin 1, angle bins 7 (left) and 6 (right). The left side shows a rapid decrease of χ^2 with background order until $N=3$, then plateaus. No systematic is assigned. The right side shows a steady decrease until $N = 4$, then another step down at $N=6$. The two yields differ by 75 events. We use half that number as the systematic.

The variation of templates with run number was explored as part of the fitter bias study. Using probe samples made with a single run number to test templates made with the complete good run list showed potential biases of up to $0.5 \sigma_{statistical}$. This bias varies depending on the run number used and disappears when the template run distribution matches the probe run distribution. Because the templates were built using the good run list that describes the data luminosity distribution, any residual effect of run-dependent variations will be negligible.

As noted above, the mass shift and scale factor determined for the highest $\Upsilon(1S)p_T$ bin was inconsistent with the other bins. As we are unaware of any reason to expect an upward mass shift, we apply the weighted average of these values over the first seven bins to this bin. Using that as a baseline, we also conduct the analysis using the exact values determined for that bin. We find that the χ^2 of the mass fits in angular

bins is stable between the two versions, and the resulting change in polarization (η) is 0.021. We assign half of this value as a systematic in that bin. No systematic is assigned to the 2S and 3S bins in this region because the highest p_T range for those states covers 12-40 GeV/c . This range begins well below the start of the $\Upsilon(1S)$ bin in question, and it is populated primarily by events in the lower end of the p_T range. Therefore, the scale factor and mass shift for these states is better-described by the preceding $Upsilon(1S)p_T$ bins.

Lastly, varying the minimum muon p_T allowed by the trigger cuts has some effect on the polarization result. This became evident when the analysis was performed on a sample where both muons were required to have CMU and CMP stubs, therefore requiring 4 GeV/c -muons. To track down the discrepancy, the minimum p_T of both muons for the CMU-CMUP dataset was varied from 3-4.3 GeV/c (the minimum p_T of 4 GeV/c for the CMUP muon was still in effect). A slight shift toward transverse polarization was seen, varying in magnitude up to $\sigma_\eta = 0.013$ in with different cuts. As such, a systematic uncertainty of 0.013 is assigned to account for this effect. This is approximately equal to the statistical error at low- p_T , but is insignificant in the higher p_T bins.

$\Upsilon(1S)$ Polarization

The results of the $\Upsilon(1S)$ fits listed in Table 5.2 show a small longitudinal polarization independent of $p_T(\Upsilon)$, consistent with the CDF Run I result [16]. At the two highest p_T bins, the central values are slightly positive, but with significant uncertainties. The results are consistent with a constant polarization $\alpha = -0.111 \pm 0.019$ with $\chi^2 = 5.0$ for seven degrees of freedom. There is no clear trend toward transverse polarization in the s-channel helicity frame. The $\cos\theta^*$ distributions for 1S data and the results of these fits are included in Figure 5.1

This measurement does agree with the Run I result, as demonstrated in Figure 5.7. The agreement is quite good above p_T of 10 GeV/c . Below this, the old results

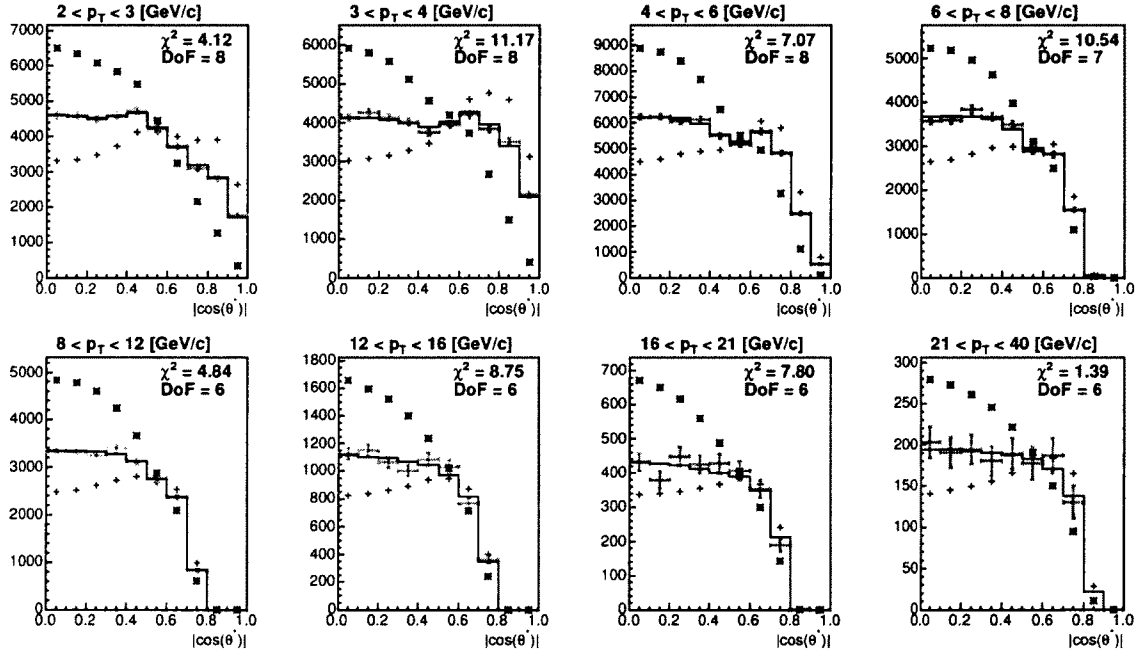


Figure 5.1: Polarization fits for $\Upsilon(1S)$, in each of the eight p_T bins. The data is shown in green with error bars. T and L templates are shown in red and blue points, respectively, while the best fit combination of the templates is indicated by the black histogram.

$\Upsilon(1S)$ Polarization					
$p_T(\Upsilon)[\text{GeV}/c]$	Data Yield	Mean p_T [GeV/c]	η	α	$\sigma_{\text{syst}}(\eta)$
2-3	38940 ± 291	2.51	0.403 ± 0.013	$-0.148^{+0.026}_{-0.026}$	0.013
3-4	37911 ± 281	3.49	0.383 ± 0.012	$-0.108^{+0.026}_{-0.025}$	0.013
4-6	48567 ± 308	4.88	0.385 ± 0.013	$-0.113^{+0.027}_{-0.026}$	0.013
6-8	25238 ± 216	6.90	0.395 ± 0.023	$-0.133^{+0.047}_{-0.046}$	0.013
8-12	22504 ± 200	9.62	0.363 ± 0.026	$-0.065^{+0.056}_{-0.054}$	0.013
12-16	7492 ± 121	13.68	0.350 ± 0.043	$-0.037^{+0.097}_{-0.091}$	0.013
16-21	3083 ± 81	18.03	0.280 ± 0.061	$0.126^{+0.156}_{-0.142}$	0.013
21-40	1510 ± 59	25.32	0.385 ± 0.104	$-0.112^{+0.234}_{-0.201}$	0.017

Table 5.2: Measured yields and polarization parameters for $\Upsilon(1S)$

show slightly more-transverse characteristics. The Run I analysis was based on a modified sideband-subtraction to isolate signal events. The offset could be attributed to mis-estimation of background proportions in that study, because the background of the $\Upsilon(nS)$ peaks shows a strong transverse polarization.

$\Upsilon(2S)$ and $\Upsilon(3S)$ Polarization

The $\Upsilon(2S)$ and $\Upsilon(3S)$ data are grouped into coarser p_T bins, as discussed earlier. These states are less strongly contaminated by feed-down from χ_b states because the production cross sections for the higher-mass χ_b states are small at the Tevatron. These polarizations are viewed as a better test of the NRQCD predictions. The polarization starts out somewhat negative at small p_T and moves positive at the largest p_T . The data are not consistent with a p_T -independent polarization. The $\cos\theta^*$ distributions for 2S data and the results of these fits are included in Figure [5.2](#) and tabulated in Table [5.3](#)

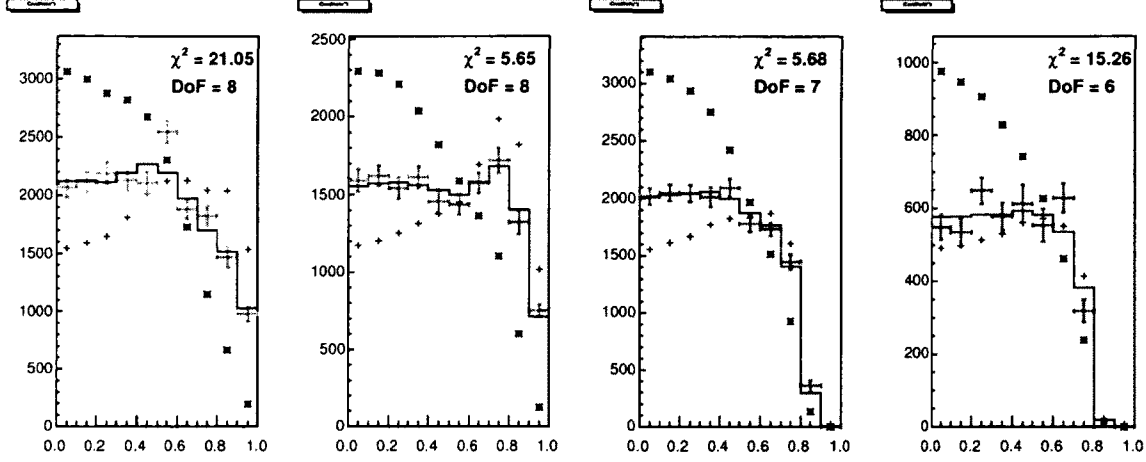


Figure 5.2: Polarization fits for $\Upsilon(2S)$, in each of the four p_T bins. The data is shown in green with error bars. T and L templates are shown in red and blue points, respectively, while the best fit combination of the templates is indicated by the black histogram.

$\Upsilon(2S)$ Polarization					
$p_T(\Upsilon)[\text{GeV}/c]$	Data Yield	Mean p_T [GeV/c]	η	α	σ_{syst}
2-4	19397 ± 270	2.97	0.381 ± 0.025	$-0.103^{+0.053}_{-0.052}$	0.013
4-6	14997 ± 222	4.85	0.342 ± 0.024	$-0.018^{+0.054}_{-0.052}$	0.013
6-12	16167 ± 211	8.14	0.292 ± 0.032	$0.095^{+0.078}_{-0.075}$	0.013
12-40	4155 ± 102	16.87	0.179 ± 0.059	$0.394^{+0.177}_{-0.161}$	0.013

Table 5.3: Measured yields and polarization parameters for $\Upsilon(2S)$

$\Upsilon(3S)$ Polarization					
$p_T(\Upsilon)[\text{GeV}/c]$	Data Yield	Mean p_T [GeV/c]	η	α	σ_{syst}
2-4	9923 ± 280	2.96	0.322 ± 0.050	$0.025^{+0.119}_{-0.111}$	0.013
4-6	8187 ± 230	4.88	0.305 ± 0.042	$0.066^{+0.101}_{-0.095}$	0.013
6-12	10063 ± 221	8.16	0.340 ± 0.051	$-0.016^{+0.118}_{-0.109}$	0.013
12-40	3099 ± 110	16.97	0.181 ± 0.084	$0.387^{+0.258}_{-0.224}$	0.013

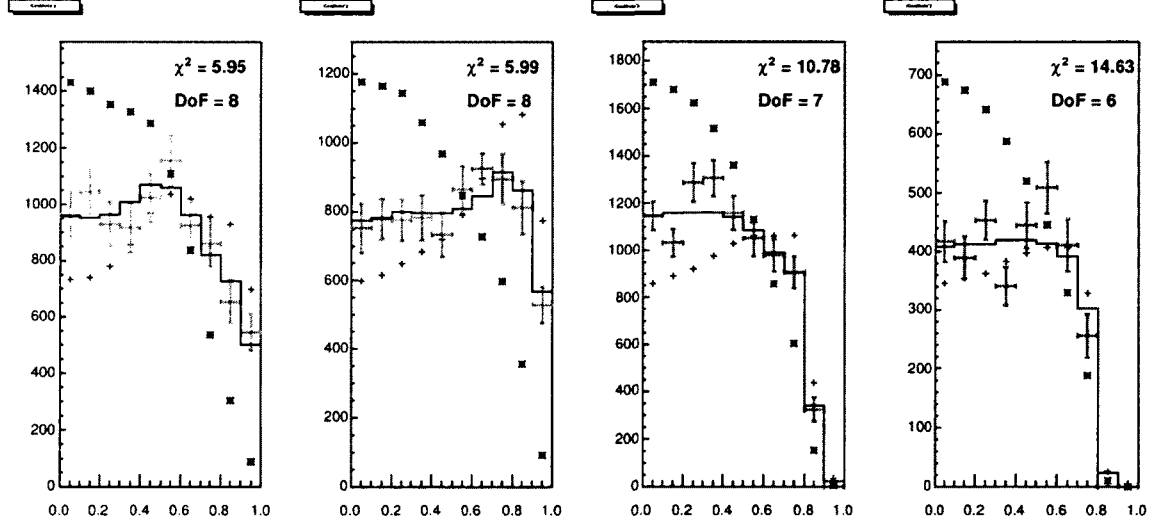
Table 5.4: Measured yields and polarization parameters for $\Upsilon(3S)$ 

Figure 5.3: Polarization fits for $\Upsilon(3S)$, in each of the four p_T bins. The data is shown in green with error bars. T and L templates are shown in red and blue points, respectively, while the best fit combination of the templates is indicated by the black histogram.

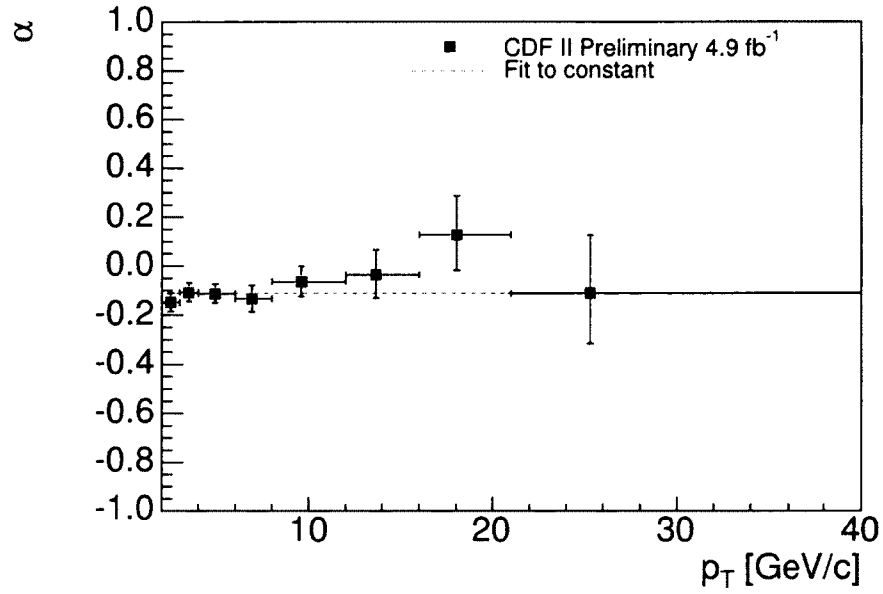


Figure 5.4: $\Upsilon(1S)$ polarization results, with a fit to a constant. The best fit is $\alpha = -0.111 \pm 0.019$.

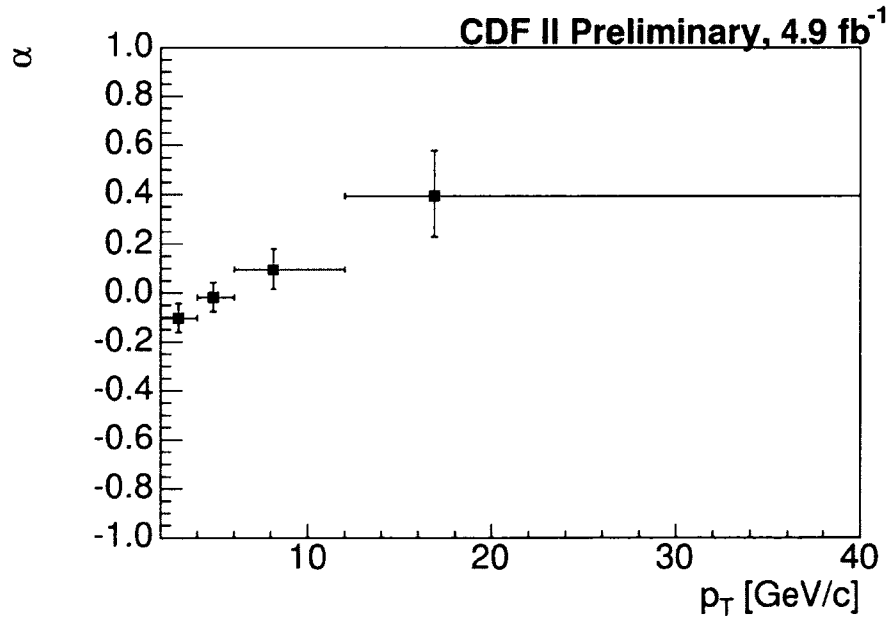
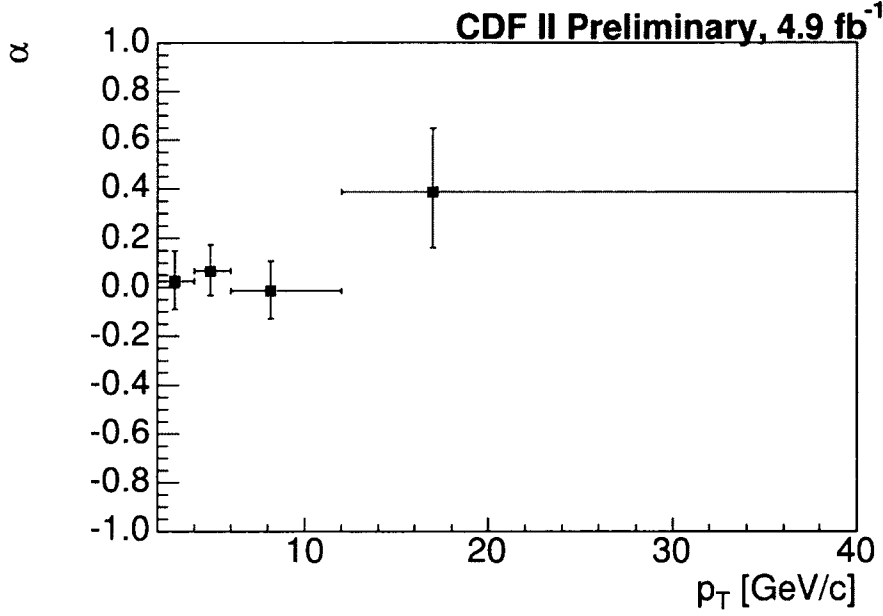


Figure 5.5: $\Upsilon(2S)$ polarization results.

Figure 5.6: $\Upsilon(3S)$ polarization results.

5.3 Comparison with Other Measurements

The results of the polarization measurements using 4.9 fb^{-1} for the $\Upsilon(1S)$, $\Upsilon(2S)$, and $\Upsilon(3S)$ are illustrated in Figures [5.4](#), [5.5](#) and [5.6](#) respectively.

Our result for $\Upsilon(1S)$ polarization agrees well with the CDF Run I result [\[16\]](#), as shown in Figure [5.7](#). The agreement is quite good above $p_T = 10 \text{ GeV}/c$. Below this region, the new result shows a slight offset in the longitudinal direction from the Run I values. Because the measurement in Run I relied on a modified sideband subtraction to isolate signal events, it may be more sensitive to strongly-polarized background. The $\Upsilon(nS)$ background shows very strong transverse characteristics. Even so, the offset is decidedly small. The Run I result was for $|y| < 0.4$, while the NRQCD predictions were explicitly done to compare to that result, using the same y range.

The method applied in the Run I measurement can also be applied to the full dataset from this analysis, to highlight the effects of choosing a different means of signal extraction. The two methods again have very good agreement above $10 \text{ GeV}/c$

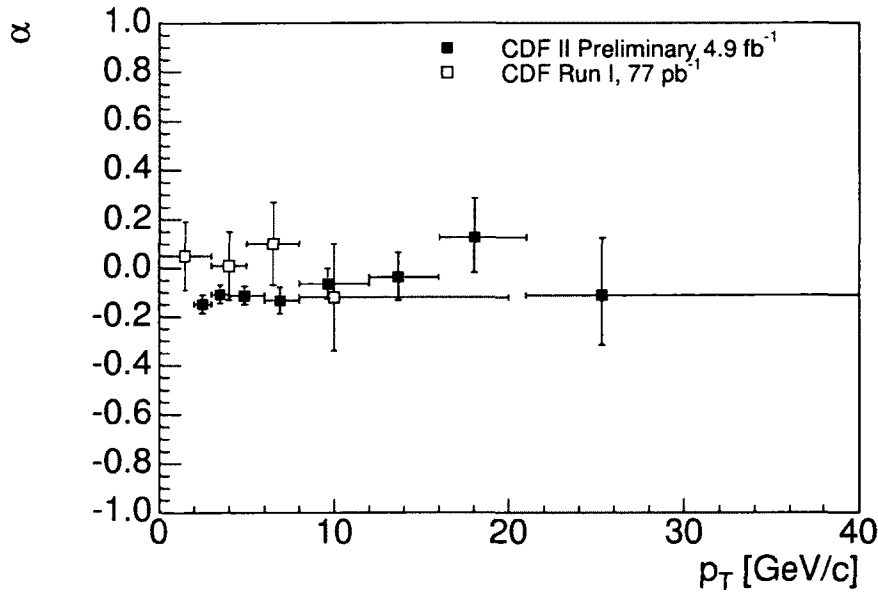


Figure 5.7: $\Upsilon(1S)$ polarization results are consistent within errors with the CDF Run I measurement.

and the low- p_T effects are still apparent. The comparison is shown in Figure 5.8

The $\Upsilon(1S)$ polarization measurement by D0 disagrees with the CDF results both for Run I and Run II. They report longitudinal polarization at low p_T and a trend toward transverse polarization at high p_T as indicated in Figure 5.9 [17]. On the other hand the result presented here is consistent with the D0 result for the $\Upsilon(2S)$ polarization, shown in Figure 5.10. The D0 measurements cover the range $|y| < 1.8$, while these measurements use data in the range $|y| < 0.6$. The difference in rapidity coverage is inadequate to explain the $\Upsilon(1S)$ discrepancy, which is still not understood.

There have heretofore been no measurements of $\Upsilon(3S)$ polarization for comparison. It is remarkable that the $\Upsilon(2S)$ and $\Upsilon(3S)$ results show such similar polarizations in this measurement.

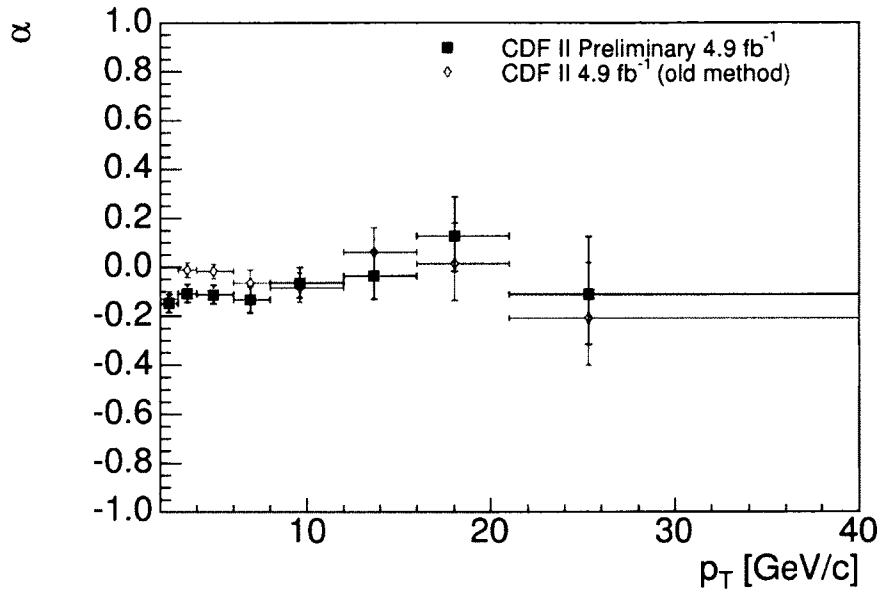


Figure 5.8: $\Upsilon(1S)$ polarization results using 4.9 fb^{-1} illustrating the results of the method from CDF Run I against the current method using the same data.

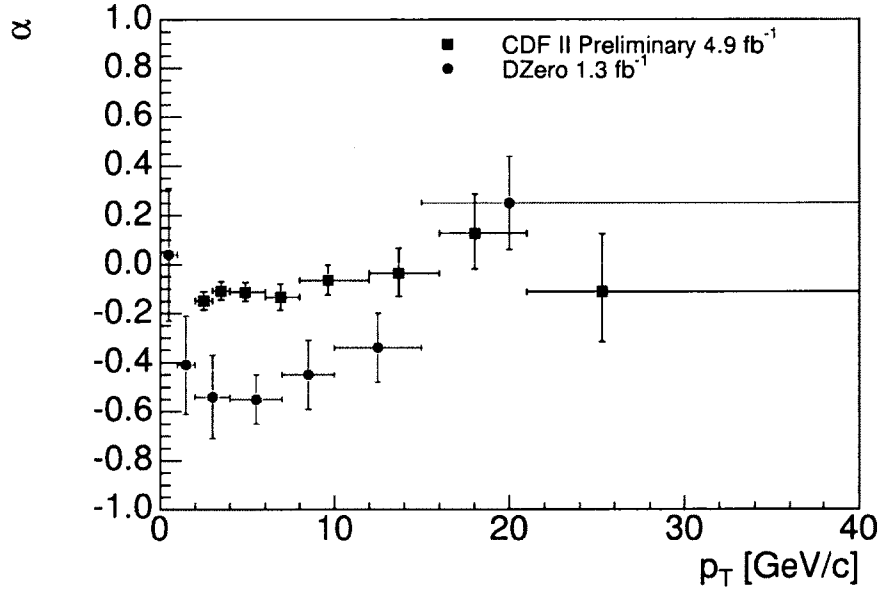


Figure 5.9: $\Upsilon(1S)$ polarization results stand in contrast to DZero measurements at low p_T , and become somewhat more consistent with increasing p_T .

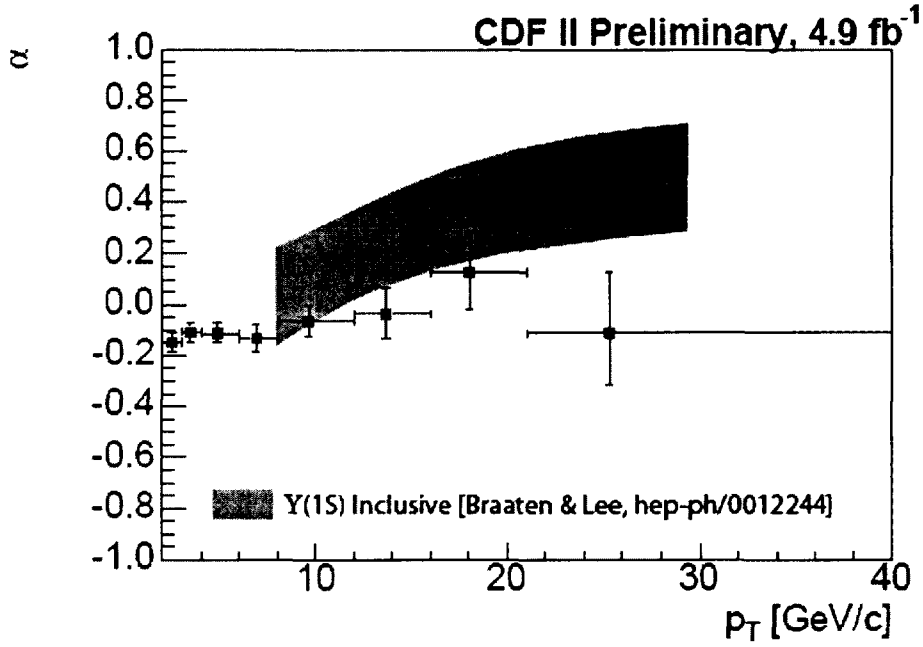


Figure 5.10: $\Upsilon(1S)$ polarization results with NRQCD predictions (green band). Excepting the highest- p_T bin, the measurement is consistent within error with the theoretical prediction.

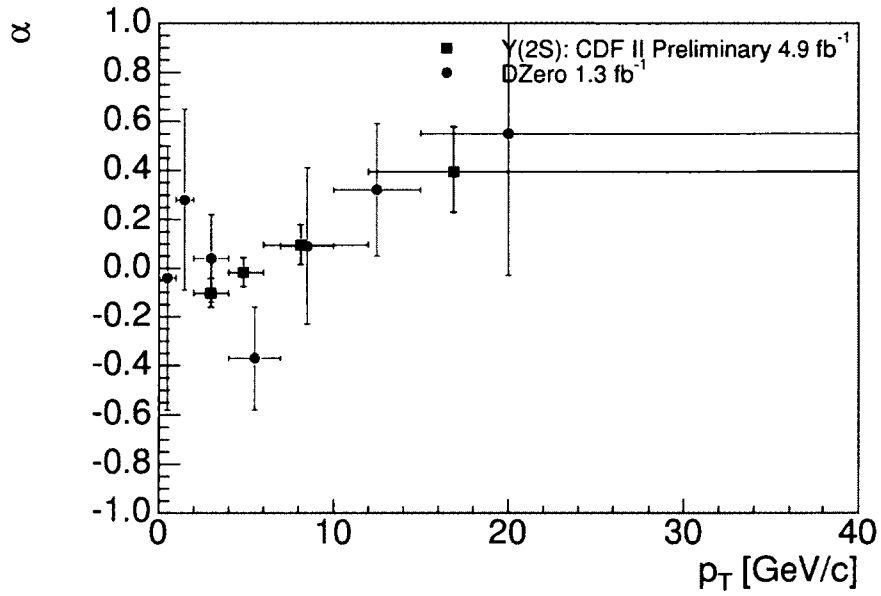


Figure 5.11: $\Upsilon(2S)$ polarization results are consistent with the DZero measurement.

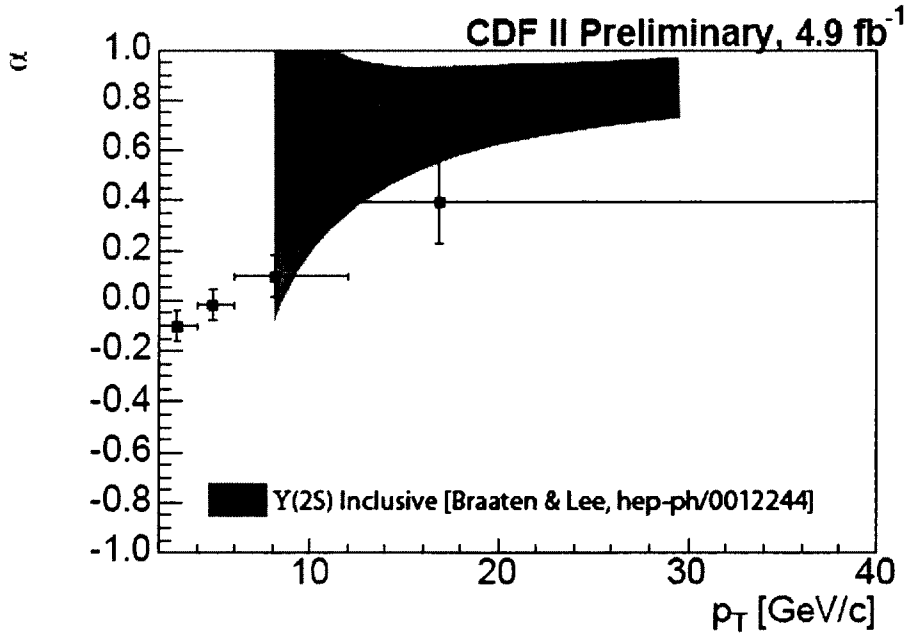


Figure 5.12: $\Upsilon(2S)$ polarization results with NRQCD predictions (green band). Theory and measurement are consistent within error.

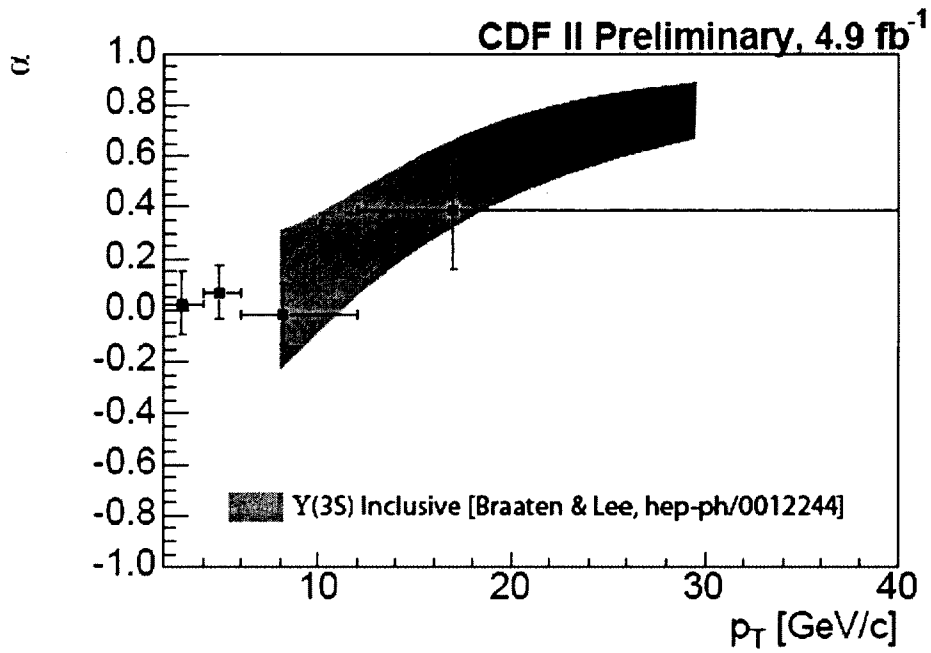


Figure 5.13: $\Upsilon(3S)$ polarization results with NRQCD predictions (green band). The measurement agrees well with the prediction.

Chapter 6

Conclusions

6.1 Summary

This measurement of $\Upsilon(1S)$ polarization shows very small polarization at all p_T in the s-channel helicity frame. A fit to a constant polarization gives $\langle \alpha \rangle = -0.108 \pm 0.014$ with a χ^2 of 5.2 for 7 degrees of freedom. This result is consistent with the CDF Run I measurement but disagrees at low p_T with the published D0 measurement. Our background measurements show significant variation with dimuon mass, whereas the D0 fits use smooth polynomial background estimates over a large mass interval. The respective rapidity coverage of each measurement also differs, with D0 covering $|y| < 1.8$ and this measurement covering $|y| < 0.6$. The results presented here disagree with the NRQCD prediction of transverse polarization for large p_T .

The gluon tower model of Ref. [14] predicts a longitudinal polarization and expects that it will be significantly longitudinal by $15 \text{ GeV}/c$. The multiple-interaction model of Ref. [15] also predicts longitudinal polarization, but starting at $p_T \sim 5 \text{ GeV}/c$, lower than we observe. This model incorporates multi-gluon processes, suggesting that the Υ states should have accompanying gluon jet activity.

Recent work by Lansberg and collaborators on the higher order effects in the color single model suggest that the $\Upsilon(1S)$ polarization may become longitudinal as p_T in-

creases. This model is capable of handling both the cross section and the polarization of the Υ family and deserves careful study [11].

The 2S and 3S states are expected in NRQCD to be more strongly transverse than the 1S, due to reduced feed-down from higher mass χ_b and nS states. We observe larger polarizations for these states at the highest p_T . For $p_T < 10$ GeV/c the 2S and 3S states are essentially unpolarized. In this p_T region polarization effects due to feed-down from higher nS states to the 1S should be small, leaving only χ_b feed-down to affect the 1S polarization.

These results extend Υ polarization measurements to a transverse mass $m_T \leq 4m_\Upsilon$, fully into the perturbative regime. They do not follow the NRQCD expectations in the s-channel helicity frame.

6.2 Current and Future Efforts

While this analysis expands the CDF polarization to a much higher- p_T range, many questions remain about discrepant results from other analyses and theoretical predictions. Recently, it has been suggested that the use of a single spin quantization axis is inadequate, not only because it is difficult to compare disparate measurements, but also because it does not make full use of information from the events [30]. It is thought that performing a measurement with multiple quantization axes on the same dataset will provide a good indication of the size of unaccounted-for systematic effects.

The analysis framework applied here is applicable in any frame. One simply generates new Monte Carlo simulations of events fully polarized along the new quantization axis, computes the polarization angle, and repeats the procedure described in the preceding chapters. The analysis is currently being re-done, using the framework provided here, in the Collins-Soper frame. In that frame, the quantization axis is along the incoming proton direction.

Furthermore, it has been suggested that it is possible to unambiguously determine the polarization by performing the analysis in 3 dimensions without choosing a specific quantization axis [30]. Then, the result can be projected onto a given axis, or analyzed in its entirety. This method is much more sensitive to inhomogeneity in detector acceptance and response, and also requires a very robust statistical sample. Studies are currently being undertaken at CDF to ascertain the feasibility of performing this analysis on the CDF dataset.

Bibliography

- [1] B. Povh, *Particles and nuclei: an introduction to the physical concepts* Physics and Astronomy Online Library (Springer, 2004). [9](#)
- [2] Particle Data Group, K. Nakamura *et al.*, J. Phys. G. **37**, 075021 (2010). [10](#)
- [3] R. Baier and R. Ruckl, *Hadronic collisions: A quarkonium factory*, Z. Phys. C. **19**, 251 (1983). [9](#)
- [4] T. C. Collaboration, J/psi,psi(2s) to mu+ mu- and b to j/psi,psi(2s) cross sections, 1994, arXiv:hep-ex/9412013. [10](#)
- [5] M. Kramer, *Quarkonium Production at High-Energy Colliders*, Prog. Part. Nucl. Phys **47**, 141 (2001), hep-ph/0106120v1. [11](#)
- [6] CDF Collaboration, F. Abe *et al.*, *J/ψ and ψ(2S) Production in pp̄ collisions at √s = 1.8TeV*, Phys. Rev. Lett. **79**, 572 (1997). [11](#)
- [7] CDF Collaboration, D. Acosta *et al.*, *Measurement of the J/ψ Meson and b-Hadron Production Cross Sections in p̄p Collisions at √s = 1960 GeV*, Phys. Rev. D **71**, 032001 (2005). [11](#)
- [8] CDF Collaboration, T. Affolder *et al.*, *Measurement of J/ψ and ψ(2S) Polarization in p̄p collisions at √s = 1.8 TeV*, Phys. Rev. Lett. **85**, 2886 (2000). [11](#)

- [9] CDF Collaboration, A. Abulencia *et al.*, *Polarization of J/ψ and $\psi(2S)$ Mesons Produced in $p\bar{p}$ Collisions at $\sqrt{s}=1.8\text{TeV}$* , Phys. Rev. Lett. **99**, 132001 (2007). [111](#)
- [10] Z. Collaboration, Measurement of j/ψ helicity distributions in inelastic photo-production at hermes, JHEP 0912:007,2009, 2009, arXiv:0906.1424. [111](#)
- [11] J. P. Lansberg, Total j/ψ and ψ production cross section at the LHC: theory vs. experiment, 2010, arXiv:1012.2815. [111](#) [89](#)
- [12] S. Fleming *et al.*, *Power Counting and Effective Field Theory for Charmonium*, Phys. Rev. D **64**, 036002 (2001). [111](#)
- [13] E. Braaten and J. Lee, *Polarization of $\Upsilon(nS)$ at the Tevatron*, Phys. Rev. D **63**, 071501 (2000). [111](#)
- [14] V. Khoze *et al.*, *Inelastic J/ψ and Υ hadroproduction*, Eur. Phys. J. **39**, 163 (2005). [112](#) [88](#)
- [15] P. Artoisenet *et al.*, *Υ production at the Tevatron and the LHC*, Phys. Rev. Lett. **101**, 152001 (2008), arXiv:0806.3282. [112](#) [88](#)
- [16] CDF Collaboration, D. Acosta *et al.*, *Υ Production and Polarization in $p\bar{p}$ Collisions at $\sqrt{s}=1.8\text{TeV}$* , Phys. Rev. Lett. **88**, 161802 (2002). [114](#) [76](#) [82](#)
- [17] DZero Collaboration, V. Abazov *et al.*, *Measurement of the Polarization of the $\Upsilon(1S)$ and $\Upsilon(2S)$ States in $p\bar{p}$ Collisions at $\sqrt{s}=1.96\text{ TeV}$* , Phys. Rev. Lett. **101**, 182004 (2008). [114](#) [83](#)
- [18] F. Abe *et al.*, Fermilab Report No. FERMILAB-Pub-96/390-E, 1996 (unpublished). [121](#)
- [19] T. Akimoto *et al.*, *The CDF Run IIb Silicon Detector: Design, preproduction, and performance*, Nucl. Instr. Meth. **556**, 459 (2006). [122](#)

- [20] A. Affolder *et al.*, *Intermediate silicon layers detector for the CDF experiment*, Nucl. Instr. Meth. **453**, 84 (2000). [\[22\]](#)
- [21] D. Ambrose, *The Central Outer Tracker for Run II at CDF*, Nucl. Instr. Meth. **518**, 117 (2004). [\[24\]](#)
- [22] L. Balka *et al.*, *The CDF central electromagnetic calorimeter*, Nucl. Instr. Meth. **267**, 272 (1988). [\[26\]](#)
- [23] S. Bertolucci *et al.*, *The CDF central and endwall hadron calorimeter*, Nucl. Instr. Meth. **267**, 301 (1988). [\[27\]](#)
- [24] A. Bhatti *et al.*, *The CDF level 2 calorimetric trigger upgrade*, Nucl. Instrum. Meth. **598**, 331 (2009). [\[28\]](#)
- [25] S. Amerio, *CDF trigger final balance: Offline resolution at low level selections to fight against Tevatron increasing luminosity*, Nucl. Instrum. Meth. **617**, 250 (2010). [\[32\]](#)
- [26] A. Abulencia *et al.*, *eXtremely Fast Tracker trigger upgrade at CDF*, Nucl. Instrum. Meth. **598**, 328 (2009). [\[34\]](#)
- [27] D. Glenzinski *et al.*, *Measurement of Level-1, 2, and 3 Low- p_T DiMuon Trigger Efficiencies for the $B_s^0 \rightarrow \mu^+ \mu^-$ Analysis*, CDF Note 7314, 2005. [\[37\]](#)
- [28] Geant3 detector design and simulation tool, CERN Program Library Wong Writeup W5013, 1993. [\[38\]](#)
- [29] J. Heinrich, personal communication, 2011. [\[61\]](#)
- [30] P. Faccioli, C. Lourenço, and J. a. Seixas, *New approach to quarkonium polarization studies*, Phys. Rev. D **81**, 111502 (2010). [\[89\]](#) [\[90\]](#)
- [31] S. U. Chung, *Spin formalisms*, BNL-QGS-02-0900, 2007. [\[95\]](#)

Appendices

Appendix A

Angular Distribution Derivation

The decay angular distribution for a resonance can be derived as follows [31]. The production and decay of the resonance (in the case below, the Υ) is denoted by

$$a + b \rightarrow c + \Upsilon; \quad \Upsilon \rightarrow 1 + 2. \quad (\text{A.1})$$

The transition amplitude \mathcal{M}_{fi} is given by

$$\mathcal{M}_{fi} \sim \sum_{\Lambda} \langle \vec{p} \lambda_1 \lambda_2 | \mathcal{M} | \Upsilon \Lambda \rangle \langle \vec{p}_f \lambda_c \Lambda | T(w_0) | \vec{p}_i \lambda_a \lambda_b \rangle. \quad (\text{A.2})$$

Here, λ_1 , λ_2 , λ_a , λ_b , and λ_c are the respective spins of particles 1, 2, a , b , and c , \vec{p} represents the momentum of particle 1 in the Υ rest frame with spherical angles denoted by $\Omega = (\theta, \phi)$, \mathcal{M} is the transition amplitude for the Υ decay, \vec{p}_f is the center-of-mass momentum of particle c , Λ denotes the helicity of the Υ , w is used to denote the effective mass of the Υ decay products 1 and 2, and \vec{p}_i is the momentum of particle a . T is an operator defined by $S = 1 + iT$, where S is the invariant S matrix.

The differential cross section in the decay angle $\Omega = (\theta, \phi)$ is then written as

$$\frac{d\sigma}{d\Omega} \sim \int d\Omega_0 dw K(w) \sum |\mathcal{M}_{fi}|^2, \quad (\text{A.3})$$

where $K(w)$ includes all dependencies on w , including the phase space factor and the square of the Breit-Wigner function $D(w)$ of the Υ .

Defining the spin density matrix $\rho_{\Lambda\Lambda'}^J$ of the Υ as

$$\rho_{\Lambda\Lambda'}^J \sim \int d\Omega_0 \sum_{\lambda_a, \lambda_b, \lambda_c} \langle \vec{p}_f \lambda_c \Lambda | T(w_0) | \vec{p}_i \lambda_a \lambda_b \rangle \times \langle \vec{p}_f \lambda_c \Lambda | T(w_0) | \vec{p}_i \lambda_a \lambda_b \rangle^*, \quad (\text{A.4})$$

the differential cross-section can be written as

$$\frac{d\sigma}{d\Omega} \sim \int dw K(w) \sum_{\Lambda\Lambda'\lambda_1\lambda_2} \langle \vec{p} \lambda_1 \lambda_2 | \mathcal{M} | \Upsilon \Lambda \rangle \rho_{\Lambda\Lambda'}^J \langle \Upsilon \Lambda' | \mathcal{M}^\dagger | \vec{p} \lambda_1 \lambda_2 \rangle. \quad (\text{A.5})$$

Exploiting parity conservation and Eq. [A.4](#) we have

$$\rho_{\Lambda\Lambda'}^J = (-)^{\Lambda-\Lambda'} \rho_{-\Lambda-\Lambda'}^J. \quad (\text{A.6})$$

Here, ρ_{00} is the longitudinal polarization fraction (denoted as η in this thesis), and $(\rho_{11} + \rho_{-1-1})$ is the transverse fraction.

The quantization axis for this analysis, as described in Chapter [II](#) lies along the Υ direction in the lab frame. As such, the coordinate system of the decay is defined so that \hat{Z} points in the direction of the Υ , \hat{y} is normal to the production plane and along the cross product of the incoming proton direction and \hat{z} , and $\hat{x} = \hat{y} \times \hat{z}$.

The normalized angular distribution for the $\Upsilon(\text{nS})$ decay to two muons is then

$$I(\Omega^*) = \left(\frac{2J+1}{4\pi} \right) \sum_{mm'} \rho_{mm'}^J \sum_{\lambda} D_{m\lambda}^{J*}(\phi^*, \theta^*, 0) D_{m'\lambda}^J(\phi^*, \theta^*, 0) g_{\lambda}^J, \quad (\text{A.7})$$

where $\Omega^*(\theta^*, \phi^*)$ is the μ^+ direction in the Υ rest frame, as measured from the lab-frame Υ momentum vector, J is the Υ spin, $\rho_{mm'}^J$ is the Υ spin density matrix, g_{λ}^J is the decay amplitude, $\lambda = \lambda_{\mu^+} - \lambda_{\mu^-}$, and $D_{m'\lambda}^J(\phi^*, \theta^*, 0)$ is a rotation matrix defined as

$$\begin{aligned} D_{m'm}^j(\alpha, \beta, \gamma) &= \langle jm' | e^{-i\alpha J_z} e^{-i\beta J_y} e^{-i\gamma J_z} | jm \rangle \\ &= e^{-im'\alpha} d_{m'm}^j(\beta) e^{-im\gamma}. \end{aligned} \quad (\text{A.8})$$

These rotations can be related to the spherical harmonics $Y_m^l(\theta, \phi)$ via

$$D_{m'0}^{l*}(\phi, \theta, 0) = \sqrt{\frac{4\pi}{2l+1}} Y_m^l(\theta, \phi). \quad (\text{A.9})$$

Assuming that the muons from the decay are relativistic in the Υ rest frame, it is inferred that the μ^+ and μ^- are fully right- and left-handed. This means that $\lambda = 1$ and therefore $g_\lambda^J = g_1^1 = 1$ because $\sum g_\lambda^J = 1$.

The spin density matrix can be simplified as well. Considering Equation [A.6](#) and the hermiticity of the matrix, it follows that $\rho_{-1-1} = \rho_{11}$, $\rho_{-11} = \rho_{1-1}$, $\rho_{-10} = -\rho_{10}$, $\rho_{0-1} = -\rho_{01}$. Thus, the matrix contains only four independent parameters, *e.g.*, ρ_{00} , ρ_{1-1} , $\text{Re}(\rho_{10})$, and $\text{Im}(\rho_{10})$.

Applying each of these features to Equation [A.7](#) and inserting the appropriate spherical harmonics according to Equation [A.9](#) the angular distribution becomes

$$\begin{aligned} I(\Omega^*) = \left(\frac{3}{4\pi}\right) & \left[\frac{1}{4}(1 + \cos^2\theta^*) + \frac{\rho_{00}}{4}(2\sin^2\theta^* - \cos^2\theta^* - 1) + \frac{\rho_{1-1}}{2}\sin^2\theta^*\cos 2\phi^* \right. \\ & \left. + \frac{\text{Re}(\rho_{10})}{\sqrt{2}}\sin 2\theta^*\cos\phi^* - \sqrt{2}\text{Im}(\rho_{10})\sin\theta^*\sin\phi^* \right]. \end{aligned} \quad (\text{A.10})$$

The angular distributions used in this analysis have been integrated over ϕ^* . To find the appropriate distribution, Equation [A.10](#) is integrated over ϕ^* , giving

$$I(\theta^*) = \frac{3}{2} \left[\frac{1}{4}(1 + \cos^2\theta^*) + \frac{\rho_{00}}{4}(1 - 3\cos^2\theta^*) \right]. \quad (\text{A.11})$$

Then, the distribution is simplified by defining a polarization parameter α .

$$\alpha = \frac{1 - 3\rho_{00}}{1 + \rho_{00}} \quad (\text{A.12})$$

Inserting the new polarization parameter into Equation [A.11](#) it becomes

$$I(\theta^*) = \frac{3}{2(\alpha + 3)}(1 + \alpha\cos^2\theta^*). \quad (\text{A.13})$$

Appendix B

Mass Fit Plots

B.1 Mass Fits in p_T Bins

To determine corrections to the peak width and mean of Monte Carlo mass peak shapes which are applied to data in each angular bin, mass shifts and scale factors are extracted from fits to the mass distributions in each p_T bin, allowing those two parameters to float. Crystal Ball + Johnson SU functions from Monte Carlo are fit to each peak, and a third-order Chebyshev polynomial shape is applied to fit the background.

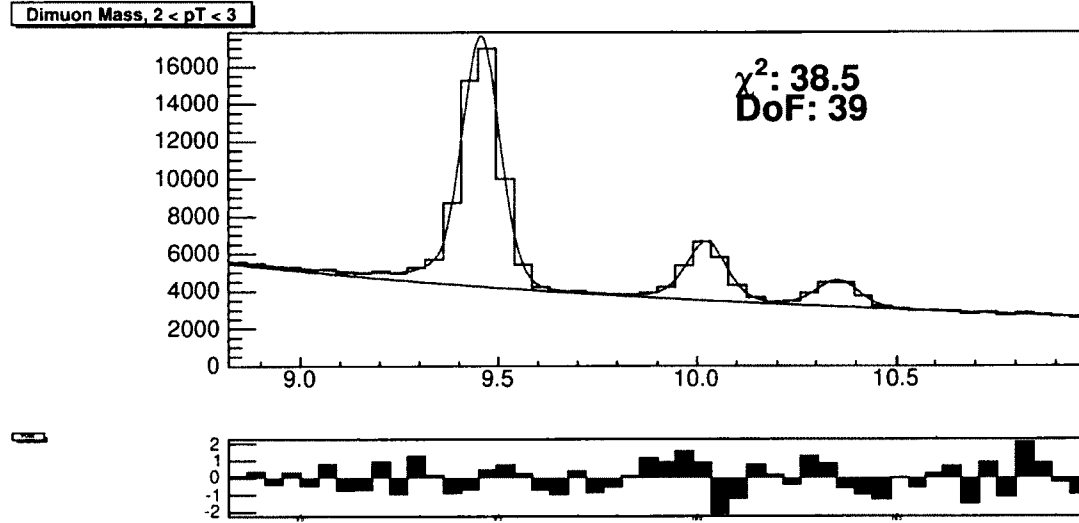


Figure B.1: Mass fit in the first $\Upsilon(1S)$ p_T bin ($2 \text{ GeV}/c < p_T < 3 \text{ GeV}/c$).

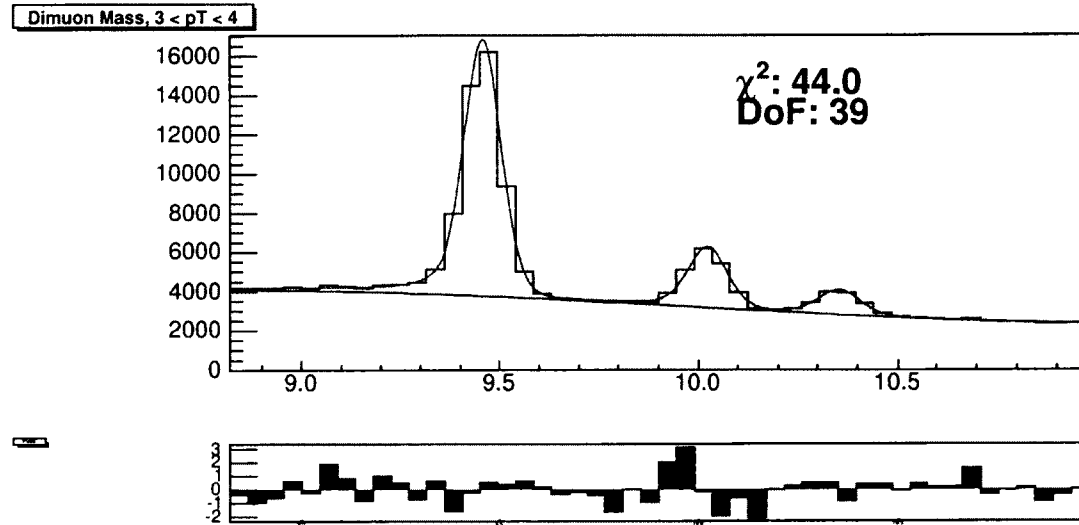


Figure B.2: Mass fit in the second $\Upsilon(1S)$ p_T bin ($3 \text{ GeV}/c < p_T < 4 \text{ GeV}/c$).

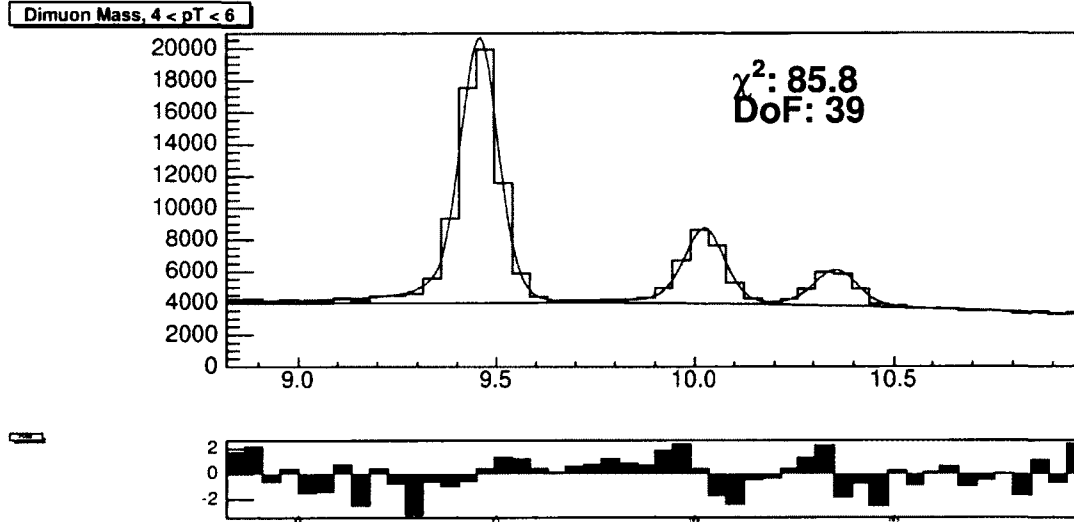


Figure B.3: Mass fit in the third $\Upsilon(1S)$ p_T bin ($4 GeV/c < p_T < 6 GeV/c$).

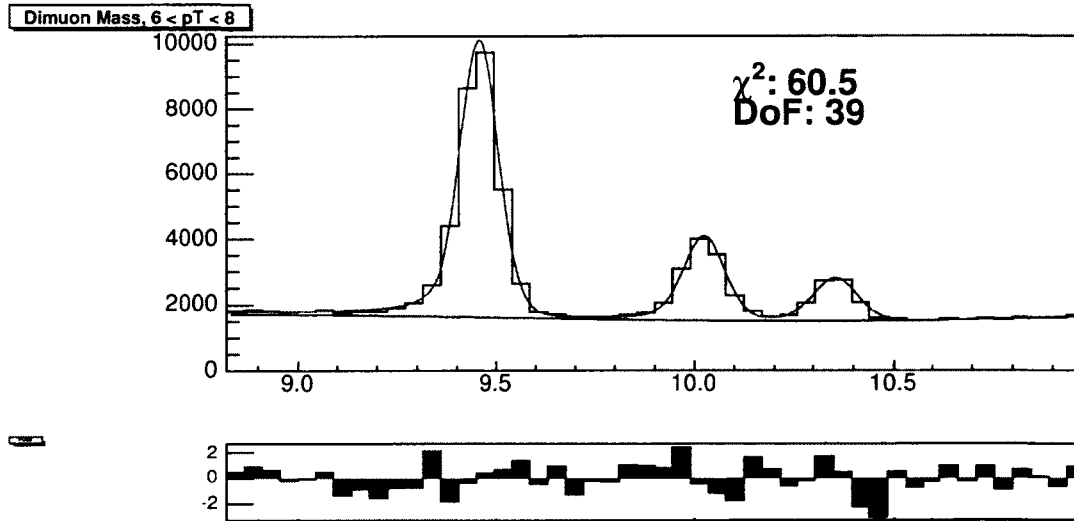


Figure B.4: Mass fit in the fourth $\Upsilon(1S)$ p_T bin ($6 GeV/c < p_T < 8 GeV/c$).

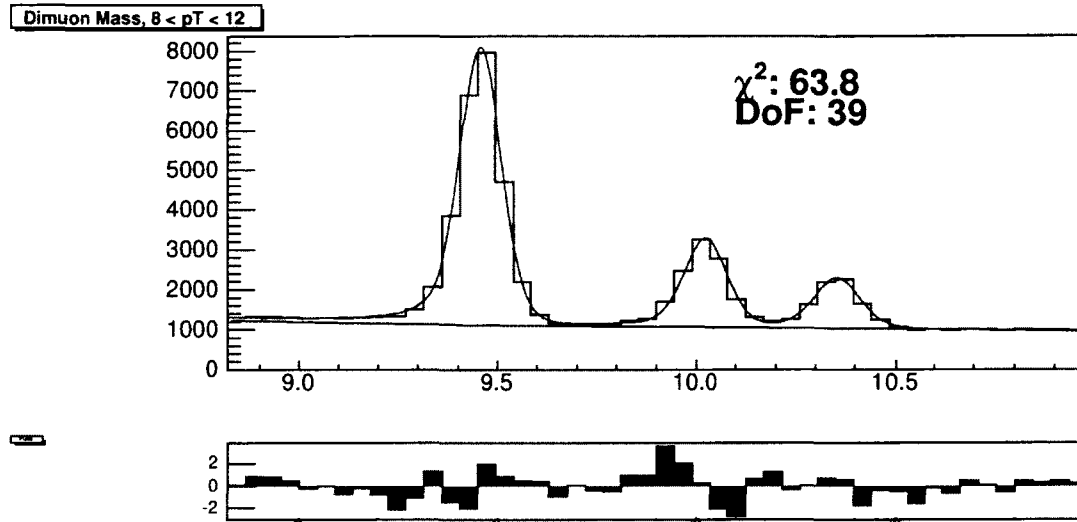


Figure B.5: Mass fit in the fifth $\Upsilon(1S)$ p_T bin ($8 \text{ GeV}/c < p_T < 12 \text{ GeV}/c$).

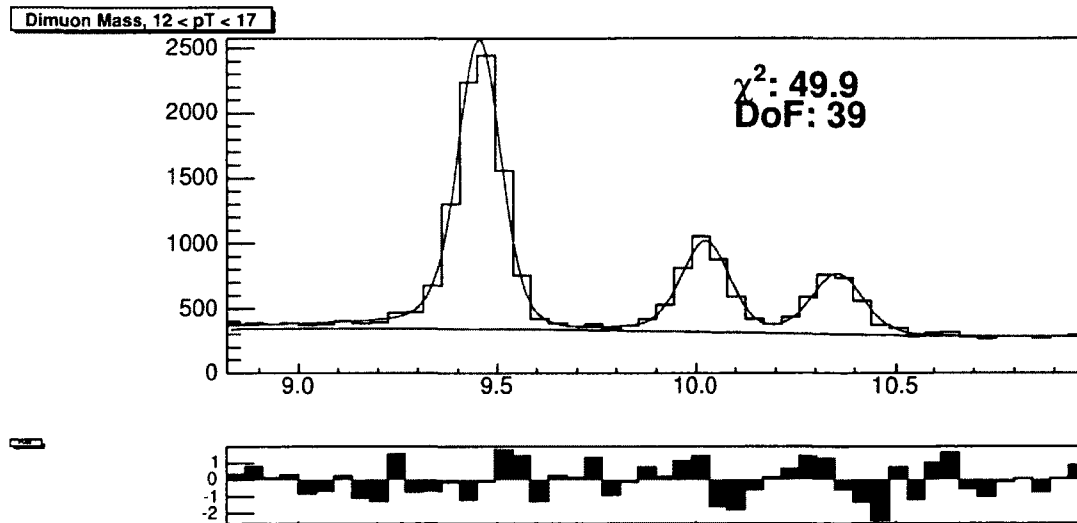


Figure B.6: Mass fit in the sixth $\Upsilon(1S)$ p_T bin ($12 \text{ GeV}/c < p_T < 16 \text{ GeV}/c$).

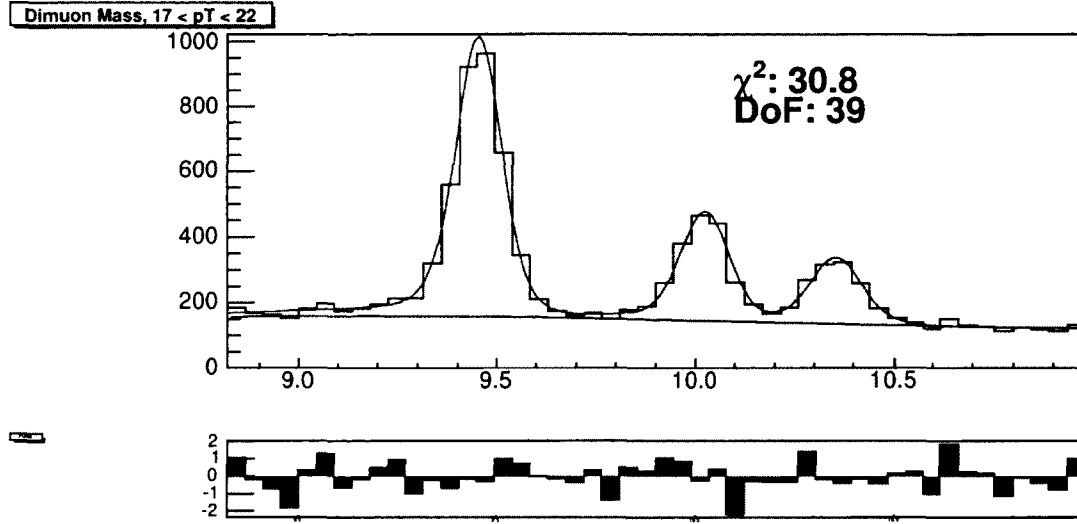


Figure B.7: Mass fit in the seventh $\Upsilon(1S)$ p_T bin ($16\text{GeV}/c < p_T < 21\text{GeV}/c$).

B.2 Mass Fits in Angular Bins

To obtain the bin contents for the angular distributions used in the polarization fitter, mass fits are performed in angular bins as described in Section [4.3.2](#)

All mass fits used for determining angular bin contents are shown below. In each fit, peak shapes are determined by Crystal Ball + Johnson SU functions fit to Monte Carlo, and background is modeled by series of Chebyshev polynomials.

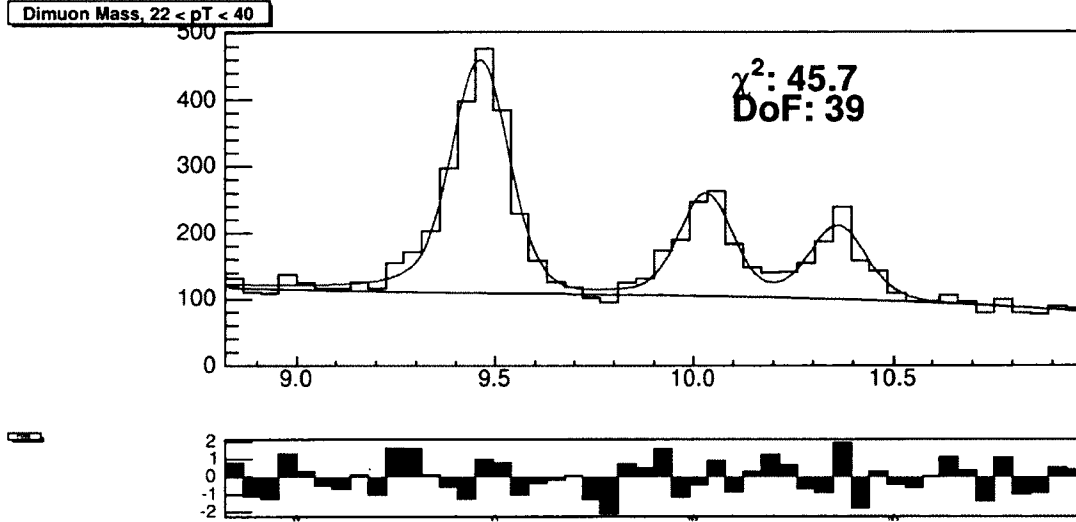


Figure B.8: Mass fit in the eighth $\Upsilon(1S)$ p_T bin ($21\text{GeV}/c < p_T < 40\text{GeV}/c$).

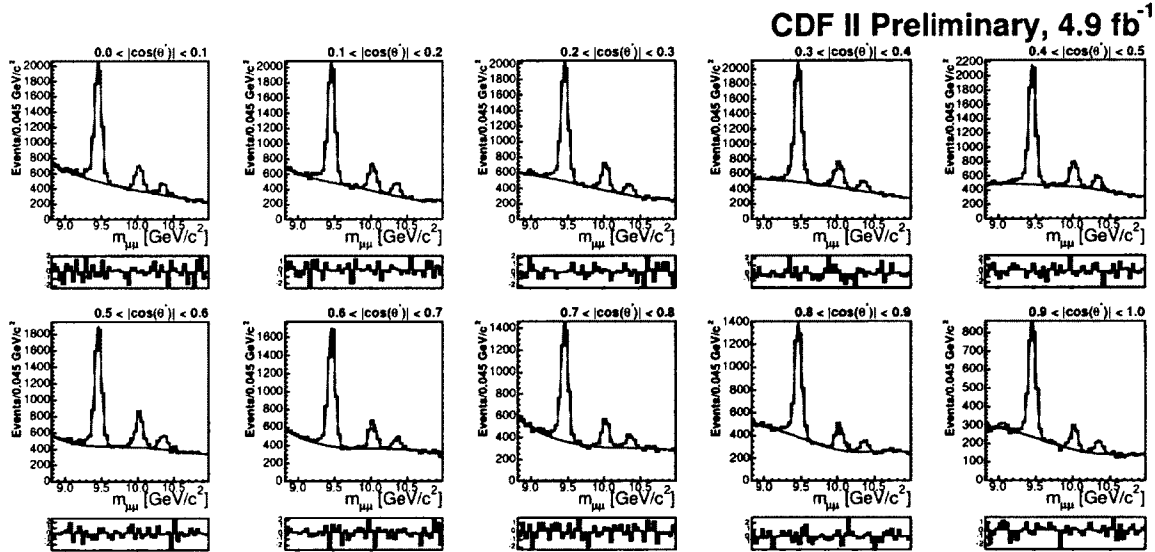


Figure B.9: Mass fits in each $\cos \theta^*$ bin of the first $\Upsilon(1S)$ p_T bin ($2\text{GeV}/c < p_T < 3\text{GeV}/c$).

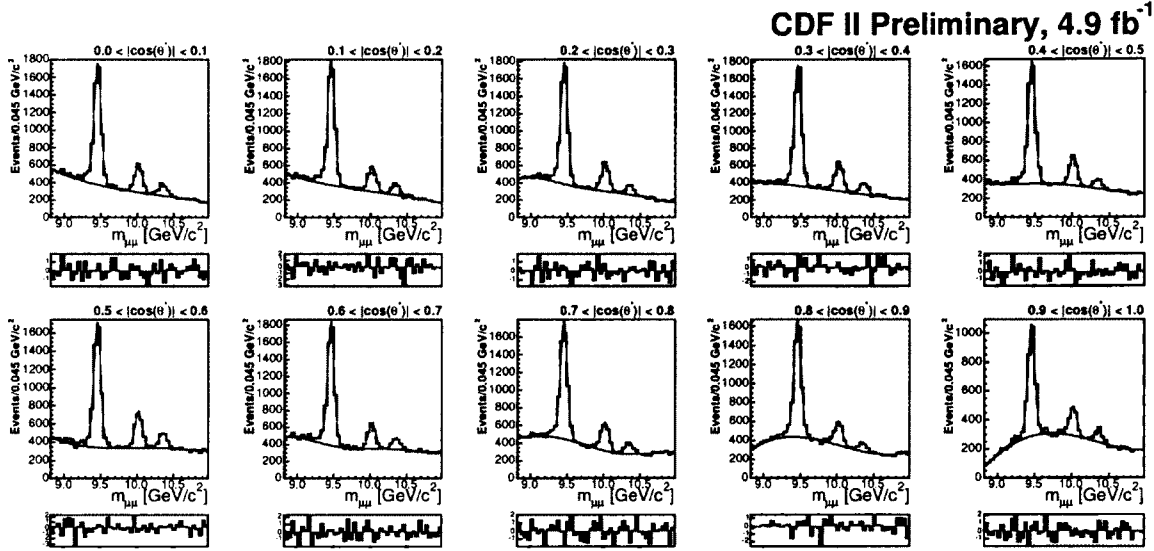


Figure B.10: Mass fits in each $\cos \theta^*$ bin of the second $\Upsilon(1S)$ p_T bin ($3\text{GeV}/c < p_T < 4\text{GeV}/c$).

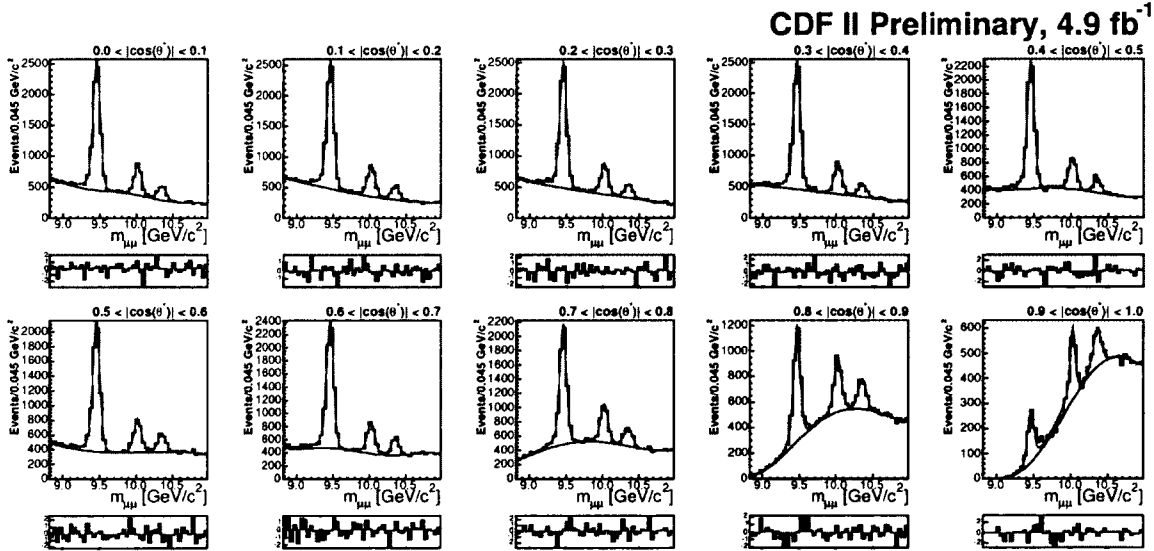


Figure B.11: Mass fits in each $\cos \theta^*$ bin of the third $\Upsilon(1S)$ p_T bin ($4\text{GeV}/c < p_T < 6\text{GeV}/c$).

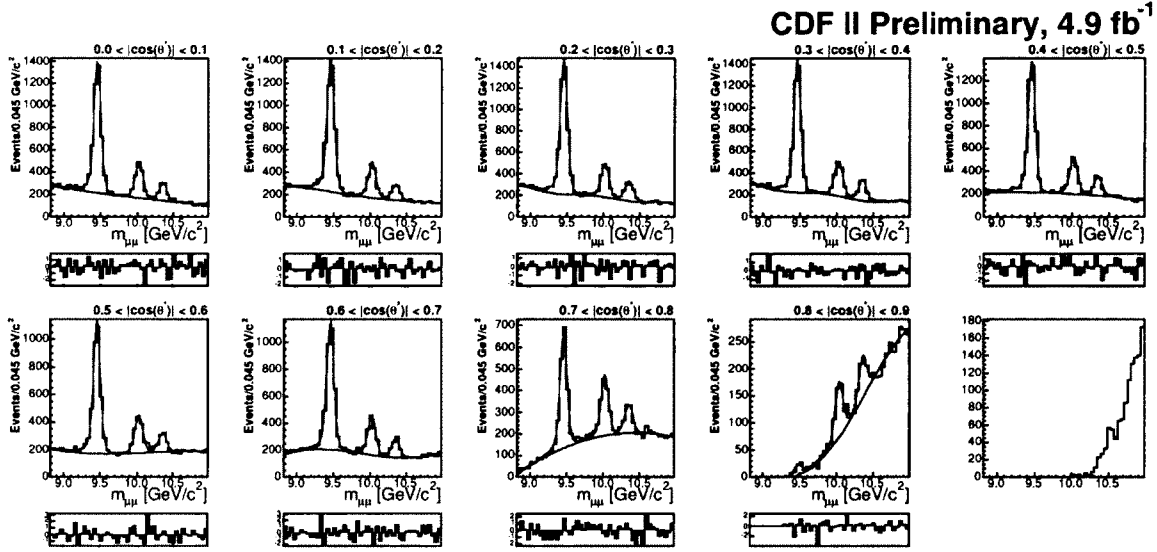


Figure B.12: Mass fits in each $\cos \theta^*$ bin of the fourth $\Upsilon(1S)$ p_T bin ($6\text{GeV}/c < p_T < 8\text{GeV}/c$).

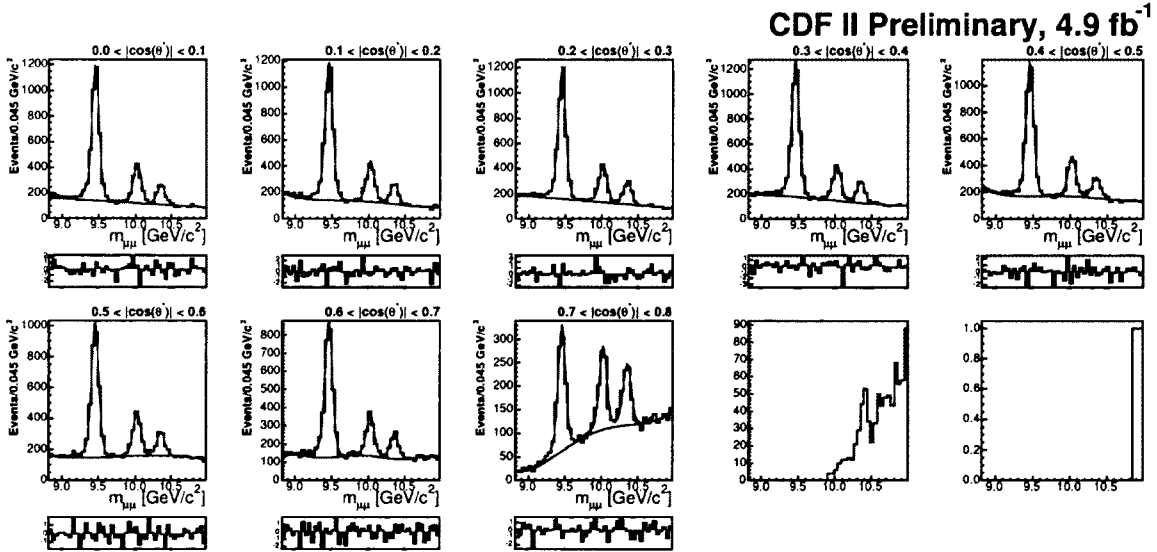


Figure B.13: Mass fits in each $\cos \theta^*$ bin of the fifth $\Upsilon(1S)$ p_T bin ($8\text{GeV}/c < p_T < 12\text{GeV}/c$).

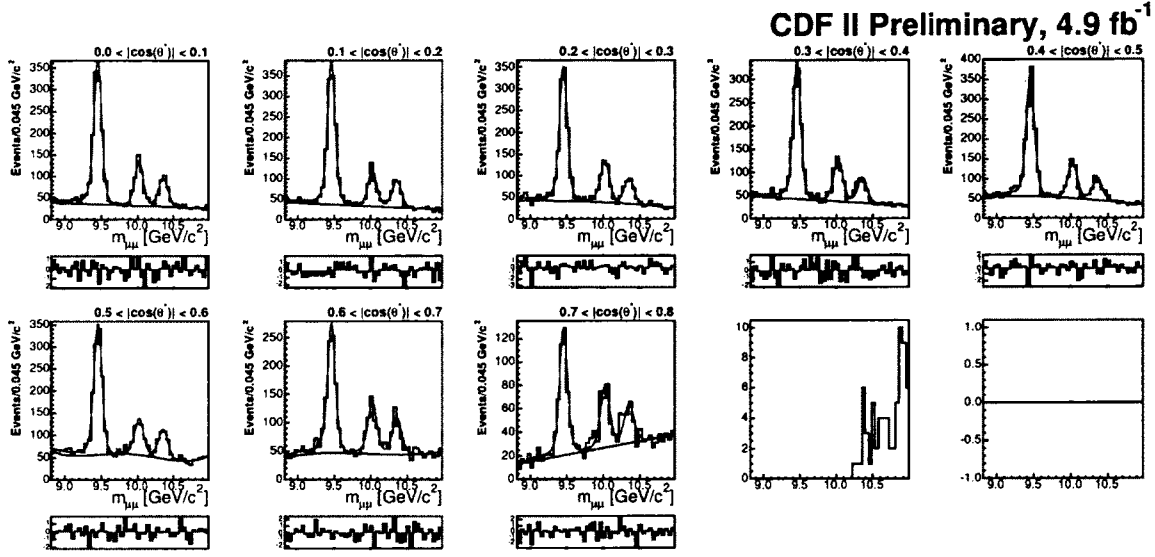


Figure B.14: Mass fits in each $\cos \theta^*$ bin of the sixth $\Upsilon(1S)$ p_T bin ($12\text{GeV}/c < p_T < 16\text{GeV}/c$).

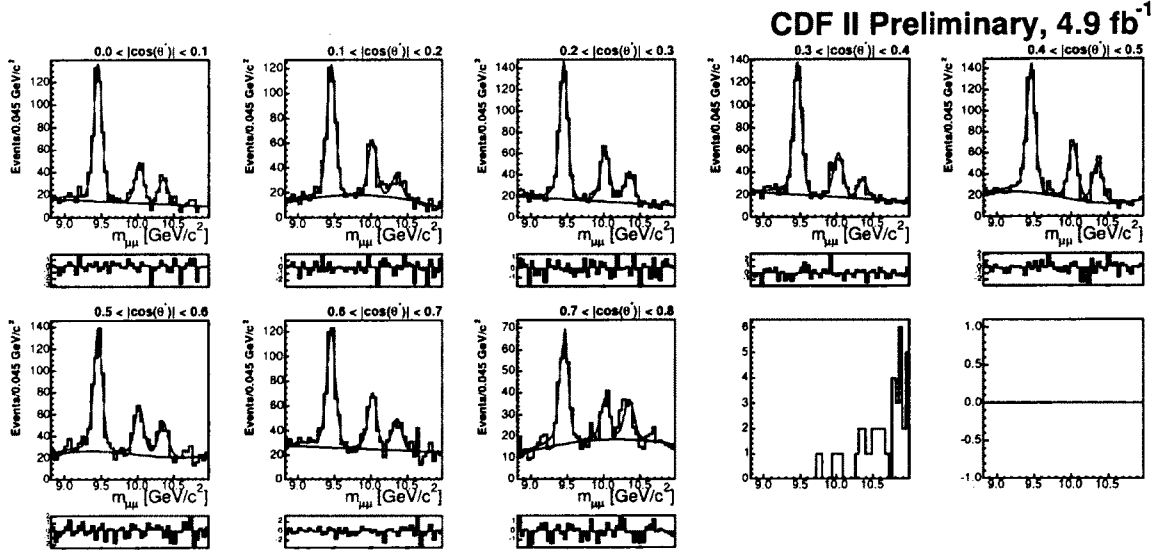


Figure B.15: Mass fits in each $\cos \theta^*$ bin of the seventh $\Upsilon(1S)$ p_T bin ($16\text{GeV}/c < p_T < 21\text{GeV}/c$).

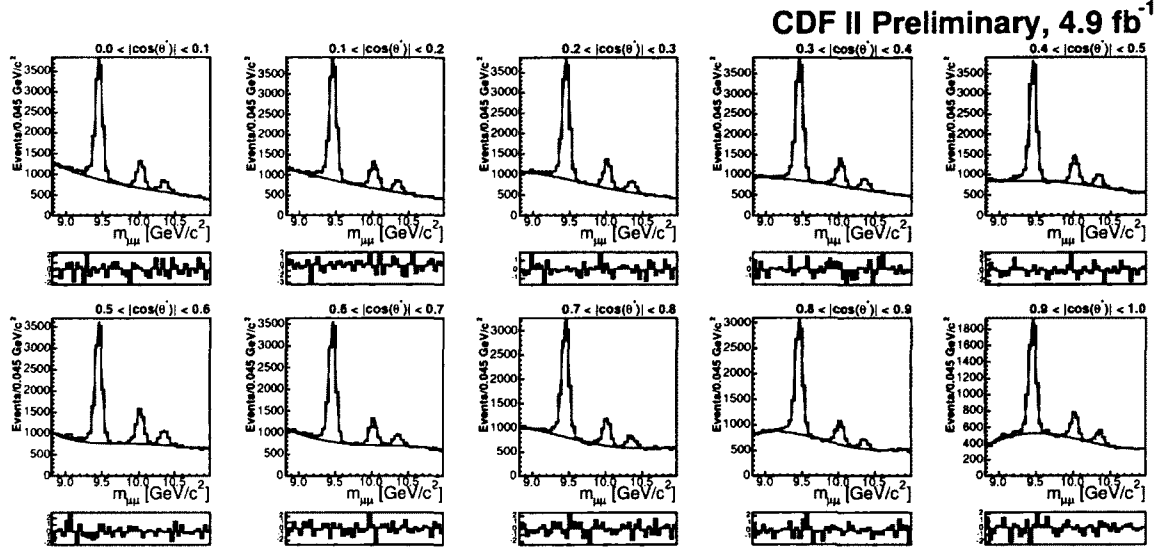


Figure B.17: Mass fits in each $\cos \theta^*$ bin of the first $\Upsilon(2S)$ and $\Upsilon(3S)$ p_T bin ($2\text{GeV}/c < p_T < 4\text{GeV}/c$), from which signal distributions are extracted. Gaussian parameters for each peak are determined by fits to Monte Carlo, and the background is modelled by an optimized Chebyshev polynomial.

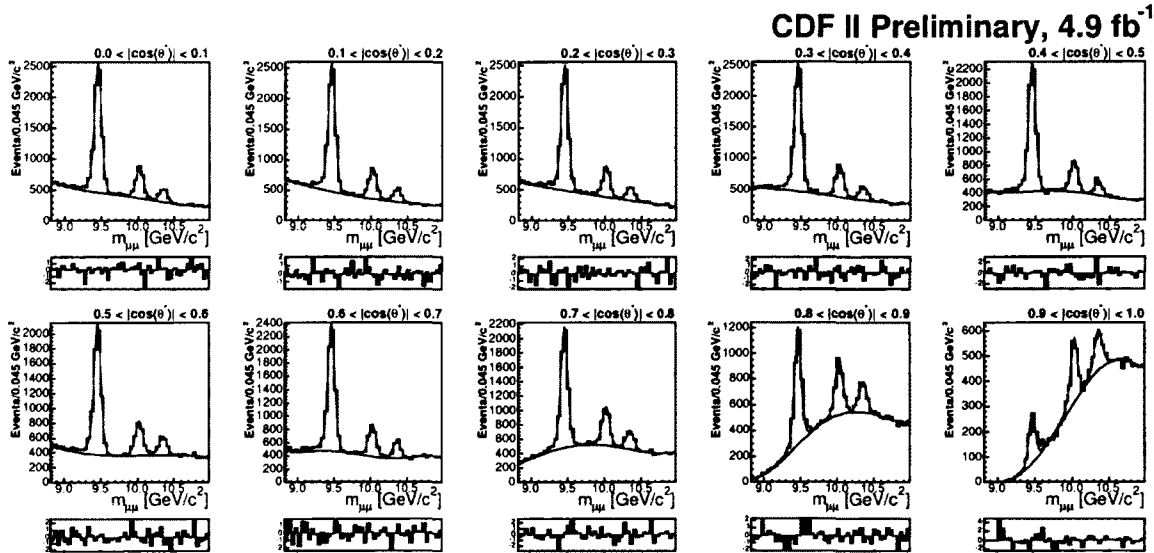


Figure B.18: Mass fits in each $\cos \theta^*$ bin of the second $\Upsilon(2S)$ and $\Upsilon(3S)$ p_T bin ($4\text{GeV}/c < p_T < 6\text{GeV}/c$).

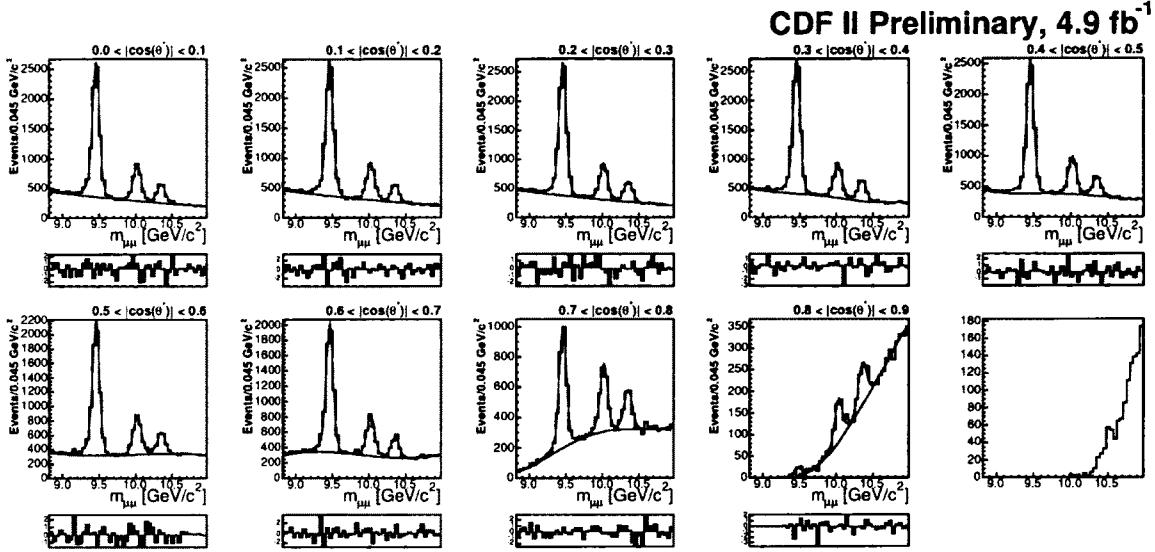


Figure B.19: Mass fits in each $\cos \theta^*$ bin of the third $\Upsilon(2S)$ and $\Upsilon(3S)$ p_T bin ($6\text{GeV}/c < p_T < 12\text{GeV}/c$).

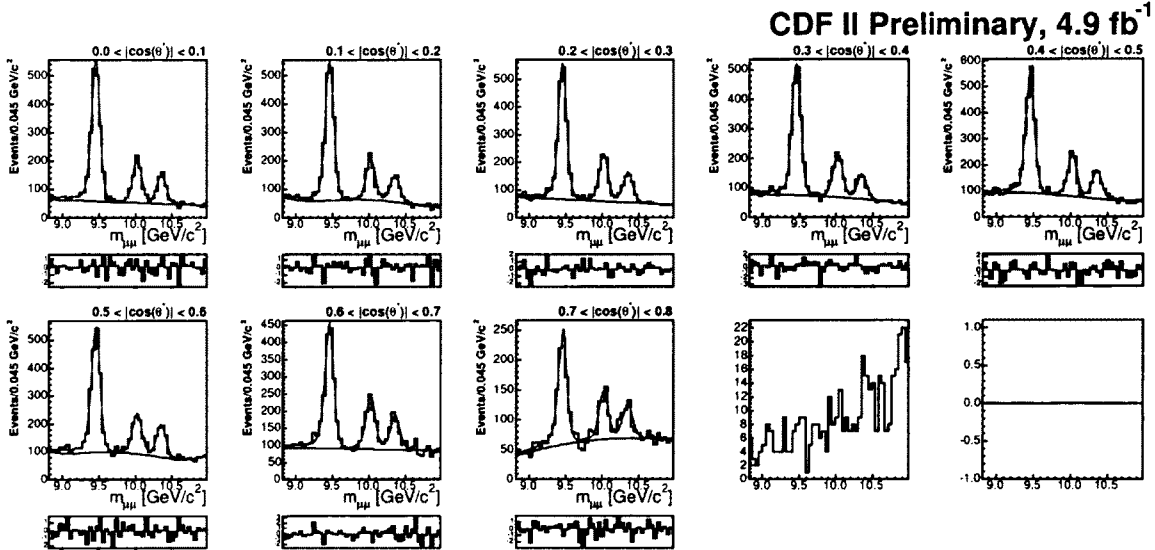


Figure B.20: Mass fits in each $\cos \theta^*$ bin of the fourth $\Upsilon(2S)$ and $\Upsilon(3S)$ p_T bin ($12\text{GeV}/c < p_T < 40\text{GeV}/c$).

Appendix C

Alternate fitter

As part of the systematic studies, a polarization is determined using the same fitter for the Υ analysis as was used for the J/ψ and $\psi(2S)$ polarization studies. It is a ROOT adaption of the Run I fitter allowing for Poisson-distributed errors. Because of the limited statistics for Υ production at high p_T , we fold the muon decay angle distribution about $\cos\theta^* = 0$ and divide the interval (0,1) into 10 equal bins. The background angular distribution B_i is produced in each Υ p_T bin using sideband information in the case of the $\Upsilon(1S)$. The signal region D_i has both signal and background events from the $\Upsilon(1S)$ mass peak region.

The theoretical signal function for $\cos\theta^*$ bin i is the polarization-weighted sum of the $T(p_T)$ and $L(p_T)$ templates for that bin in this p_T range:

$$E_i(p_T) = N(\eta; p_T)[(1 - \eta) \cdot T_i(p_T) + \eta \cdot L_i(p_T)]. \quad (\text{C.1})$$

The normalization parameter $N(\eta; p_T)$ matches the total number of events in the mass window for the specific p_T bin to the η -dependent prediction from the templates:

$$N(\eta; p_T) = \frac{\sum_i (D_i(p_T) - B_i(p_T))}{(1 - \eta) \cdot \sum_i T_i(p_T) + \eta \cdot \sum_i L_i(p_T)}. \quad (\text{C.2})$$

The fitter includes an individual background term for each $\cos \theta^*$ bin, normalized to the total number of sideband events, $\sum_i B_i(p_T)$. The minimization is done simultaneously for the total and sideband distributions according to the χ^2 function in Equation [C.3](#)

$$\chi^2 = 2 \cdot \sum_i (E_i + \beta_i - D_i) - D_i \cdot \ln \frac{E_i + \beta_i}{D_i} + (\beta_i - B_i) - B_i \cdot \ln \frac{\beta_i}{B_i} \quad (\text{C.3})$$

Here, β_i represents the expected number of background events in bin i . The inputs to this fitter are the signal-region angular distribution, two sideband-region distributions, and a sideband-subtracted distribution.